

UNIVERSITÀ
DEGLI STUDI
DELL'AQUILA

University of L'Aquila

Dipartimento di scienze Fisiche e Chimiche
PhD in Physics

Correlation-Driven Effects in Strongly Correlated Systems with Symmetry Protection and Disorder

Thesis Advisor
Prof. Sergio Ciuchi

PhD student
Arianna Poli
281783

Academic Year 2023-2024 (XXXVII cycle)

Abstract

This thesis explores the effects of strong correlations combined with additional interactions such as disorder and structural influences in nodal semimetals and correlated metals. Using Dynamical Mean Field Theory (DMFT) and Iterated Perturbation Theory (IPT) as a real-frequency solver, we analyze quasiparticle dynamics and d.c./a.c. transport properties.

The quasi-particle and transport properties of a model describing interacting Dirac and Weyl semimetals has been investigated in the presence of local Hubbard repulsion U, where an explicit deviation from the linearity of the energy-momentum dispersion through an intermediate-energy scale Λ has been introduced. The main focus is on the correlated phase of nodal semimetals.

At the nodal point, the renormalization of spectral weight at a fixed temperature T exhibits a weak dependence on Λ but is sensitive to the proximity to the Mott transition. Conversely, the scattering rate of quasi-particles and the resistivity display high-temperature exponents that crucially rely on Λ, leading to a crossover towards a conventional Fermi-liquid behaviour at finite T. Finally, by employing the Nernst-Einstein relation for conductivity, a corresponding density crossover as a function of the chemical potential has been identified.

The Kondo effect has been found in our study of the nodal semimetals by analyzing charge compressibility and spin susceptibility. Within single-site DMFT this behaviour arise due to a divergent hybridization function in the auxiliary Anderson Impurity model for the lattice solution. The solution of the Anderson impurity model with divergent hybridization, reveals a spin susceptibility peak at low temperatures, reflecting a transition from Curie-Weiss to Pauli-like behavior. This peak is explained analitically by simplifying the impurity model with a Kondo dimer where an impurity is coupled with a site in the bath. The calculated compressibility matches the analytical solution, confirming our findings.

In the correlated metallic phase of a single band Hubbard model the interplay between disorder and correlations in transport and quasiparticle properies is studied using a combination of IPT-DMFT and Coherent Potential Approximation (CPA). Interplay shows-up in a mutual, but non-symmetric, renormalization of scattering channels, leading to the breakdown of Matthiessen's rule.

CONTENTS

Introduction **1**

1 Strongly Correlated electrons: models and methods **4**
1.1 Landau-Fermi liquid theory 4
1.2 Green's function formalism for linear response 5
1.2.1 The perturbative expansion of the Green's function 5
1.2.2 Correlation effects on spectral quantities 8
1.2.3 Kubo formalism for electrical conductivity 10
1.3 The Hubbard model 11
1.4 Methods 11
1.4.1 Dynamical Mean Field Theory 12
1.4.2 Impurity Solver: Iterated Perturbation Theory 14
1.4.3 Phase diagram of the Hubbard model within DMFT 17

2 Interacting Nodal semimetals **20**
2.1 DMFT approach to nodal semimetals 21
2.1.1 The model 22
2.1.2 The local Green's function 24
2.2 The semimetal to insulator transition 27
2.2.1 Spectral function away from half-filling 31
2.3 Transport crossovers 32
2.3.1 Kubo formula approximation and DC conductivity for nodal semimetals 35
2.3.2 Temperature crossover at nodal point 37
2.3.3 Density crossover away from nodal point 39
2.3.4 Energy crossover at nodal point 41
2.3.5 Optical Conductivity and optical damping 42

3 Kondo screening in interacting nodal semimetals **46**
3.1 Kondo screening in the impurity model 46
3.2 Kondo screening in interacting materials 47
3.3 Signatures of Kondo screening in a nodal semimetal 48
3.4 Anderson Impurity model with singular hybridization function 49
3.5 Correlation function study of the Kondo dimer 50
3.5.1 Local spin susceptibility of the Kondo Dimer 51
3.5.2 Comparison with numerical calculation 53

4 Interplay between electronic and interactions and quenched and annealed disorder **55**
4.1 Quenched and annealed disorder . . . 56
4.1.1 Coherent Potential Approximation for quenched disordered systems . . 56
4.1.2 Annealed disordered systems (Classical phonons) . . . 58
4.1.3 Quenched and annealed disorder scattering rate within the CPA description . . . 60
4.2 Combining electrons correlation and disorder . . . 62
4.2.1 Probability distribution approximation for the Annealed disorder . . . 64
4.3 Results for the quenched disordered case . . . 65
4.3.1 Resistivity and scattering rate . . . 65
4.3.2 Renormalization of the disorder by the interaction and of the interaction by the disorder . . . 67
4.4 Results for the annealed disorder . . . 71
4.4.1 Scattering rate . . . 72
4.4.2 Preliminary results with interaction . . . 73

Conclusions **75**

Bibliography **77**

Appendices **83**

A Quasiparticle Damping at weak coupling **83**

B Scaling at weak coupling **86**

C Second-order perturbation theory calculations for a flat DOS **88**

D Kondo Dimer calculations **91**
D.1 Eigenvalues and eigenvectors of the Kondo dimer . . . 91
D.1.1 0-particles and 4-particles . . . 91
D.1.2 1-particle and 3-particles . . . 91
D.1.3 2-particles . . . 92
D.2 Magnetization and susceptibility in the canonical ensemble . . . 94
D.2.1 0-particles and 4-particles . . . 94
D.2.2 1-particle and 3-particles . . . 94
D.2.3 2-particles . . . 95
D.3 Limits of susceptibility in the grand canonical ensemble . . . 96
D.3.1 $T \to 0$ . . . 96
D.3.2 $T \to \infty$ . . . 96
D.3.3 Crossing temperature . . . 97

E IPT+CPA algorithm **98**

F Comparison of sampling the probability distribution using internal and free energies **100**

G Self-energy sum-rules within IPT **105**

INTRODUCTION

Strongly correlated electron materials present a notable theoretical challenge, not only because of their wide range of exotic phases but also the unique features of their non-ordered phases. These systems exhibit phenomena such as the metal-insulator transition, observed in transition-metal oxides [1], the Kondo effect in heavy fermion compounds [2–5], and the Mott insulating phase in undoped high-T_c cuprate superconductors [6].

However, any material exhibiting these properties is a complex system where electron-electron interactions are not the single contributors to their relevant physical properties. Before providing a general introduction to these materials, it is important to emphasize that the purpose of this thesis is to study models that incorporate both strong correlations and additional interactions, such as structural influences in nodal semimetals and the interplay between electronic correlations and disorder. In all the models studied here, quasiparticle properties, as well as d.c. and a.c. transport properties, are analyzed, with a focus on how these additional factors influence or are influenced by correlation effects. This analysis is crucial for disentangling the various effects observed in experiments on complex materials, allowing for a clearer distinction between the impact of electron-electron interactions, disorder, and other competing interactions.

Experiments on certain materials can be understood through the models studied in this thesis. The model for nodal semimetals, for example, provides a framework for investigating Weyl and Dirac semimetal systems, which exhibit the chiral anomaly and exotic transport properties [7–9]. These properties are influenced not only by electron correlations and lattice disorder, but also by the intrinsic structure of the system and its symmetries [10]. While graphene is intrinsically weakly correlated, it can exhibit correlation effects when placed on specific substrates or doped, in addition to the disorder effects arising from defects or impurities [11].

Another intriguing system is twisted bilayer graphene (TBG), where overlapping and rotating graphene layers at the so-called "magic angle" exhibit remarkable electronic properties. In these systems, the unique material structure induces both topological properties and strong electron correlation effects [12, 13]. Indeed, such materials can display behaviors characteristic of strongly correlated systems, such as the Kondo effect [14, 15], as well as other many-body phenomena that are not yet fully understood.

Finally, high-temperature superconductors, particularly cuprates, have been extensively

studied in recent years. In these materials, correlation-driven phenomena, such as pseudogap formation and superconductivity, are highly sensitive to disorder introduced by oxygen vacancies [6, 16]. Similarly, electron-electron interactions and disorder play a crucial role in shaping the properties of organic conductors, such as $(BEDT-TTF)_2X$, which exhibit Mott insulator transitions, where disorder can be introduced through anion substitution [17].

The thesis is organized as follows.

In the First Chapter I will give an overview of the theoretical background. From a theoretical perspective, the non-perturbative nature of purely correlated systems has led to the development of non-perturbative approaches. One of the most successful of these is Dynamical Mean Field Theory (DMFT), which provides a coherent description of the interaction-driven metal-insulator transition (MIT) even in the strong correlation regime at infinite dimensions [18]. The MIT has been successfully described for metallic lattices with a finite density of states at the Fermi level. Transport properties have also been studied near the metal-insulator transition, revealing a surprising extension of Drude-like behavior beyond the perturbative regime described by Fermi liquid theory.

In the following chapters additional factors such as structural properties or scattering from disorder are introduced alongside electronic correlation. These are studied within the framework of Dynamical Mean Field Theory. The specific models examined include a three-dimensional nodal semimetal with correlated electrons and, separately, a model where electronic correlation and disorder (both quenched and annealed) are treated on an equal footing.

Specifically, in the Second Chapter, the results obtained studying the effects of correlations on nodal semimetals are exposed. Following the discovery of graphene and its topological properties, several topological materials have been identified, studied, and characterized. In particular, nodal semimetals (Dirac and Weyl semimetals) are materials where the bands at the Fermi level cross at specific points in the Brillouin zone, resulting in linearly dispersed bands around these nodes [10, 19]. It is well known that these nodes are protected by system symmetries against local perturbations. Our study investigates the effects of local perturbations arising from electron correlations, particularly interactions mediated by short-range Coulomb repulsion. This interaction modifies transport properties, which have previously been studied in the absence of electron correlation [20, 21]. Experimental resistivity measurements on real nodal semimetal samples [7–9] have shown unexpectedly high temperature exponents. The model studied here incorporates a deviation from linearity in the band dispersion, making it more comparable to real materials.

The Third Chapter is a more detailed study of the Kondo effect in peculiar Anderson models in which the hybridization function has a singular feature. In nodal semimetals, a DMFT solution reveals the presence of Kondo screening, a low-temperature many-body phenomenon where quantum impurity spins interact with a bath of conduction electrons [22, 23]. Kondo screening typically requires a well-behaved hybridization function between the impurity and the conduction bath. In conventional systems, this function is often assumed to be constant or to vanish no faster than quadratically with energy [24]. However, in nodal semimetals, the Anderson impurity model used in DMFT exhibits a singular hybridization function due to the vanishing density of states at the nodes. Specifically, the quadratic vanishing of the density of states results in a divergence of the hybridization function near the

Fermi level, which strongly affects the Kondo screening process [25, 26]. A similar phenomenon occurs in twisted bilayer graphene (TBG) near the magic angle, where the flat bands form Dirac-like features with extremely reduced bandwidth. Moving slightly away from the magic angle increases the dispersion, and the hybridization function develops a sharp δ-like peak. These TBG systems have been modeled using heavy-fermion-like descriptions, where the singular hybridization function plays a fundamental role [12, 13].

The Fourth Chapter presents a model of correlated electrons and disorder. There are several motivations for studying a model of interacting electrons combined with disorder. Here, we propose a model based on a Bethe lattice, representing a generic metallic system with a finite density of states at the Fermi level. Impurities or lattice deformations introduce new sources of scattering that compete with electron correlation. A fundamental tool for analyzing transport properties in such systems is Matthiessen's rule, which states that different sources of scattering contribute additively to transport properties. However, this rule breaks down when multiple scattering mechanisms compete on equal footing and have similar magnitudes. In such cases, mutual renormalization of the interactions occurs. To explore these effects, we develop a combined mean-field approach where the impurity solver Iterated Perturbation Theory (IPT), commonly used in correlated systems, is integrated with the Coherent Potential Approximation (CPA), a widely used technique for disordered systems.

Chapters 2,3 and 4 report the original work made in this thesis.

Chapter 2 describes in details results published in *"Interacting nodal semimetals with nonlinear bands", A. Poli, N. Wagner, M. Fischer, A. Toschi, G. Sangiovanni, and S. Ciuchi, Phys. Rev. B 109, 045118 – Published 10 January 2024 [26]*

Chapter 3 is part of an ongoing work *M. Fischer, A. Poli, L. Crippa, S. Ciuchi, M. Vojta, A. Toschi, and G. Sangiovanni, arXiv:2503.14326 (2025)* [27].

Chapter 4 reports a work *"Stabilization of Fermi-liquid behavior by interactions in disordered metals" A. Poli, J. Coulter, S. Fratini, A. J. Millis, and S. Ciuchi, arXiv:2502.17250 (2025)* [28].

CHAPTER 1

STRONGLY CORRELATED ELECTRONS: MODELS AND METHODS

Understanding correlated electron systems is a central problem in condensed matter physics. The Band Theory of Solids [29] is a well-established method for studying electron systems in solids. It involves calculating the eigenvalues and eigenvectors of one-particle states, which are then filled with electrons. However, the one-particle approach is no longer sufficient when electron interactions become significant. In the Band Theory framework, these interactions are either neglected or approximated with a one-body potential. Materials where electron interactions play a dominant role are known as strongly correlated electron materials. The simplest yet nontrivial model to study interacting fermions is the Hubbard model. This model has been solved in the limit of large dimensions thanks to the Dynamical Mean Field Theory (DMFT) method which maps the lattice model into an auxiliary impurity model. In this approach, an Anderson impurity model must be solved, for which various impurity solvers are available. In this work, we focus specifically on the Iterated Perturbation Theory (IPT), a semi-analytical method that uses a perturbative expansion of the self-energy.

This chapter covers key theoretical concepts that aid in understanding the DMFT method and the impurity solver employed in this work. Detailed descriptions of both the DMFT method and the impurity solver will follow.

1.1 Landau-Fermi liquid theory

The Landau-Fermi liquid theory describes the behavior of metals with weak electron-electron interactions by adiabatically transforming a non-interacting system into a weakly interacting one. A central idea of Landau's theory is the introduction of quasiparticle excitations, which, in the interacting system, correspond to the Fermi particles of the non-interacting Fermi gas. This transition from an ideal free electron gas to a real Fermi liquid is achieved by establishing a one-to-one correspondence between their eigenstates, allowing the eigenstates of the non-interacting system to evolve gradually into those of the interacting system. The real eigenstates are expressed as a combination of the ideal state and a correction term, with the interaction strength characterized by a parameter λ. As interactions are introduced, each

electron becomes surrounded by a cloud of other electrons, forming a quasiparticle. These quasiparticles, which account for electron excitations, replace the particles in the free-electron theory, but with a renormalized mass m^* that is larger than the bare electron mass. In more extreme cases, such as in compounds containing rare-earth or actinide elements, where the renormalization of the mass is particularly large, the system is often referred to as exhibiting "heavy fermions." The concept of quasiparticles remains valid near the Fermi surface, where their lifetimes are sufficiently long to allow them to behave as quasi-independent particles.

This theory also provides key insights into transport properties, particularly in metals. Its application helps explain why a strongly interacting electron gas in a clean crystal can still behave nearly like a free electron gas and exhibit efficient heat and electrical conductivity at low temperatures. In this context, we focus on the scattering rate and resistivity, particularly the contribution from electron-electron scattering. In metals, this interaction leads to a T^2 and ω^2 dependence of both the scattering rate and resistivity, which dominate at low temperatures and low energies [30, 31]. In transition metals, this behavior extends to higher temperatures and energies due to the renormalized large "effective mass" of the electrons. Additionally, we explore the behavior of semimetals with linearly dispersed Dirac-like bands, where the mean-field solution results in a significantly different behavior. In this case, the scattering rate's dependence on both frequency and temperature shows an enhancement in the exponent, increasing from 2 to 8 (Section 2.2) [25, 26].

1.2 Green's function formalism for linear response

The basic procedure to study a system in many-body theory is to analyze the full Hamiltonian of the system $H = H_0 + V$ (H_0 is the free Hamiltonian and V the interaction) within perturbation theory, considering the interaction as a small perturbation [32].

1.2.1 The perturbative expansion of the Green's function

Different representations of wave functions (Ψ) and operators ($\hat{O}$) differently include the interaction in quantities of interest. Here we analyze the interaction representation which includes the time dependence in both the operators and wave functions

$$\begin{aligned} \hat{O}(t) &= e^{iH_0 t}\hat{O}e^{-iH_0 t} \\ \hat{\Psi}(t) &= e^{iH_0 t}e^{-iHt}\hat{\Psi}(0) \end{aligned} \tag{1.1}$$

This representation is built for systems where $[H_0, V] \neq 0$, in such a way that the time dependence of the wave function is only given by the interaction term and the Scrödinger equation reads

$$\frac{\partial}{\partial t}\hat{\Psi}(t) = -i\hat{V}(t)\hat{\Psi}(0) \tag{1.2}$$

and the solution is given by Dyson's series

$$\begin{aligned}\hat{\Psi}(t) =& S(t,0)\hat{\Psi}(0) \\ &= \sum_{n=0}^{\infty} \frac{(-1)^n}{n!} \int_0^t dt_1 \int_0^t dt_2 \int_0^t dt_3 ... T\hat{V}(t_1)\hat{V}(t_2)\hat{V}(t_3)...\hat{V}(t_n)\hat{\Psi}(0)\end{aligned} \tag{1.3}$$

where T represents the time ordering operator which orders the subsequent operators in a way that the first has the lower time and so on. $S(t,t')$ is the S-matrix which means scattering matrix and it changes the wave function $\Psi(t')$ into $\Psi(t)$.

While the wave function is a fundamental concept in quantum mechanics, it is not directly measurable in experiments. Instead, we focus on quantities that are more experimentally accessible. Given that interactions in the system act as scattering sources, it is useful to calculate a response function, the Green's function, which describes the average creation or annihilation of a particle in the system at a certain time. By using Green's functions, we bridge the gap between theoretical models and observable phenomena. Therefore, Green's function is defined

$$G(\lambda, t, t') = -i\langle|T\Psi(\lambda, t')\Psi^\dagger(\lambda, t)|\rangle \tag{1.4}$$

where λ is a set of quantum numbers characteristic for the system, for example $(\vec{p}, \sigma)$; $(\Psi^\dagger(\lambda, t),\ \Psi(\lambda, t'))$ are creation and destruction operators of a particle and may be written as a linear combination of the eigenstates of the unperturbed Hamiltonian H_0. They are defined in the Heisenberg representation $\Psi(\lambda, t) = e^{iHt}\Psi(\lambda)e^{-iHt}$; $|\rangle$ is the ground state for the Hamiltonian H.

The physical meaning of Green's function is to describe the creation of an excitation λ at time t' and its destruction at t when $t > t'$ and the removal of a particle from the ground state in t and its subsequent creation in t' when $t' > t$.

The Green's function is a theoretical tool that includes in itself the perturbative intervention of the interaction. The Green's function can be written in the interaction representation with the S-matrix formalism

$$G(\lambda, t - t') = -i\frac{{}_0\langle|T\hat{\Psi}(\lambda, t')\hat{\Psi}^\dagger(\lambda, t)S(\infty, -\infty)|\rangle_0}{{}_0\langle|TS(\infty, -\infty)|\rangle_0} \tag{1.5}$$

where $|\rangle_0$ is the ground state of the unperturbed Hamiltonian H_0 and $\hat{\Psi}$ and $\hat{\Psi}^\dagger$ are operators defined in the interaction representation (Eq. 1.1).

When $V = 0$ the S-Matrix is unity and the Green's function is called *unperturbed Green's function* or *free propagator*

$$G^{(0)}(\lambda, t - t') = -i_0\langle|T\hat{\Psi}(\lambda, t')\hat{\Psi}^\dagger(\lambda, t)|\rangle_0 \tag{1.6}$$

Thanks to the S-Matrix perturbative expansion we can expand the Green's function

$$G(\vec{p}, t-t') = \sum_{n=0}^{\infty} \frac{(-i)^{n+1}}{n!} \int_{-\infty}^{\infty} dt_1 \cdots \int_{-\infty}^{\infty} dt_n \frac{{}_0\langle|T\hat{\Psi}(\vec{p},t)V(t_1)\cdots V(t_n)\hat{\Psi}^\dagger(\vec{p},t')|\rangle_0}{{}_0\langle|TS(\infty,-\infty)|\rangle_0} \tag{1.7}$$

$V(t_i)$ are the interaction terms and are expressed as products of $\hat{\Psi}$ and $\hat{\Psi}^\dagger$ at t_i.

The average in the numerator can be calculated with the help of the *Wick Theorem* which states that not all the combinations between creation and destruction operators are physically possible and we must reduce the number of the possible physical terms that are non-vanishing

$${}_0\langle|T\hat{\Psi}(\alpha,t_i)\hat{\Psi}^\dagger(\beta,t_j)|\rangle_0 \tag{1.8}$$

In the end, for each fixed order of perturbative expansion n, the average in the numerator of Eq. 1.7 becomes a sum of products of unperturbed Green's functions when $t_i \neq t_j$ ($\delta_{\alpha=\beta}G^{(0)}(\alpha, t_i - t_j)$) or of number operator at equal time ($\delta_{\alpha=\beta}n_F(\epsilon_k - \mu)$). These products also include the interaction coupling functions given by the interaction terms $V(t_i)$. Each addend describes a process of an electron in the state $\vec{p}$ annihilated at time t due to a scattering process and created again in the same state at the time t'. These processes may or may not happen in the system and for this reason, some terms are exactly 0, being non physical processes. Some other processes can be simplified with the average in the denominator because they just contribute as a multiplication factor overall. This mechanism can be easily understood with the Feynmann diagram formalism that we don't express here but it associates each process propagator with a line in the time reference and each coupling function with a vertex connecting the lines of the propagators.

In the vision of the processes, Eq. 1.7, can be written in a more readable way by considering its Fourier transform

$$G(\vec{p},\omega) = \int_{-\infty}^{\infty} dt e^{i\omega(t-t')} G(\vec{p}, t-t') \tag{1.9}$$

The complete perturbative expansion in this way leads to the Dyson's equation

$$\begin{aligned} G(\vec{p},\omega) &= G_0(\vec{p},\omega) + G_0^2(\vec{p},\omega)\Sigma(\vec{p},\omega) + G_0^3(\vec{p},\omega)\Sigma^2(\vec{p},\omega) + G_0^3(\vec{p},\omega)\Sigma^4(\vec{p},\omega) + ... \\ &= \frac{G_0(\vec{p},\omega)}{1 - G_0(\vec{p},\omega)\Sigma(\vec{p},\omega)} \end{aligned} \tag{1.10}$$

where $G_0(\vec{p},\omega)$ is the unperturbed Green's function and the function $\Sigma(\vec{p},\omega)$ is called self-energy and it is the summation of infinite orders of distinct scattering processes due to the interaction. Its meaning is the energy of the electron due to the interaction and also the dynamical properties of an electron are described by the self-energy which determines the energy shift and broadening of the poles of the Green's function. In most cases, it is impossible to obtain it exactly and the theory is limited to a perturbative theory.

1.2.2 Correlation effects on spectral quantities

Physical quantities can be obtained from a specific kind of Green's function which is called retarded Green's function and is defined

$$G_{ret}(\vec{p}, t' - t) = -i\theta(t' - t)\langle\{\Psi(\vec{p}, t'), \Psi^\dagger(\vec{p}, t)\}\rangle \tag{1.11}$$

with the θ function included to preserve causality and the $\{,\}$ are the fermionic anticommutator. The spectral function associated with this Green's function is defined as

$$A(\vec{p}, \omega) = -\frac{1}{\pi} ImG_{ret}(\vec{p}, \omega) \tag{1.12}$$

When Fourier transformed, the retarded Green's function can be written in the Lehmann spectral representation which is useful to visualize its connection with the measurable spectral quantities

$$G_{ret}(\vec{p}, \omega) = \frac{1}{\mathcal{Z}} \sum_{n,m} \langle n|\Psi(\vec{p})|m\rangle\langle m|\Psi^\dagger(\vec{p})|n\rangle \frac{e^{-\beta E_n} + e^{-\beta E_m}}{\omega + E_n - E_m + i\delta} \tag{1.13}$$

where $\mathcal{Z}$ is the partition function and $|m\rangle$ and $|n\rangle$ are the eigenstates of the full Hamiltonian with eigenvalues E_m and E_n.

The spectral function is consequently

$$A(\vec{p}, \omega) = \frac{1}{\mathcal{Z}} \sum_{n,m} |\langle n|\Psi(\vec{p})|m\rangle|^2 \left(e^{-\beta E_n} + e^{-\beta E_m}\right) \delta(\omega + E_n - E_m) \tag{1.14}$$

whose meaning is the probability of observing transitions between two states with an energy difference of ω and a momentum difference of $\vec{p}$. In other words the probability to find a quasi-particle with the energy ω and the momentum $\vec{p}$.

For example, the spectral density for a non interacting system looks like a delta function

$$A^{(0)}(\vec{p}, E) = \delta(\omega - \epsilon_{\vec{p}} + \mu) \tag{1.15}$$

thus the state is localized and has an infinite lifetime because it is non-interacting and stationary.

Adding the interaction we don't consider any more the single-particle eigenstates ($\epsilon_{\vec{p}}$) but we deal with a many-body problem. So we can write the Dyson's equation also for retarded functions

$$G_{ret}(\vec{p}, \omega) = \frac{1}{\omega - \epsilon_{\vec{p}} + \mu + i\delta - \Sigma_{ret}(\vec{p}, \omega)} \tag{1.16}$$

The spectral function

$$A(\vec{p}, \omega) = -\frac{1}{\pi} \frac{Im\Sigma_{ret}(\vec{p}, \omega)}{\left(\omega - \epsilon_{\vec{p}} + \mu - Re\Sigma_{ret}(\vec{p}, \omega)\right)^2 + \left(Im\Sigma_{ret}(\vec{p}, \omega)\right)^2} \tag{1.17}$$

is now written in terms of retarded self-energy whose effects are discussed below.

When $Im\Sigma = 0$ the delta-shaped peak of the free system is just shifted of the quantity $\tilde{\omega}(\vec{p}) = \epsilon_{\vec{p}} - \mu + Re\Sigma_{ret}(\vec{p}, \omega)$ where $\tilde{\omega}(\vec{p})$ is the energy of the quasi-particle excitation. The real part of the self-energy is responsible for the renormalization of the band structure due to the presence of interactions.

The renormalized peak has this form

$$A(\omega) = Z(\vec{p})\delta(\omega - \tilde{\omega}(\vec{p})) \tag{1.18}$$

and

$$Z(\vec{p}) = \frac{1}{|1 - \frac{\partial Re[\Sigma]}{\partial \omega}|_{\omega=\tilde{\omega}(\vec{p})}|} \tag{1.19}$$

is a renormalisation factor for the delta.

If $Im\Sigma \neq 0$, $\tilde{\omega}(\vec{p})$ is no longer an eigenvalue of the interacting Hamiltonian. The lifetime of quasi-particles is finite due to the scattering, leading to a Lorentian shape of the spectral function.

When $Im\Sigma(\vec{p}, \omega)$ is smaller than the other term in the denominator of eq. (1.17), we approximate $Im\Sigma(\vec{p}, \omega) \simeq Im\Sigma(\vec{p}, \tilde{\omega}(\vec{p})) + o((\omega - \tilde{\omega}(\vec{p}))^2)$. This allows us to expand Eq. (1.17) around $\tilde{\omega}(\vec{p})$

$$A(\vec{p}, \omega) = -\frac{1}{\pi} \frac{Im\Sigma_{ret}(\vec{p}, \tilde{\omega}(\vec{p}))}{\left[Z(\vec{p})^{-1}(\omega - \tilde{\omega}(\vec{p}))\right]^2 + \left[Im\Sigma_{ret}(\vec{p}, \tilde{\omega}(\vec{p})\right]^2} =$$

$$= -\frac{1}{\pi} \frac{Z^2(\vec{p}) Im\Sigma_{ret}(\vec{p}, \tilde{\omega}(\vec{p}))}{\left[(\omega - \tilde{\omega}(\vec{p}))\right]^2 + Z^2(\vec{p}) \left[Im\Sigma_{ret}(\vec{p}, \tilde{\omega}(\vec{p}))\right]^2} \tag{1.20}$$

This has the Lorentzian shape with the half width at half height $\Gamma_{QP} = -Z(\vec{p}) Im\Sigma_{ret}(\vec{p}, \tilde{\omega}(\vec{p})) = Z(\vec{p})\Gamma$, where

$$\Gamma = -Im\Sigma_{ret}(\vec{p}, \tilde{\omega}(\vec{p})) \tag{1.21}$$

and reresents the quasiparticle scattering-rate.

Thus the spectral function can be written

$$A(\vec{p}, \omega) = \frac{1}{\pi} \frac{Z(\vec{p})\Gamma_{QP}}{\left(\omega - \tilde{\omega}(\vec{p})\right)^2 + \Gamma_{QP}^2} \tag{1.22}$$

Self-energy primarily affects the spectral function by renormalizing the energy bands and broadening the spectral function's width. Consequently, calculating self-energy is a crucial objective in solving the many-body problem. To improve approximations of self-energy, both perturbative and non-perturbative methods have been developed. Dynamical Mean Field Theory (DMFT) is the most widely used non-perturbative approach. DMFT will be discussed in the next sections, following the introduction of a standard model for studying strongly correlated electrons, the Hubbard model.

1.2.3 Kubo formalism for electrical conductivity

Condensed matter experiments often measure the linear response of a system to weak external perturbations. The effect of such perturbations is that certain operators, whose expectation values vanish in the unperturbed state, acquire non-zero expectation values. This linear response can be described using a generalized susceptibility, χ_{ij}. For instance, in a translationally invariant system, the response to an applied external electric field $\vec{E}$ to a translational is given by the electrical conductivity, σ

$$\vec{J}(\boldsymbol{k},\omega) = \sigma(\boldsymbol{k},\omega)\vec{E}(\boldsymbol{k},\omega) \tag{1.23}$$

where the observable is the current density $\vec{J}$.

The Kubo formula provides a rigorous theoretical framework for analyzing linear response in quantum systems. At its core, the Kubo formula links microscopic quantum dynamics to macroscopic observables through the fluctuation-dissipation theorem. Specifically, it relates the response function to the system's equilibrium correlation functions. For a system perturbed by an electric field, the conductivity tensor $\sigma_{\mu\nu}$ is expressed as:

$$\sigma_{\mu\nu}(\Omega) = \frac{V}{\hbar}\int_0^\infty dt e^{i\Omega t}\langle[J_\mu(t), J_\mu(0)]\rangle \tag{1.24}$$

where J_μ and J_ν are the components of the current operator, V is the system's volume, and Ω is the frequency of the applied field. This relation elegantly connects the system's equilibrium properties, encoded in the correlation function, to its non-equilibrium behaviour.

In the framework of Dynamical Mean Field Theory, the equations simplify because in the limit of high spatial dimension, where the DMFT is exact, only the bubble term for the self-energy exists and the vertex corrections can be safely neglected (see Refs. [18, 33]). In this way, by computing the thermal expectation value using Wick's theorem and reformulating it within the Matsubara summation framework (see Ref. [32]), one obtains the following formula for the conductivity:

$$\sigma(\Omega) = \frac{1}{2\pi}\int_{-\infty}^{\infty} d\omega \frac{f(\omega) - f(\omega+\Omega)}{\Omega}\frac{2e^2}{a^2\hbar}\int \frac{d^d\boldsymbol{k}}{(2\pi)^d} v^i_{\boldsymbol{k}}\hat{G}_{\boldsymbol{k}}(\omega)v^j_{\boldsymbol{k}}\hat{G}_{\boldsymbol{k}}(\omega+\Omega) \tag{1.25}$$

where $f(\omega)$ is the Fermi function, e is the electron charge, a the unit lattice spacing, $v^i_{\boldsymbol{k}} = \partial\epsilon_{\boldsymbol{k}}/\partial k_i$ are the velocity operators in the $i-$direction and $\hat{G}_{\boldsymbol{k}}(\omega)$ are the Green's functions of the electrons with frequency ω and momentum $\boldsymbol{k}$.

In the static case, when $d = 3$ and $\Omega \to 0$, Eq. 1.25 is approximated with the d.c. conductivity

$$\sigma = \bar{\sigma}4\pi\int d\omega\int d\epsilon \mathcal{N}_\phi(\epsilon)A^2(\epsilon,\omega)\left(-\frac{\partial f(\omega)}{\partial\omega}\right) \tag{1.26}$$

where $\mathcal{N}_\phi(\epsilon)$ is the current vertex distribution $\mathcal{N}_\phi(\epsilon) = \sum_k |v^i_k|^2\delta(\epsilon-\epsilon_k)$ and $\bar{\sigma} = \frac{e^2}{a\hbar}$. $A(\epsilon,\omega)$ is the quasiparticle spectral function Eq. 1.22

This formula will be employed throughout this work to calculate the conductivity from a given Green's function for the correlated electrons, which is obtained as the output of the DMFT loop. Even though it is exact for a metallic system at infinite dimension, this can't

be said for nodal semimetal systems where it is still an approximation.

1.3 The Hubbard model

The simplest model for describing interacting electrons in a solid is the Hubbard model, introduced independently by Gutzwiller, Hubbard, and Kanamori [34–36]. In this model, the electron interaction is considered to be strongly screened, meaning it is purely local. The Hamiltonian consists of two components: the kinetic energy $\hat{H}_k$ which has the simple interpretation of electrons hopping between lattice sites, and the interaction energy $\hat{H}_U$ modelling the Coulomb repulsion of two electrons on the same site

$$\hat{H} - \mu\hat{N} = -\mu \sum_{i,\sigma} \hat{n}_{i,\sigma} - \sum_{\langle i,j\rangle\sigma} t_{i,j}(\hat{c}^{\dagger}_{i\sigma}\hat{c}_{j\sigma} + \hat{c}^{\dagger}_{j\sigma}\hat{c}_{i\sigma}) + U\sum_{i} \hat{n}_{i,\uparrow}\hat{n}_{i,\downarrow} \tag{1.27}$$

where μ is the chemical potential, $t_{i,j}$ is the hopping amplitude computed by considering the overlapping of Wannier functions that are the lattice Fourier transform of Bloch functions of momentum $\boldsymbol{k}$ [37], $\hat{c}^{(\dagger)}_{i,\sigma}$ the annihilation (creation) operators of an electron with spin σ in the i-site, U the local repulsive interaction and $\hat{n}_{i,\sigma} = \hat{c}^{\dagger}_{i,\sigma}\hat{c}_{i,\sigma}$ the number particle operators.

There are two competitive terms: t-term, which tends to delocalize wave function, and U-term, which tends to localize electrons. If $\frac{U}{t} \to 0$ the relevant term is the hopping term and the eigenstates of the Hamiltonian are Slater determinants of delocalized wave functions of momentum $\boldsymbol{k}$; if $\frac{U}{t} \to \infty$ the second term discourages the double-occupation of each lattice site with associate energy cost U, then electrons, at half-filling, occupy each one a state localised on a single site, thus the ground state is localized and behave as a set of isolated atoms where the band structure loses its meaning. At half-filling this phase is called Mott insulator. Intuitively, for a certain value of the parameter $\frac{U}{t}$ the system undergoes a transition which is properly the *Mott Transition*. This transition occurs between a metallic state and an insulating state; however, the insulating state here is not a band insulator arising when a band gets completely filled. Instead, it is a correlation-driven insulating state, defined by the energy cost incurred when two electrons are brought together in the system.

1.4 Methods

Except for the two limits exposed before, the Hubbard model can't be solved analytically. The cases in which we have a solution are the one-dimensional case where the Bethe ansatz furnishes an analytical solution [38] and the infinite dimensions limit, where Dynamical Mean Field Theory is a successful method to have a numerically exact solution at many temperatures and interaction strengths [18]. This method was first formulated by A. Georges and G. Kotliar [39] after the previous work by W. Metzner and D. Vollhardt [40] where they highlighted that the infinite dimensions limit is significant for solving quantum many-body models, because it simplifies equations while preserving key features, thereby maintaining nontrivial physics.

1.4.1 Dynamical Mean Field Theory

Dynamical Mean-Field Theory (DMFT) is an approximated method which can span the non-perturbative regime of the Hubbard model up and beyond the Mott transition [18]. In the following Chapter the specific version of DMFT used is the single-site DMFT. The fundamental idea of this method is to map a lattice problem, with many degrees of freedom, into a single-site quantum impurity problem embedded in an effective medium determined in a self-consistent way. DMFT method is not fully analytical but needs a numerical impurity solver for practical calculations. This approximation may be seen as the quantum version of the classical mean-field theory applied e.g. to the Ising model. As in the classical case, in DMFT spatial fluctuations are retained at the local level but, since the model is itinerant, the site's occupation has quantum fluctuations and oscillates between empty, occupied with a spin up, occupied with a spin down and doubly occupied. This translates to the time dependence of the correlations. This method becomes exact in the limit of large dimension or large lattice connectivity.

The core idea behind the DMFT self-consistent equations is that, in the infinite-dimensional limit, the parameters of the Hubbard Hamiltonian can be rescaled to retain the system's itinerant nature with interactions intact. In this approach, the hopping term is adjusted to produce a rescaled density of states (when the coordination number $z \to \infty$, the hopping term scales like $t \to t^*/\sqrt{z}$), while the interaction term remains unchanged.

Let's consider how to calculate the system's self-energy—a crucial quantity for predicting the properties of a many-body system. As mentioned earlier, this calculation is challenging to perform analytically due to the inclusion of an infinite summation of diagrams. The self-energy $\Sigma(\vec{k}, \omega)$ is defined by the single-electron Green's function as

$$G(\vec{k}, \omega) = \frac{1}{\omega + \mu - \epsilon_{\vec{k}} - \Sigma(\vec{k}, \omega) + i\delta} \tag{1.28}$$

being μ thew chemical potential and $\epsilon_{\vec{k}}$ the energy dispersion of the conduction electrons. In the infinite-dimensional limit, the self-energy becomes exactly local in lattice space and depends only on the frequency in the Fourier space, expressed as $\Sigma(\vec{k}, \omega) = \Sigma(\omega)$ [39, 40]. With this property, the self-energy can be computed by mapping the model onto an auxiliary Anderson impurity model. The Green's function is instead dependent on $\vec{k}$ at infinite-dimensions, too. We will discuss the connection with the impurity model in more detail later. For now, it is important to note that the impurity model provides an impurity self-energy, $\Sigma_{imp}[G_0, \omega]$, which is a functional of a bath Green's function. This bath Green's function is not the free Green's function of the Hubbard model; instead, it encapsulates information from all other sites in the system.

The impurity self-energy is defined by the interacting Green's function of the impurity

$$G_{imp}(\omega) = \frac{1}{G_0^{-1}(\omega) - \Sigma_{imp}[G_0](\omega)} \tag{1.29}$$

The mean-field treatment, setting spatial fluctuations froze, imposes that at the self-consistency the site-diagonal Green's function – given by the summation over momenta of Eq. 1.28 – is equal to the impurity Green's function Eq. 1.29 ($G_{loc}(\omega) = \sum_{\vec{k}} G(\vec{k}, \omega) = G_{imp}(\omega)$). Being

also $\Sigma(\omega) = \Sigma_{imp}[G_0, \omega]$

$$G_{loc}(\omega) = \int \frac{\mathcal{N}(\epsilon)}{\omega + \mu - \Sigma(\omega) - \epsilon + i\delta} d\epsilon \tag{1.30}$$

At this point, the Dyson equation

$$G_0^{-1} = G_{loc}(\omega) + \Sigma(\omega) \tag{1.31}$$

with the mean-field equation Eq. 1.30, Eq. 1.29 and the calculation of the impurity self-energy from the impurity model, closes the set of the self-consistent equations (Fig. 1.1).

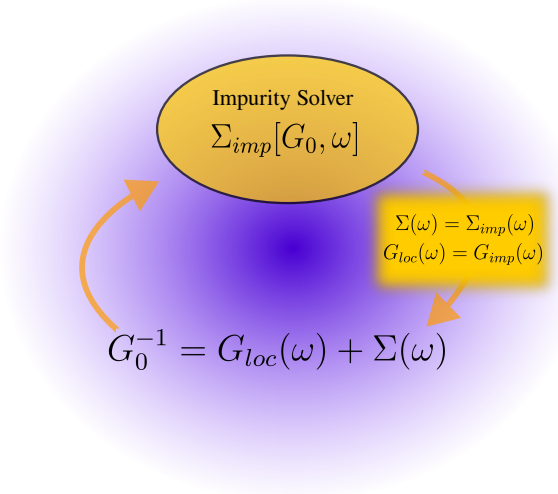


Figure 1.1: Scheeme of the DMFT loop

The dynamic of the system is described by the impurity model and G_0 gives the effect of the other impurities on the single-site. In the weak coupling regime, this expression is correct by construction because it is obtained from a perturbative expansion. In the atomic limit, where the Hubbard model describes an atomic system with localized orbitals, the limit is also reproduced by IPT.

At this point one can introduce how the mapping is performed and the description of the auxiliary Anderson impurity model. Practically, the mapping can be performed by integrating all the degrees of freedom except for the single-site i. The single site is described by $(c_{i,\sigma}, c_{i,\sigma}^\dagger)$ as an "impurity orbital" and the bath as a "conduction band". Replacing the single site operators with $(d_\sigma, d_\sigma^\dagger)$ and the bath operators with $(a_{k,\sigma}, a_{k,\sigma}^\dagger)$ to obtain the Anderson Impurity Hamiltonian

$$H_{AIM} = \sum_{k,\sigma} V_k (a_{k,\sigma}^\dagger d_\sigma + d_\sigma^\dagger a_{k,\sigma}) + \sum_\sigma \epsilon_d d_\sigma^\dagger d_\sigma + \sum_{k,\sigma} E_k a_{k,\sigma}^\dagger a_{k,\sigma} + U n_{d,\uparrow} n_{d,\downarrow} \tag{1.32}$$

where (d, $d^\dagger$) are fermionic operators of the localized state, and ($a_k^\dagger$, a_k) are the states belonging to the continuum; E_k, ϵ_d and V_k are parameters determined in a self-consistent way by the mapping from the lattice Hubbard model. The first term represents the interaction between the localized state (identified by the second term) and the band (identified by the

third term). The fourth term is an on-site interaction with strength U. In the impurity model, G_0 is the Green's function describing the hopping back and forth between the impurity and the conduction band. We can derive G_0 from the model without the interaction term

$$G_0^{-1}(\omega)^{AIM} = \omega - \epsilon_d - \sum_{\vec{k}} \frac{|V_k|^2}{\omega - E_{\vec{k}}} \tag{1.33}$$

The last term is the Hybridization function

$$\Delta(\omega) = \sum_{\vec{k}} \frac{|V_k|^2}{\omega - E_{\vec{k}}} \tag{1.34}$$

. The choice of parameters for the Anderson impurity model also defines the corresponding lattice model that can be solved using this auxiliary impurity approach.

In detail, one needs to solve the impurity problem with the aid of an impurity solver. Different impurity solvers are useful in different ranges. In this work, we will focus on Iterated Perturbation Theory (IPT) which gives results in real frequencies that are exact both at weak and strong coupling and well interpolates between these two limits.

1.4.2 Impurity Solver: Iterated Perturbation Theory

Yosida and Yamada demonstrated that perturbation theory in U for the Single Impurity Anderson Model (SIAM) behaves well in the symmetric case (half-filled in) when expanded around the Hartree-Fock solution [41, 42]. Building on their work, Georges and Kotliar introduced an impurity solver known as Iterative Perturbation Theory (IPT) to address the single-band Hubbard model within the Dynamical Mean Field Theory (DMFT) framework [39, 43]. IPT, which relies on a mean-field G_0, successfully captures both coherent and incoherent features of the single-particle spectrum. This reliance on G_0, rather than the fully dressed G, is a major advantage of such theories. Classical IPT, as it was formulated results to be incorrect for systems away from half-filling.

For this reason, Kajueter and Kotliar later introduced a refinement to IPT, known as Modified Iterative Perturbation Theory (MIPT) [44, 45]. In addition to the standard constraints of IPT, MIPT enforces a constraint on the zero-frequency behaviour of the self-energy by introducing a pseudo-chemical potential, $\tilde{\mu}$, into the Hartree-corrected bath propagators. Since $\tilde{\mu}$ can be determined in various ways, this method involves some ambiguity. Kajueter addressed this by fixing the parameter using Friedel's sum rule (equivalently, the Luttinger theorem). As the Luttinger theorem and Friedel's sum rule apply only at zero temperature, for finite-temperature calculations, Kajueter used the same $\tilde{\mu}$ value obtained from the zero-temperature case. To investigate spontaneous magnetism in the single-band Hubbard model, Potthoff, Wegner, and Nolting further enhanced MIPT by considering spectral moments up to the third order [46, 47]. Instead of using the Luttinger theorem to fix $\tilde{\mu}$, they imposed the constraint $n = n_0$. This approach is referred to as IPT-n_0.

IPT at half-filling

IPT relies on an impurity self-energy calculated with the second-order perturbative expansion

$$\Sigma(\omega) = Un + \Sigma^{(2)}(\omega) \tag{1.35}$$

In this work, a real-frequencies impurity solver has been used and the expression for the operative imaginary part of the self-energy is obtained [25]

$$\begin{aligned} Im\Sigma(\omega) = -\pi U^2 \int dxdy\ \rho(\omega - x)\rho(y)\rho(y - x)\cdot \\ \cdot (f(\omega - x)f(y)f(x - y) + f(x - \omega)f(-y)f(y - x)) \end{aligned} \tag{1.36}$$

where $\rho(x) = -\frac{1}{\pi} ImG_0(x)$ (G_0 is the real-frequency Weiss field) and f is the Fermi-Dirac function. The integral in Eq. 1.36 is the most expensive numerical part. It can be either calculated with a two-dimensional integral or, being a convolution, by using the Fast Fourier Transform. The real part of the self-energy can be calculated with Kramers-Kröening relations for spectral functions.

The self-energy in Eq. 1.35 well interpolates between the weakly interacting and the strongly interacting case, being exact in this last case.

In the weakly interacting case it can be shown that the impurity Green's function coincide with the expansion up to the second order of the Hubbard self-energy. The first term is the well-known Hartree term. This term is a constant term and can be included in the chemical potential with a resetting of this one. The second term is obtained by calculating the infinite dimension limit [40, 48] of the second-order expansion of the Hubbard self-energy which retains only the bubble term

$$\Sigma^{(2)}(\vec{k}, i\omega_n) = \sum_{\vec{k}',m} D(\vec{k}', i\omega_m) G^{(0)}(\vec{k} + \vec{k}', i\omega_n + i\omega_m) \tag{1.37}$$

where D is the bubble propagator

$$D(\vec{k}', i\omega_m) = U^2 \sum_{\vec{k}'',l} G^{(0)}(\vec{k}' + \vec{k}'', i\omega_m + i\omega_l) G^{(0)}(\vec{k}'', i\omega_l) \tag{1.38}$$

$G^{(0)}$ is the free-propagator of an electron, and ω_n, ω_m and ω_l are fermionic Matsubara frequencies in the imaginary axis $\omega_n = \frac{\pi}{\beta}(2n + 1)$ [32].

In the atomic limit, the Hubbard model has the local Green's function

$$G_{loc}(i\omega) = \frac{1}{2}\left(\frac{1}{i\omega_n - \frac{U}{2}} + \frac{1}{i\omega_n + \frac{U}{2}}\right) = \frac{1}{i\omega_n - \frac{U^2}{4i\omega_n}} \tag{1.39}$$

where the poles indicate the two Hubbard bands at $\frac{U}{2}$ and $-\frac{U}{2}$. Knowing that in the

atomic limit $G^{(0)} = \frac{1}{i\omega_n}$ we obtain the self-energy

$$G_{loc} = \frac{1}{G^{-1}_{(0)} - \Sigma} \qquad \rightarrow \qquad \Sigma(i\omega_n) = \frac{U^2}{4i\omega_n} = \frac{U^2}{4} G^{(0)}(i\omega_n) \tag{1.40}$$

The atomic limit of the self-energy formally appears as a second-order term, as the IPT in this limit yields the same result. By substituting $G^{(0)}$ into the second-order expansion for the self-energy (eq. (1.37)), we obtain

$$\Sigma^{(2)}(i\omega_n) = U^2 \sum_{\omega_m} G^{(0)}(\omega_n + \omega_m) \frac{\delta_{\omega_m,0}}{4} = \\ = \frac{U^2}{4} G^{(0)}(\omega_n) \tag{1.41}$$

An important part is to verify that the IPT satisfies sum-rules on the self-energy and this has been studied in the Appendix G.

IPT away from half-filling

For finite doping, IPT doesn't have a correct behaviour. The extension of IPT away from half-filling was proposed in [44, 45] and it relies on an interpolating scheme which well interpolates between high and low interaction strengths and high and low frequencies. The Hubbard model, when studied away from half-filling, reveals that increasing doping within the insulating phase leads to the formation of doped states within the energy gap. At low doping levels, the system retains a predominantly localized momentum regime. However, beyond a critical doping threshold, charge fluctuations between localized states and the emergent empty doped states become significant [45].

Effectively, in the extension of the IPT away from half-filling, the self-energy ansatz to the impurity problem is the one proposed previously in [49]

$$\Sigma(\omega) = Un + \frac{A\Sigma^{(2)}_{\xi}(\omega)}{1 - B\Sigma^{(2)}_{\xi}(\omega)} \tag{1.42}$$

It interpolates at low interaction strengths being a perturbative expansion expression in U. $\Sigma^{(2)}_{\xi}(\omega)$ has been calculated with Eq. 1.36 by using an effective G_0

$$G_0 = \frac{1}{\omega + \tilde{\mu} - \Delta(\omega)} \tag{1.43}$$

with $\tilde{\mu}$ a free parameter that should be determined self-consistently. The coefficients A and B are determined through the interpolation in the atomic limit (A) and high frequencies (B)

$$A = \frac{n(1-n)}{n_0(1-n_0)}$$
$$B = \frac{(1-n)U - \mu + \tilde{\mu}}{n_0(1-n_0)U^2}$$

μ is the chemical potential, n and n_0 are the carrier densities determined with the site Green's

function G_f and the effective field G_0

$$n = -\frac{1}{\pi} Im \int G_f(\omega) f(\omega) d\omega \tag{1.44}$$

$$n_0 = -\frac{1}{\pi} Im \int G_0(\omega) f(\omega) d\omega \tag{1.45}$$

In the solution of the Hubbard model, the self-consistency requires $G_f = G_{loc}$ and the $\tilde{\mu}$ parameter is determined by imposing $n = n_0$ [46]. One has to be careful with this method because even if it has been introduced to have a good result at finite temperatures, it is quite satisfactory for the correlated metal $U < U_c$ but not for higher U because it gives a solution in which the system is never insulating when $\mu \neq 0$ [50].

1.4.3 Phase diagram of the Hubbard model within DMFT

As discussed in the previous sections, the Hubbard model can be studied perturbatively only in the weak and strong coupling regimes. However, DMFT has successfully obtained a solution for the Hubbard model at intermediate couplings and we can span over a large range of U and T.

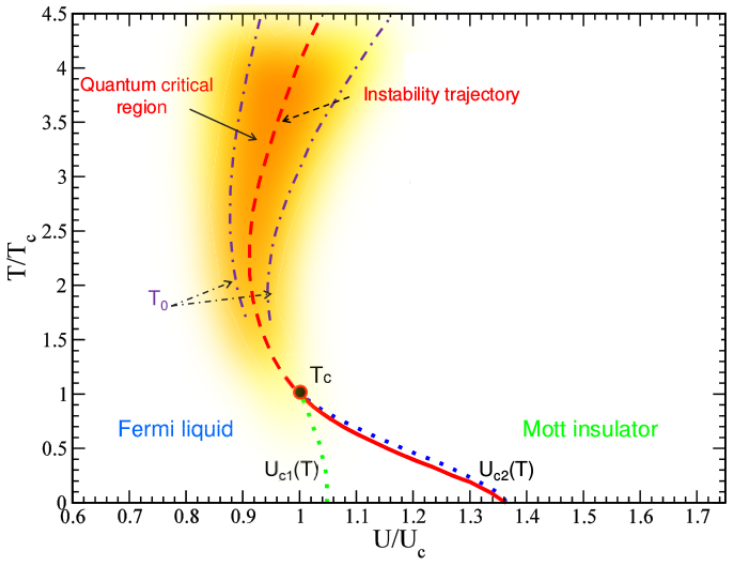


Figure 1.2: DMFT phase diagram of the Hubbard model obtained with IPT impurity solver. At low temperatures, $T < T_c$, U_{c1} and U_{c2} dashed lines define the region where both metallic and insulating solutions coexist. The full solid curve is the location of such a first-order transition line, ending up at the second-order critical point T_c . As $T > T_c$ no phase transition occurs, instead, a crossover from a metallic-like solution to an insulating-like one is observed. The critical region close to the end-point T_c is fully described within the framework of the classical liquid-gas scaling theory [51]. (Figure from Supplementary material of ref.[51])

The phase diagram Temperature-Interaction associated with the Hubbard model (Fig. 1.2) reveals the presence of a first-order transition for small temperatures while increasing U, and a second-order transition increasing the temperature. The first-order transition is a metal-insulator transition (known as the Mott transition), where the insulating phase is a phase of strongly interacting electrons localized by the on-site repulsion. For a temperature below the critical temperature for the second-order transition, the system tends to localize

electrons increasing the interaction strength U.

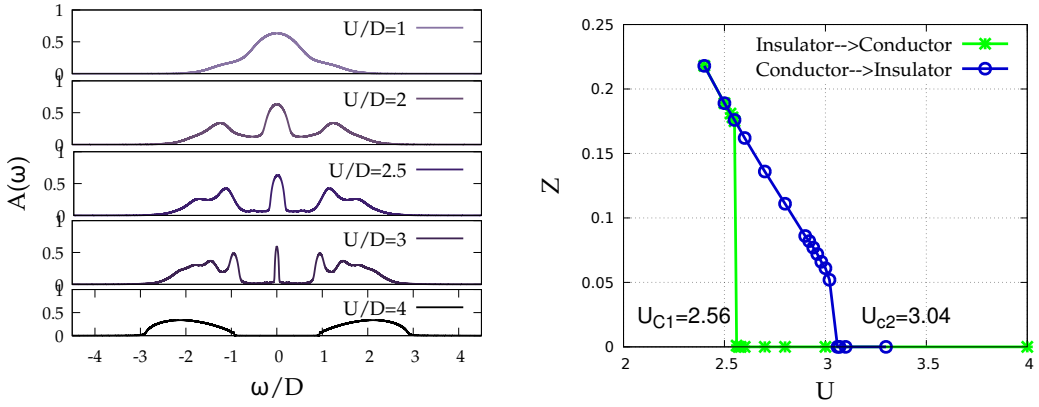


Figure 1.3: a) Mott Transition from the point of view of the density of elementary excitations. In this graph, the density is defined as $A(\omega) = -\frac{1}{\pi} Im\left[G_{loc}(\omega)\right]$. We can see the shaping of the quasiparticle peak increasing U/D where $D = 1$. At a certain value of U, there is an abrupt transition between the Fermi Liquid phase to the Mott Insulator phase. b) Hysteresis of the spectral weight obtained at $T = 0.02$ using IPT for a Bethe lattice

The evolution of the density of states (DOS) with the interaction clarifies this point (Fig. 1.3 a)). At low interactions, the DOS shows a central peak which, from the self-energy analysis, corresponds to a density of coherent quasiparticles (particles that can be described within the Fermi liquid theory). By increasing the interaction two bands start to take place on the same foot of the central density and represent localized states forming in the model. These bands are called "lower" and "upper" Hubbard bands. When the system reaches the critical interaction, the central coherent quasiparticle peak disappears, leaving space only for the two Hubbard bands placed around the energy $\omega = \pm\frac{U}{2}$.

The weight of the quasiparticle peak, when the self-energy is local, is defined by the quantity in Eq. 1.19

$$Z = \left[1 - \frac{\partial}{\partial\omega} Re\Sigma(\omega)|_{\omega=0}\right]^{-1} = \frac{m}{m*} \tag{1.46}$$

which is the inverse of the renormalized mass. By observing the evolution of the quasiparticle weight with U (Fig. 1.3 b)), it is possible to verify that there is a coexistence region between U_{c1} and U_{c2}. Starting from the metallic phase and increasing U the peak disappears (its weight is zero) when $U = U_{c2}$, while starting from the insulating phase and decreasing U, the quasiparticle peak appears (the weight is finite) at $U = U_{c1} < U_{c2}$.

Another intriguing feature of this phase diagram is the crossover observed in the correlated metal regime. As the temperature increases, the system transitions from a Fermi liquid phase to a bad metallic phase. This bad metallic phase is characterized by the presence of local moments that are not screened by the surrounding coherent electrons. This phenomenon is a hallmark of Kondo screening, which will be explored in greater detail in Chapter 3.

To understand the different phases in the diagram, it is helpful to examine the behavior of the resistivity (Fig. 1.4). For a fixed interaction strength U, increasing T, the resistivity changes from a T^2 behaviour, characteristic of a Fermi liquid, to a regime with very high resistivity values. In this regime, the resistivity is around the Ioffe-Regel-Mott limit (ρ_{MIR} calculated by imposing that $\Gamma \simeq D$), yet it remains metallic-like, as indicated by $\frac{d\rho}{dT} > 0$. This

regime corresponds to a bad metallic phase. For interaction strengths in the transition region, this increase in resistivity continues until a maximum is reached. Beyond this maximum, the system enters a semiconducting regime, where $\frac{d\rho}{dT} < 0$). This semiconducting behaviour is continuously connected to the insulating phase observed at higher temperatures on the insulating side of the phase diagram.

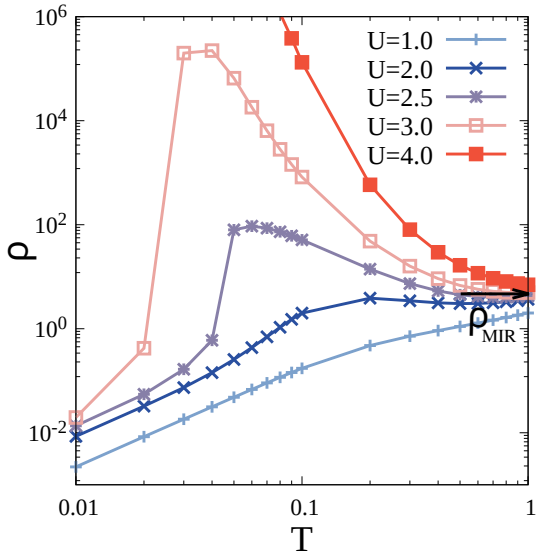


Figure 1.4: Static resistivity as a function of the temperature of the Bethe lattice calculated with the Kubo formula in the DMFT framework, for different U. The arrow represents the MIR limit.

CHAPTER 2

INTERACTING NODAL SEMIMETALS

In this chapter, I will reframe the text and figures from the article *"Interacting nodal semimetals with nonlinear bands", A. Poli, N. Wagner, M. Fischer, A. Toschi, G. Sangiovanni, and S. Ciuchi, Phys. Rev. B 109, 045118 – Published 10 January 2024 [26]* aiming to present them in a fuller, more detailed exposition.

Nodal semimetals are characterized by a linear crossing of bands, protected either by topology or by lattice symmetries. Contrary to conventional metals possessing a sizeable density of the states (DOS) at the Fermi level, the DOS of nodal semimetals in three (two) spatial dimensions, vanishes quadratically (linearly). The consequently small carriers' density at the nodal point is the origin of non-trivial transport properties. The possibility of having excitations with arbitrarily small energy gives indeed rise to non-trivial resistivity temperature exponents [20] [52].
Further, the shrinking of the Fermi surface down to a single point reduces the phase space for fermion-fermion scattering and guarantees robust protection against electronic correlations for short-range interactions [23, 53]. In the weak-to-intermediate regime, quasi-particle lifetime is much longer than in conventional Fermi liquids. This shielding effect breaks down only at strong coupling, where the self-energy can diverge and a Mott insulating state sets in.

From a general point of view the electronic properties of realistic semimetals are significantly affected by the precise spin/orbital structure of the band dispersion in the whole vicinity of the nodal point. In particular, the position of the Fermi energy with respect to the symmetry point significantly impacts the low-temperature behaviours. Further, corrections beyond the considered "Lorentz-invariant" linear dispersion are present in real materials. In Fig. 2.1 real bands of the recently discovered Weyl semimetal material TaAs are shown [54]. We can observe that in the high-symmetry point (Σ) of the First Brillouin zone, there is a Weyl point and the linear dispersion is restricted to a small energy range with respect to the full bandwidth. These deviations from linearity translate into corresponding deviations in the DOS at a scale – defined in our model as Λ – at which the non-linearity of the dispersion starts to appear. Our modelization of the "real bands" situation is sketched in Fig. 2.2.

We here study the competition between two effects: the protection against electron-electron interaction originating from the fermiology of the semimetallic band structure on

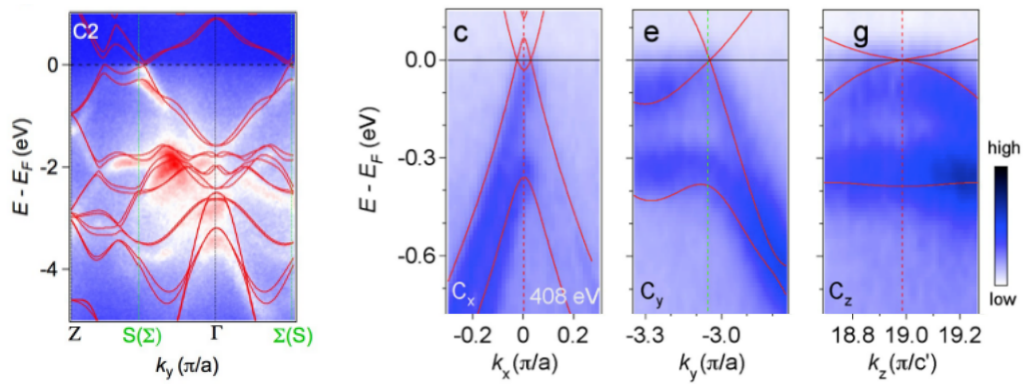


Figure 2.1: The picture shows the band structure for the $TaAs$. In the first picture, we can see that at the Fermi level in Σ point of Brillouin zone two bands are touching each other. These are measures of ARPES with calculated bands plotted on top of experiments. Picture **c**,**e** and **g** represent photoemission intensity plots along some specific directions in Brillouin zone (C_x, C_y and C_z). Superimposing lines are the calculated bands. Fig. (c) shows a double Dirac cone along the C_x-direction . (The figures are taken from ref. [54]).

the one hand and the tendency of the system to flow to strong coupling when the strength of the local Hubbard interaction U reaches the electronic half-bandwidth D. The interplay between these two counteracting effects is enriched by the presence of the intermediate scale of non-linear dispersion Λ and by finite doping when the chemical potential no longer sits at the Dirac cone. Both are non-universal factors which are present in materials and quantitatively influence their behaviour and are expected to change, for instance, the transport exponents as well as the position of the crossover scales in the phase diagram of interacting semimetals. In particular, we will focus on quasiparticle properties and transport as a function of the temperature and of the Hubbard repulsion for different Λ/D ratios.

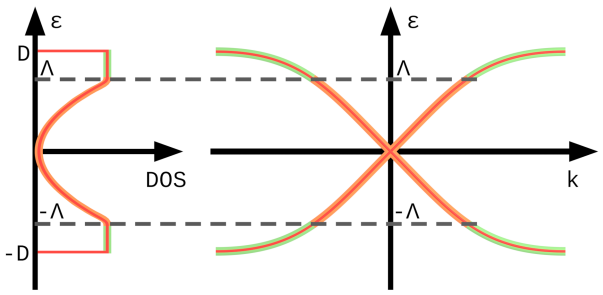


Figure 2.2: The free particle energy dispersion (on the right) and the correspondent DOS in 3 dimensions (on the left) are shown. The DOS is taken quadratic at low energy $|\epsilon| < \Lambda$ and constant at high energy $\Lambda < |\epsilon| < D$. The cutoff Λ sets the scale where the deviation from the linearity of the bands becomes relevant.

2.1 DMFT approach to nodal semimetals

We need to go beyond perturbative approaches in the electron-electron interaction. For this reason in order to address weakly and strongly interacting semimetals on equal footing, we apply dynamical mean field theory (DMFT) [18]. The self-consistent quantum impurity prob-

lem, in this case, consists of two orbitals and two spin species. As pointed out in the previous chapter, in three spatial dimensions, DMFT can be viewed as a tool for getting an approximate momentum-independent self-energy. The latter is obtained by solving the DMFT equations written in terms of the local Green's function only. Further, the momentum-dependent Green's function can be calculated with the Hamiltonian describing the non-interacting lattice model under consideration. For this, we will use here a corresponding DOS sketched in Fig. 2.2 which is specific for the 3D case and where the half-bandwidth D is our energy unit.

We will solve the DMFT equations within iterated perturbation theory (IPT), which keeps enough accuracy on the real frequency axis [44, 45, 55] and hence allows us to reliably extract transport quantities as done in Ref. [25]. Apart from the specific solver, a general disclaimer on single-site DMFT is in order, particularly when focusing on transport properties: nodal points are well protected against local interactions. Single-site DMFT does not include a momentum-dependent self-energy therefore the long wavelength effects of interaction are absent. In the case of a vanishing DOS, these effects are relevant while approaching the nodal point and the value of the temperature exponents can be modified with respect to the single site DMFT [56].

2.1.1 The model

We consider the following Hamiltonian for electrons ($\sigma =\uparrow,\downarrow$) in two orbitals ($\alpha = 1,2$) interacting through on-site Hubbard repulsion

$$\hat{H} = \sum_{\boldsymbol{k}} \boldsymbol{\psi}^{\dagger}_{\boldsymbol{k}} \hat{\boldsymbol{H}}_{\boldsymbol{0}}{}^{(4\times4)}(\boldsymbol{k})\boldsymbol{\psi}_{\boldsymbol{k}} + U\sum_{i,\alpha}(\boldsymbol{n}_{i,\alpha,\uparrow} - \frac{1}{2})(\boldsymbol{n}_{i,\alpha,\downarrow} - \frac{1}{2}) \tag{2.1}$$

where $\boldsymbol{\psi}^{(\dagger)}_{\boldsymbol{k}} \equiv (c^{(\dagger)}_{\boldsymbol{k},1,\uparrow}, c^{(\dagger)}_{\boldsymbol{k},2,\uparrow}, c^{(\dagger)}_{\boldsymbol{k},1,\downarrow}, c^{(\dagger)}_{\boldsymbol{k},2,\downarrow})$ is a four-component spinor of annihilation (creation) operators for the electrons in $\boldsymbol{k}-$space. The density of carriers $\boldsymbol{n}_{i,\alpha,\sigma} = c^{\dagger}_{i,\alpha,\sigma}c_{i,\alpha,\sigma}$.

The matrix $\boldsymbol{H_0}(\boldsymbol{k})$ defines the non-interacting part of the Hamiltonian that can have the general form

$$\hat{\boldsymbol{H}}_0^{(4\times4)}(\boldsymbol{k}) = \vec{\sigma}_z \otimes \vec{b}(\boldsymbol{k}) \cdot \vec{\tau} \tag{2.2}$$

where the energy dispersion function is

$$\vec{b}(\boldsymbol{k}) = (b_x(\boldsymbol{k}), b_y(\boldsymbol{k}), M(\boldsymbol{k})) \tag{2.3}$$

Here the Pauli matrices $\vec{\sigma}$ act on spin and $\vec{\tau}$ on orbital space. The three components of $\vec{b}(\boldsymbol{k})$ are such that around the Dirac node (here located at $\boldsymbol{k} = 0$), they acquire a linear $\boldsymbol{k}$-dependence such that for an isotropic Dirac node, we have $\hat{\boldsymbol{H}}_{\boldsymbol{0}}{}^{(4\times4)}(\boldsymbol{k}) \simeq \vec{\sigma}_z \otimes v_F\boldsymbol{k} \cdot \vec{\tau}$ with v_F being the Fermi velocity.

Since we do not consider spontaneous time-reversal symmetry-breaking and our microscopic Hamiltonian does not contain explicit time-reversal-breaking terms, all calculations shown in the following will be representative of both Dirac and Weyl fermions. The interplay between the phase-space suppression of electron-electron (el-el) scattering and local Mottness is mainly determined by the form of the band structure and on the type of interaction. For

this reason, this basic competition of physical effects would equally characterize actual Weyl fermions in the presence of time-reversal breaking terms in the single-particle Hamiltonian. The decisive point is the parabolic density of the states of the three-dimensional lattice with linear dispersion.

The free particle DOS $A_0(\omega)$ scales quadratically in energy for a pure linear band structure in three dimension.

$$\omega = v_F|\vec{k}| \tag{2.4}$$

in a generic d-dimensional space the DOS vanishes as a power law for $d > 1$ at the Weyl node indeed

$$\begin{aligned}\mathcal{N}(\omega) &= \int \frac{d^d k}{(2\pi)^d}\, \delta(\omega - v_F|\vec{k}|) = \qquad (2.5)\\ &= \frac{\Omega_d}{v_F}\int_0^\infty \frac{dk}{(2\pi)^d}\, k^{d-1}\, \delta(\frac{\omega}{v_F} - k) = \\ &= \frac{\Omega_d}{(2\pi)^d}\frac{\omega^{d-1}}{v_F^d} = \\ &= a\, \omega^{d-1} \qquad (2.6)\end{aligned}$$

Here we assume $\Omega_d = 1$. Using these units v_F has energy units.

In 3D the density of state takes the form

$$\mathcal{N}(\omega) = \frac{4\pi}{(2\pi)^3}\, \frac{\omega^2}{(v_F)^3} \tag{2.7}$$

The second term in Eq. (2.1) is a purely local Hubbard repulsion. We use DMFT to treat this last term. For a general Hamiltonian of the kind of Eq. (2.2) the standard DMFT procedure gives a local self-energy which, in view of the diagonal form of interaction in the orbital space, is also diagonal. In this work, we analyze the semi-metallic correlated and Mott phases in the absence of long-range order. In real-life materials, such states are reachable upon heating above the transition temperatures, in particular when these are suppressed by lattice geometrical effects [1, 57]. Paramagnetic DMFT is hence an ideal way of studying the effect of strong frustration.

Together with the action of local interaction, we take into account deviations from quadratic low-energy behaviour of the total DOS which are included in the specific form of the vector $\vec{b}(\boldsymbol{k})$. In particular, we introduce an intermediate energy cut-off Λ separating different zones in energy space as is depicted in Fig. 2.2 (How we treated this density of states in DMFT will be discussed in the next paragraph).

In a low energy sector ($|\epsilon| < \Lambda$), we will consider a linear approximation for the band structure in Eq. (2.2). For ($|\epsilon| > \Lambda$) instead we will neglect $b_x(\boldsymbol{k}), b_y(\boldsymbol{k})$ terms in Eq. (2.2) to maintain only the mass term. In addition assuming that the orbital-diagonal term $M(\boldsymbol{k})$ is such that $\sum_{\boldsymbol{k}} M(\boldsymbol{k}) = 0$ we arrive to an expression of the local Green's function which is a functional of the total DOS (see Paragraph 2.1.2).

This choice takes into account not only finite-bandwidth effects ($|\omega| < D$) essential to deal

with the metal-insulator transition as in Ref. [25], but also deviations from linearity occurring above the intermediate energy cutoff Λ. A flat DOS is considered to mimic a more realistic one as that obtained from tight-binding models (see e.g. Ref. [58]) at intermediate frequencies $\Lambda < |\omega| < D$. This form of the DOS will allow for analytical estimates of various quantities of interest.

2.1.2 The local Green's function

The local Green's function is not a straightforward quantity to calculate in our four-band model, especially if we aim to leverage the density of states, as is done, for instance, in the single-band Bethe lattice case (see Eq. 1.30). The density of states is the relevant quantity entering the calculations of the spectral functions in the DMFT approach but also for calculating the conductivity from the Kubo formula (Eq. 1.25). Here I will introduce our simplified model for the *total* density of states i.e. the DOS of all orbital and spin degree of freedom described before which is characterized by an intermediate cutoff in energy (Λ) separating the low-energy part (linear bands) and the high-energy part (separated bands).

The Green's function ($\hat{G}$) of the general Hamiltonian (Eq. 2.1) will be calculated and the local Green's function of the model, under certain conditions, can be expressed as a functional of the total DOS. This is not obvious for our four-bands model. Assuming that the $\vec{\sigma}$ are the Pauli matrices representing the spin part of the Hamiltonian and $\vec{\tau}$ are the orbital Pauli matrices, the Eq. 2.2 for $\boldsymbol{H}_0^{(4\times4)}$ has the standard Weyl Hamiltonian form but with different coefficients that now are $\boldsymbol{k}$-dependent. Its energy dispersion function in Eq. 2.3 has each component including the linear and non-linear parts. We define b_x, b_y and $M(\boldsymbol{k})$ to be linear functions of $\boldsymbol{k}$ around $\boldsymbol{k} \to 0$ (nodal point). The term $M(\boldsymbol{k})$ implicitly includes the linear term $b_z(\boldsymbol{k})$). With the notation $\vec{b}_\perp(\boldsymbol{k})$ and $\vec{\sigma}_\perp$ we indicate vectors projected in the x,y subspace.

Now, defining

$$b_-(\boldsymbol{k}) = (b_x(\boldsymbol{k}) - ib_y(\boldsymbol{k})) \tag{2.8}$$

$$b_+(\boldsymbol{k}) = (b_x(\boldsymbol{k}) + ib_y(\boldsymbol{k})) \tag{2.9}$$

the matrix in Eq. 2.2 has the following form

$$\hat{\boldsymbol{H}}_0^{(4\times4)}(\boldsymbol{k}) = \begin{pmatrix} M(\boldsymbol{k}) & b_-(\boldsymbol{k}) & 0 & 0 \\ b_+(\boldsymbol{k}) & -M(\boldsymbol{k}) & 0 & 0 \\ 0 & 0 & -M(\boldsymbol{k}) & -b_-(\boldsymbol{k}) \\ 0 & 0 & -b_+(\boldsymbol{k}) & M(\boldsymbol{k}) \end{pmatrix} \tag{2.10}$$

The eigenvalues of Hamiltonian Eq. (2.10) are easily evaluated as

$$\epsilon(\boldsymbol{k}) = \pm\sqrt{M^2(\boldsymbol{k}) + b_x^2(\boldsymbol{k}) + b_y^2(\boldsymbol{k})}. \tag{2.11}$$

The next step is to calculate the interacting Green's function of the model. We have to notice that, if there isn't any interaction which matches the two blocks and therefore the self-energy

is diagonal, we can have to deal only with a 2×2 matrix. The inverse Green's function reads

$$\hat{G}_{\boldsymbol{k}}^{-1} = \begin{pmatrix} z_1 - M(\boldsymbol{k}) & -b_-(\boldsymbol{k}) \\ -b_+(\boldsymbol{k}) & z_2 + M(\boldsymbol{k}) \end{pmatrix} \tag{2.12}$$

where

$$z_i = \omega + \mu - \Sigma_i(\omega) \tag{2.13}$$

The self-energy is a complex quantity $\Sigma(\omega) = Re[\Sigma(\omega)] + iIm[\Sigma(\omega)]$ and each band ($i = 1, 2$) has in principle a different self-energy.

Finally, inverting Eq. 2.12

$$\hat{G}_{\boldsymbol{k}} = \frac{1}{(z_2 + M(\boldsymbol{k}))(z_1 - M(\boldsymbol{k})) - b_\perp^2(\boldsymbol{k})} \times \begin{pmatrix} z_2 + M(\boldsymbol{k}) & b_-(\boldsymbol{k}) \\ b_+(\boldsymbol{k}) & z_1 - M(\boldsymbol{k}) \end{pmatrix} \tag{2.14}$$

where $b_\perp(\boldsymbol{k}) = \sqrt{b_x^2(\boldsymbol{k}) + b_y^2(\boldsymbol{k})}$ is the modulus of the energy dispersion in the (x, y)-plane.

The single site DMFT approach involves the calculation of the local Green function $\hat{G}_{loc} = \sum_{\boldsymbol{k}} \hat{G}_{\boldsymbol{k}}$. We will show that under some conditions the local Green function becomes a scalar quantity.

From Eq. 2.14 we can deduce the equation for $\hat{G}_{loc} = \sum_{\boldsymbol{k}} \hat{G}_{\boldsymbol{k}}$ by defining the functions

$$F(z_1, z_2) = \sum_{\boldsymbol{k}} \frac{1}{(z_2 + M(\boldsymbol{k}))(z_1 - M(\boldsymbol{k})) - b_\perp^2(\boldsymbol{k})} \tag{2.15}$$

$$P(z_1, z_2) = \sum_{\boldsymbol{k}} \frac{M(\boldsymbol{k})}{(z_2 + M(\boldsymbol{k}))(z_1 - M(\boldsymbol{k})) - b_\perp^2(\boldsymbol{k})} \tag{2.16}$$

and the off-diagonal terms

$$U_\pm(z_1, z_2) = \sum_{\boldsymbol{k}} \frac{b_\pm(\boldsymbol{k})}{(z_2 + M(\boldsymbol{k}))(z_1 - M(\boldsymbol{k})) - b_\perp^2(\boldsymbol{k})} \tag{2.17}$$

thus we have the local G as

$$\hat{G}_{loc} = \begin{pmatrix} z_2 F(z_1, z_2) + P(z_1, z_2) & U_-(z_1, z_2) \\ U_+(z_1, z_2) & z_1 F(z_1, z_2) - P(z_1, z_2) \end{pmatrix} \tag{2.18}$$

The mass term in Eq. (2.10) can be separated into an even and an odd term in $\boldsymbol{k}$ we have

$$M(\boldsymbol{k}) = M_E(\boldsymbol{k}) + M_O(\boldsymbol{k}) \tag{2.19}$$

where the symmetries ensure that $\sum_{\boldsymbol{k}} M_O(\boldsymbol{k}) = 0$ in the first Brillouin zone. Furthermore we

assume that

$$M_E(\boldsymbol{k}) = 0. \tag{2.20}$$

Let us assume also that the out-diagonal terms b_+ and b_- are odd functions of $\boldsymbol{k}$ as it can be seen e.g. from tight-biding models [58].

When $M(\boldsymbol{k})$ is an odd function of $\boldsymbol{k}$, the function defined in Eq. (2.15) is even under argument exchange $F(z_1, z_2) = F(z_2, z_1)$. This property guarantees that the DMFT self-consistency admits as a possible solution $z_1 = z_2 = z$ and $P(z, z) = U_\pm(z, z) = 0$. In this case the spectral function $A(\boldsymbol{k}, \omega) = -\frac{1}{2\pi} Im \mathrm{Tr} \hat{G}_{\boldsymbol{k}}(\omega)$ from Eq. (2.14) is

$$A(\boldsymbol{k}, \omega) = -\frac{1}{2\pi} Im \left(\frac{1}{z - |\vec{b}(\boldsymbol{k})|} + \frac{1}{z + |\vec{b}(\boldsymbol{k})|} \right) \mathbf{1} \tag{2.21}$$

All these considerations show that the off-diagonal terms after the sum over $\boldsymbol{k}$ is performed vanish and the self-consistency condition takes the following form

$$\hat{G}_{loc} = \sum_{\boldsymbol{k}} \frac{z}{z^2 - |\vec{b}(\boldsymbol{k})|^2} \mathbf{1} = \sum_{\boldsymbol{k}} \frac{1}{2} \left(\frac{1}{z - |\vec{b}(\boldsymbol{k})|} + \frac{1}{z + |\vec{b}(\boldsymbol{k})|} \right) \mathbf{1} \tag{2.22}$$

The local Green's function can be written as separating the two parts: high energy ($|E(\boldsymbol{k})| > \Lambda$) and low energy ($|E(\boldsymbol{k})| < \Lambda$)

$$\hat{G}_{loc} = \sum_{\boldsymbol{k} > \boldsymbol{k}_\Lambda} \hat{G}^{>}_{\boldsymbol{k}} + \sum_{\boldsymbol{k} < \boldsymbol{k}_\Lambda} \hat{G}^{<}_{\boldsymbol{k}} \tag{2.23}$$

where $\hat{G}^{>}_{\boldsymbol{k}}$ and $\hat{G}^{<}_{\boldsymbol{k}}$ are respectively the high and low energy limits of the Green's function in Eq. 2.14 and $|\boldsymbol{k}_\Lambda| = \Lambda / v_F$.

Low energy - The low energy part is obtained by linearization around the Weyl points

$$\hat{H}^{<} = \begin{pmatrix} t_z k_z & \lambda(k_x - i k_y) \\ \lambda(k_x + i k_y) & -t_z k_z \end{pmatrix} \tag{2.24}$$

where t_z and λ are the Fermi velocity near the nodal point of the z-component and the x, y-components respectively. The linearized Hamiltonian corresponds to the effective Weyl Hamiltonian $H^{WEYL} = v_F \boldsymbol{k} \cdot \vec{\tau}$ where without losing of generality we assume that the velocity is isotropic in the three directions $t_z = \lambda = v_F$.

The local Green function at low energy can be rewritten as:

$$G^{<}_{loc} = \frac{1}{2} \int_{-\Lambda}^{\Lambda} d\epsilon \frac{D_<(\epsilon)}{z - \epsilon} \tag{2.25}$$

where $D_<(\epsilon) = c\epsilon^2$ is the quadratic density of states corresponding to the linear part of the bands at low energy near the node(s) and c as the normalization constant.

High Energy - For energies larger than Λ we consider a constant DOS model where $D^+_>$ and $D^-_>$ are respectively the electron and the hole DOSes. Since $M(\boldsymbol{k}) = -M(-\boldsymbol{k})$ then $D^+_> = D^-_> = D_> = c\Lambda^2$. The term in Eq. 2.22 is

$$\sum_{\boldsymbol{k}>\boldsymbol{k}_\Lambda} \frac{1}{z \pm |\vec{b}(\boldsymbol{k})|} = \sum_{\boldsymbol{k}>\boldsymbol{k}_\Lambda} \int \frac{\delta(\epsilon \pm |\vec{b}(\boldsymbol{k})|}{z-\epsilon} d\epsilon = \int \frac{D^{\mp}_{>}(\epsilon)}{z-\epsilon} d\epsilon \tag{2.26}$$

The local Green's function at high energy is thus

$$G^{>}_{loc} = \frac{1}{2}\left(\int_{-\infty}^{-\Lambda} d\epsilon \frac{D_{>}(\epsilon)}{z-\epsilon} + \int_{\Lambda}^{\infty} d\epsilon \frac{D_{>}(\epsilon)}{z-\epsilon} \right) \tag{2.27}$$

Final Formula - We can define a total DOS from which the local Green function can be expressed as

$$\hat{G}_{loc} = \int_{-\infty}^{\infty} d\epsilon \frac{\mathcal{N}(\epsilon)}{z-\epsilon} \tag{2.28}$$

where

$$\mathcal{N}(\epsilon) = \begin{cases} c\epsilon^2 & -\Lambda < \epsilon < \Lambda \\ c\Lambda^2 & \Lambda < |\epsilon| < D \end{cases} \tag{2.29}$$

Notice that the normalization constant takes into account the presence of another Weyl node associated with the second block of the Hamiltonian Eq. (2.2) as well as spin multiplicity

$$\int_{-D}^{+D} \mathcal{N}(\epsilon) d\epsilon = 1 \tag{2.30}$$

which gives

$$c = \frac{1}{2\Lambda^2(D-\Lambda) + \frac{2}{3}\Lambda^3} \tag{2.31}$$

A comparison of the present model DOS and that of the anisotropic Weyl semimetal tight binding model [58] is shown in Fig. 2.3 and it confirms the validity of the choice for the DOS.

2.2 The semimetal to insulator transition

The starting point of this study is to examine the phase diagram of the previously introduced model. By analyzing the quasiparticle properties and spectral functions, we aim to map out the entire phase diagram, with a particular focus on the coherent semimetal regime, which exhibits the most significant deviations from the Fermi liquid behaviour.

We describe first the approach to the semimetal-to-insulator transition (sMIT) that occurs when the chemical potential is fixed at the nodal point upon increasing the interaction's strength U. The overall behaviour is qualitatively similar to the prototypical Mott transition in DMFT for a conventional metallic DOS (see paragraph 1.4.3). Assuming spin degeneracy (paramagnetic solutions), this statement can be illustrated using the single-particle local spectral function $A_{\rm loc}(\omega) = {\rm Tr}\sum_{\boldsymbol{k}} \boldsymbol{A}(\boldsymbol{k},\omega)$ with $\boldsymbol{A}(\boldsymbol{k},\omega) = -{\rm Im}\boldsymbol{G}(\boldsymbol{k},\omega)/\pi$ being the spectral

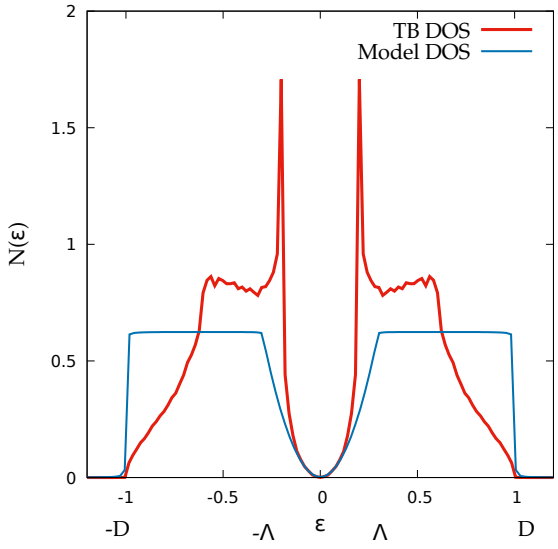


Figure 2.3: Model of free particles DOS compared with the DOS calculated from the Tight Binding (TB) model of Ref. [58] with parameters $\lambda = 0.2$. We fit our model to the curvature at the nodal point which sets our scale $\Lambda/D = 0.3$

function matrix in the spin/orbital space obtained from the Green's function matrix

$$\hat{\boldsymbol{G}}(\boldsymbol{k},\omega) = ((\omega + \mu - \Sigma(\omega))\mathbf{1} - \hat{\boldsymbol{H}}_0^{(4\times4)}(\boldsymbol{k}))^{-1}. \tag{2.32}$$

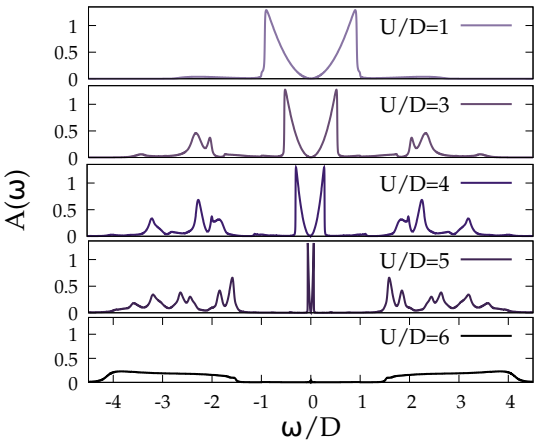


Figure 2.4: sMIT at half-filling with $\Lambda/D = 1$ and $T/D = 0.01$ illustrated with the evolution of the local DMFT spectral function. The transition from the semimetallic to the insulating state occurs at a specific critical value U_{c_2} that in this specific case is $U_{c_2}/D = 5.6$.

The evolution of the semimetallic solution across the sMIT revealed by the IPT solver of DMFT is fairly similar to that of the DMFT solution of the Hubbard model on the cubic or Bethe lattice and the evolution of the spectral function with U is shown in Fig. 2.4: the low-frequency central feature in the spectral function, made of a renormalized parabola (henceforth called U-shape), loses weight in favour of the upper and lower Hubbard bands at $\omega = \pm\frac{U}{2}$. Such a corresponding U-shape, describing a correlated nodal semimetal (NSM), finally disappears above U_{c_2}/D. The width of the parabolic U-shape gets smaller while its curvature increases as the renormalized Fermi velocity decreases. The system remains semimetallic all

the way to the sMIT, at which the curvature of the parabolic U-shape diverges and the renormalized Fermi velocity becomes zero. At larger interactions, only the Hubbard bands survive. The overall picture is remarkably similar to that found in solving a tight-binding version of Weyl-Hubbard Hamiltonian with exact diagonalization [59].

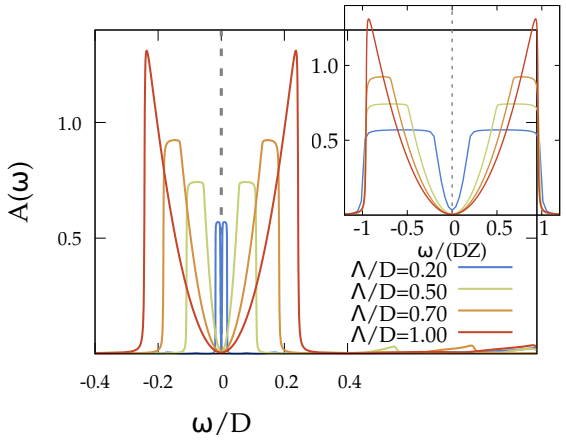


Figure 2.5: The low-frequency spectral function at half-filling for $U/D = 4.2$ and $T/D = 0.01$ in the strongly correlated semimetallic phase for different values of Λ/D. In the inset, the same quantity with the frequency axis scaled with quasiparticle Z. The Fermi level is indicated by the dashed line.

Specifically, we want to point out the spectral properties of the central coherent part of the DOS. In Fig. 2.5 it is shown at a fixed temperature ($T/D = 0.01$) in the strongly correlated NSM phase near the sMIT $U/D = 4.2$ for different values of the cutoff Λ/D. The overall weight of the central U-shape here shows a strong dependence on Λ/D. By decreasing Λ/D the system is closer to the sMIT and the central U-shape has a lower weight. In the Hubbard model for a Bethe lattice the central quasiparticle weight is associated with the factor Z (Sec. 1.4.3). In the NSM case, there is no quasi-particle peak at the nodal point therefore the factor Z, defined in Eq. 1.46 should be associated with the renormalization of the Fermi velocity instead of the mass. Indeed, the free particle DOS $A_0(\omega)$ scales quadratically in energy for a linear band structure as shown in Eq. 2.7 ($A_0(\omega) \propto \omega^2/v_F^3$) and therefore the self-energy effects included in the renormalization factor Z leads to

$$A(\omega) \propto (\omega/Z)^2/v_F^3 \tag{2.33}$$

which indeed amounts to a rescaling of the Fermi velocity

$$v_F \to Z v_F$$

as well as to a reduction of the *total* spectral weight associated with the central U-shape as is shown in the inset of to Fig. 2.5 where $A(\omega)$, plotted against ω/Z, rescales to the same width for any value of the cutoff Λ. The strong dependence of the factor Z on Λ observed in Fig. 2.5 is attributed to the proximity of the sMIT. Interestingly, when plotted against the distance from the sMIT, the factor Z shows little qualitative dependence on Λ (see Fig. 2.6). Thus, the observed Λ dependence of Z primarily arises from the variation of the critical U with Λ, as illustrated in the inset of Fig. 2.6 a).

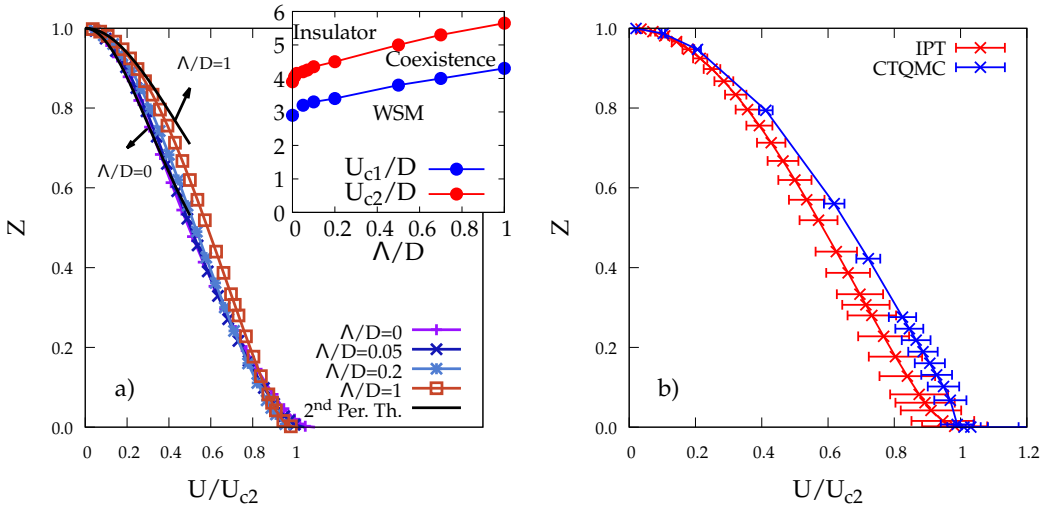


Figure 2.6: a) The quasiparticle weight Z at half-filling for $T/D = 0.01$ is calculated at several values of Λ/D as a function of U/U_{c2}. The same figure also shows the value obtained for a flat DOS ($\Lambda/D = 0$). The black lines represent the second-order diagram calculations both for the Dirac model with $\Lambda/D = 1$ [25] and the flat one with $\Lambda/D = 0$ (Appendix C). In the inset the values U_{c1}/D and U_{c2}/D as a function of Λ/D are shown for $T/D = 0.01$. b) Comparison between the renormalization factor Z calculated with IPT and QMC. Horizontal error bars are estimated considering the uncertainty in calculating U_{c2}/D, and they are shown in order to specify that the two methods give different values beyond errors but the resulting behaviour is qualitatively similar.

Regarding the phase diagram, as in the case of the Hubbard model with metallic DOS (Sec. 1.4.3), the sMIT shows a finite temperature region of coexistence of insulator and NSM solutions between U_{c_1} and U_{c_2}, both depending on Λ. The value of U_{c1} is obtained by starting from the insulating solution and decreasing U until at $U = U_{c1}$ the semimetallic U-shape suddenly appears. As for the standard MIT, the IPT solver gives larger critical values U_{c_1} and U_{c_2} when compared with ED [59]. In Fig. 2.6 b) a comparison of IPT and a CTQMC solver [60] is shown in the case $\Lambda/D = 1.0$ for $T/D = 0.01$ as a function of U/U_{c2}. The overall behaviour is similar however for this temperature CTQMC predicts $U_{c2}/D = 4.85$ while IPT gives $U_{c2}/D = 5.6$.

Differently from the Z factor, the scattering rate $\Gamma = -\mathrm{Im}\Sigma(\omega = 0)$ depends explicitly on the cutoff Λ and not only on the distance from the sMIT as is shown in Fig. 2.7. In particular, Γ increases by orders of magnitude as far as Λ decreases in the NSM phase. We shall discuss the implications of transport of this behaviour in the next section.

Another important aspect to analyze is the temperature dependence of the central U-shape. In the case of the Bethe lattice, and more generally for systems with a metallic density of states, the disappearance of the coherent central feature with increasing temperature is linked to the formation of local moments, which characterizes the bad metallic regime. For the NSM case, where the density of states vanishes at the Fermi level, it is particularly intriguing to investigate the behavior under similar conditions. In Fig. 2.8 the evolution of the central U-shape is shown for increasing temperature at the given value of interaction in the strongly correlated NSM phase for a fixed Λ. This low-energy spectral structure disappears quickly when increasing the temperature, going from the coherent semimetallic state to the incoherent bad metallic regime. This is also reflected in the momentum distribution ($\langle n(\boldsymbol{k})\rangle =$

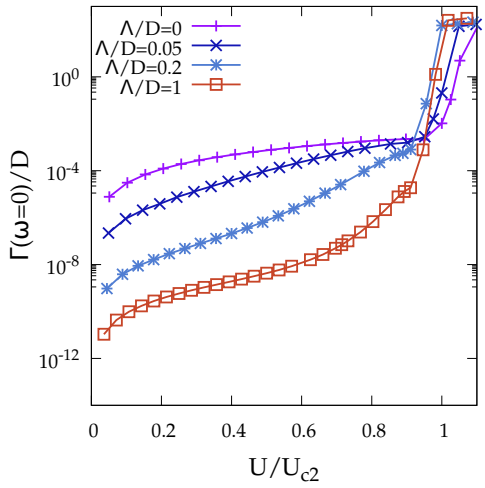


Figure 2.7: The scattering rate Γ/D at half-filling for $T/D = 0.01$ calculated at several values of Λ/D as a function of U/U_{c2}.

$\int d\omega \mathrm{Tr}\boldsymbol{A}(\boldsymbol{k},\omega))$ (inset of Fig. 2.8), where the sharp decrease around $\epsilon(k) = 0$ signalling the semimetallic Fermi point around $k = 0$ progressively disappears as the temperature reaches the scale $(T/D)^* \sim 0.1$ where the semimetallic peak disappears (black curves in Fig. 2.8). In the DMFT approach to the MIT in the single band Hubbard model the temperature above which the spectral function becomes pseudogapped has been interpreted as the Kondo scale of the associated Anderson impurity model (AIM) [18, 61, 62].

The fact that a Kondo screening is observed in the NSM strongly correlated phase despite the vanishing of the DOS at the Fermi point can indeed be rationalised by looking at the peculiar nature of the associated AIM. As in the standard single site single-orbital DMFT, in our case, the local Green function (see Eq. 2.28) can be expressed as $\hat{G} = (\omega + \mu - \Delta - \Sigma)^{-1}\mathbf{1}$ in terms of the hybridisation function Δ of an AIM. If one assumes as customary for non-pseudo-gapped system that $-Im\Delta(\omega) \propto -ImG(\omega)$ for $\omega \simeq 0$ then one should not expect Kondo screening to occur because the lack of states around the nodal point [24]. However, the semimetallic solution shows instead a *diverging* Δ around the zero energy since to get a vanishing DOS i.e. $-ImG(\omega = 0) = 0$ one needs a diverging $Im\Delta$ assuming that the self-energy is still irrelevant in the semimetallic phase around the nodal point. In the next chapter (Chap. 3), as a part of another work, it will be shown that this large hybridisation guarantees the presence of Kondo screening even when the DOS vanishes.

2.2.1 Spectral function away from half-filling

For finite doping, we have used the modified version of the IPT proposed in [44] and described in the previous chapter using the formulation illustrated in [25]. As it happens within DMFT in the metallic Hubbard model the temperature T^* at which the central U-shape gets destroyed depends strongly on chemical potential [18]. Fig. 2.9 shows the evolution of the DOS by varying the chemical potential at constant temperature $T^*/D(\mu = 0.0) = 0.1$ and for a value of the interaction where the system is insulating at half-filling. The central coherent semimetallic spectral function is restored when, starting from the insulating phase at half-

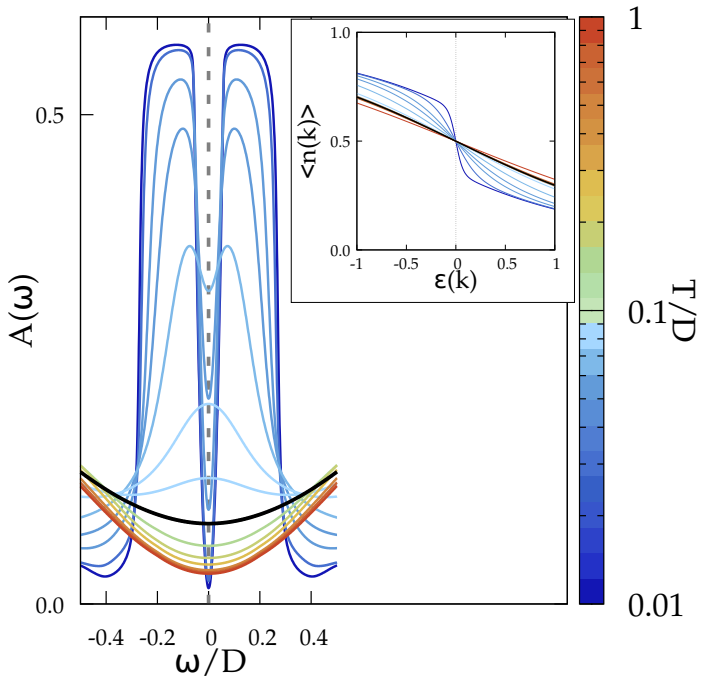


Figure 2.8: The central U-shape in the spectral function at half-filling for $U/D = 3.0$ and $\Lambda/D = 0.2$ as a function of temperatures. In the inset, the momentum distribution as a function of $\epsilon(\boldsymbol{k})$. The black bold line is the $T^*/D = 0.1$. The vertical dashed line indicates the position of the Fermi level.

filling, the system moves away from half-filling. This suggests that the coherent phase becomes more robust away from half-filling due to the newly available states for hopping, similar to the behaviour observed in a Bethe lattice [45].

2.3 Transport crossovers

The second objective of employing DMFT in real frequencies is to facilitate the straightforward calculation of transport properties directly from the spectral functions. The main reason to study transport properties for these materials is the experimental finding of high exponents of the resistivity (T^α, $\alpha = 4, 5$) for some Dirac and Weyl semimetals, for example in the type-II Weyl system WP_2 [7], in the multifold-fermion system MoP [8] and in the 3D Dirac semimetal Cd_3As_2 [9].

In the work [25], this issue was already explored. A notable result of a simple perturbative calculation for the scattering rate was the significantly higher exponents governing its temperature and energy dependence (Appendix A, Eq. A.1) compared to the standard quadratic behaviour characteristic of Fermi liquids. Using the Kubo formalism, the conductivity σ was also computed, leveraging the analytical expression for Γ and employing the bubble approximation which gives good results in the DMFT framework where the vertex corrections vanish in ladder diagrams when only using an intra-orbital-only Hubbard interaction ([25] (Suppl. Materials)), The model with linear bands at half-filling has a surprisingly high exponent for the resistivity. As shown in Fig. 2.10 (from [25]), a high exponent in temperature, which is $\alpha = 6$, characterizes what should be the Fermi liquid phase at low temperatures and before the first order transition. When the temperature increases the system has a behaviour similar

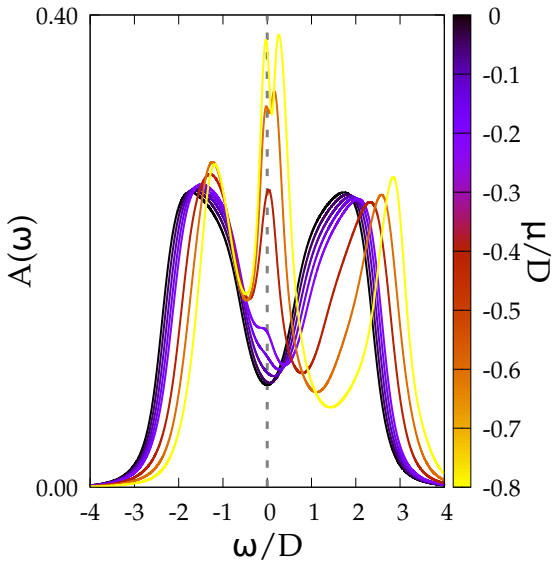


Figure 2.9: The spectral function shown at various chemical potentials for $\Lambda/D = 0.2$, $U/D = 3.0$ and $T = T^*(\mu = 0.0) = 0.1D$ where at half-filling the semimetal behaviour (U-shape) disappears. The dashed grey line indicates the position of the Fermi level.

to the case of the Bethe lattice and it goes into the bad metallic regime with the formation of local moments, characterized by a linear dependence of the resistivity by the temperature.

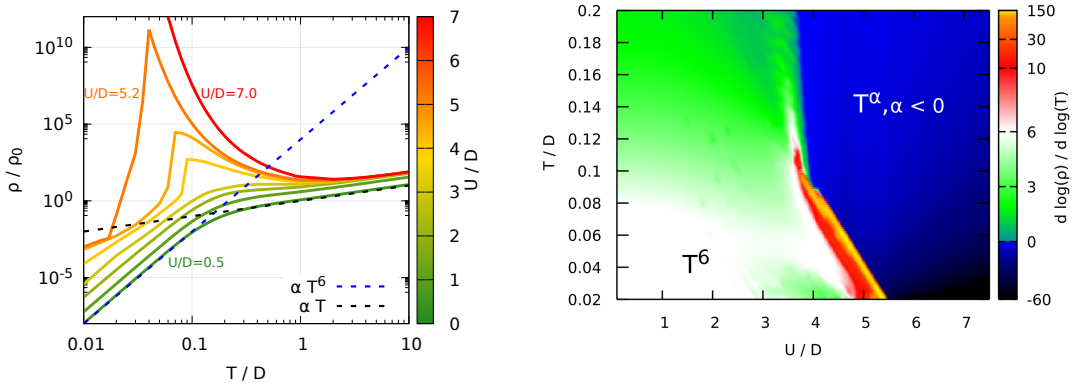


Figure 2.10: The figures obtained in [25] show the resistivity calculated for a nodal semimetal model with linear dispersed bands with the Kubo formula. The first picture shows the resistivity as a function of the temperature for different interaction strengths. The second one is a phase diagram T-U described by the exponent of the resistivity w.r.t the temperature.

This exponent is still higher than the experimental findings and the study away from half-filling reveals that the exponent decreases when increasing the doping concentration (Fig. 2.11). The experimental findings in [9] are shown in the inset of Fig. 2.11 and they show a lower exponent ($\alpha = 4$) which can be ascribed to the fact that the Fermi energy is not precisely on the node. Moving away from half-filling the theoretical model shows indeed a crossover from a T^6 exponent to a T^2 exponent (Fig. 2.11).

In this work, we aim to investigate whether incorporating deviations from band linearity in conductivity calculations can further reduce the exponent. Additionally, we utilize the Nernst-Einstein relation to explore transport properties such as compressibility and diffusivity.

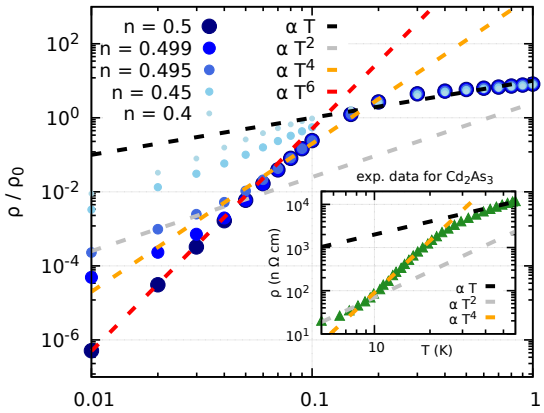


Figure 2.11: The picture taken from [25] shows the resistivity as a function of the temperature for different doping concentrations. In the inset a comparison with the experiments.

This relation connects the static conductivity σ to the charge compressibility χ and charge diffusivity $\mathcal{D}$, providing deeper insights into transport behaviour. It reads

$$\sigma = e^2 \chi \mathcal{D} \tag{2.34}$$

where the charge compressibility is

$$\chi = \frac{\partial \langle n \rangle}{\partial \mu} \tag{2.35}$$

In the work [25] the asymptotic behaviour for the conductivity at the nodal point was derived as well as for finite chemical potential in the semimetallic regime establishing an approximate Drude-Boltzmann approximation for linearly dispersing bands

$$\sigma = \frac{e^2 n_{eff} \tau}{m^*} \tag{2.36}$$

where n_{eff}/m^* is the effective number of carriers (scaled with effective mass) and τ is a scattering time defined in terms of quasiparticle scattering rate Γ. At *weak coupling* one can easily prove that $n_{eff} \propto \chi$ and $\tau \propto \mathcal{D}$ [63].

In this work, the d.c. conductivity is derived from the DMFT outcomes, both at half-filling and away from half-filling, using the Kubo formula which neglects vertex corrections. The compressibility χ will be calculated as

$$\chi = \frac{\partial \langle n \rangle}{\partial \mu} \tag{2.37}$$

where $\langle n \rangle$ is the average number of carriers obtained with the DMFT Green's function calculated with the away from half-filling code

$$\langle n \rangle = \int_{-\infty}^{\infty} f(\omega) G_{loc}(\omega) d\omega \tag{2.38}$$

The diffusivity is finally computed through the Nernst formula spanning from weak to strong coupling. In particular, we will identify different crossovers in terms of different temper-

ature exponents α of the quantities appearing in Eq. (2.34) which are related by $\alpha_\sigma = \alpha_\chi + \alpha_{\mathcal{D}}$.

2.3.1 Kubo formula approximation and DC conductivity for nodal semimetals

Before presenting the results, it is essential to clarify how the spin-orbital structure of the nodal semimetal and the deviation from linearity of the DOS enter the Kubo formula. The Kubo formula for conductivity, written in Eq. 1.25 ($\hbar = e = a = 1$), here is emplyed per spin and it disregards vertex corrections

$$Re\sigma_{i,j}(\Omega) = \frac{\bar{\sigma} 2\pi}{\Omega} \int_{-\infty}^{+\infty} d\omega \left[f(\omega - \mu) - f(\omega - \mu + \Omega) \right] \int \frac{d^3k}{(2\pi)^3} \mathrm{Tr} \left[v_i A(\boldsymbol{k}, \omega) v_j A'(\boldsymbol{k}, \omega + \Omega) \right] \tag{2.39}$$

where $A(\boldsymbol{k}, \omega)$ is the spectral function defined as $A(\boldsymbol{k}, \omega) = -\frac{1}{\pi} Im[\hat{G}(\boldsymbol{k}, \omega)]$ (Eq. 1.22) and $v_i = \frac{\partial H}{\partial k_i}$ is the velocity operator. This last quantity can be calculated, for example in the $x-$direction from the upper block of Hamiltonian Eq. 2.10

$$\hat{v}_x = \begin{pmatrix} \frac{\partial M(\boldsymbol{k})}{\partial k_x} & \frac{\partial b_-(\boldsymbol{k})}{\partial k_x} \\ \frac{\partial b_+(\boldsymbol{k})}{\partial k_x} & -\frac{\partial M(\boldsymbol{k})}{\partial k_x} \end{pmatrix} \tag{2.40}$$

Instead, considering the Green's function in Eq. 2.14 we can put $z_1 = z_2 = z$ when the components of $\vec{b}(\boldsymbol{k})$ are odd respect to $\boldsymbol{k}$. This Green's function is the same considered in [64] but it also includes the non-linear dispersion in the different components. The $\boldsymbol{k}$-integral can be divided into two different sums for low and high energies

$$\sum_{\boldsymbol{k}} Tr[v_{\boldsymbol{k}} A v_{\boldsymbol{k}} A'] = \sum_{\boldsymbol{k} < \boldsymbol{k}_\Lambda} Tr[v^<_{\boldsymbol{k}} A^< v^<_{\boldsymbol{k}} A^{<'}] + \sum_{\boldsymbol{k} > \boldsymbol{k}_\Lambda} Tr[v^>_{\boldsymbol{k}} A^> v^>_{\boldsymbol{k}} A^{>'}] \tag{2.41}$$

where we can separate the low energy and high energy density and velocity operator.

Let's study the two separate contributions.

Low Energy - We can calculate the vertex function in the $x-$direction from Eq. 2.40 assuming the limit $k_x \to 0$ near the Weyl point of Eq. 2.24 and considering an isotropic Fermi velocity $\lambda = t_z = v_F$,

$$\hat{v}^<_x = \begin{pmatrix} 0 & v_F \\ v_F & 0 \end{pmatrix} = v_F \vec{\sigma_x}. \tag{2.42}$$

It has the same spinorial structure of that e.g. Ref. [64] including intraband and interband transitions.

High Energy - Again, the high energy contribution to the conductivity can be calculated by neglecting the interband-contribution terms $b_\pm$ both in the vertex function (Eq. 2.40) and in the Green's function (Eq. 2.14 with $z_1 = z_2$). This means that the

vertex function in the high-energy regime, $\hat{v}_x^>$, looks

$$\hat{v}_x^> = \begin{pmatrix} \frac{\partial M(\boldsymbol{k})}{\partial k_x} & 0 \\ 0 & -\frac{\partial M(\boldsymbol{k})}{\partial k_x} \end{pmatrix} = \frac{\partial M(\boldsymbol{k})}{\partial k_x}\vec{\sigma_z} \tag{2.43}$$

Both the velocity operator and the Green's function are diagonal therefore the two orbitals are independent. The spectral density $A^>$ is

$$A^>(\boldsymbol{k},\omega) = \begin{pmatrix} A_+ & 0 \\ 0 & A_- \end{pmatrix}(\boldsymbol{k},\omega) \tag{2.44}$$

where

$$A_\pm(\boldsymbol{k},\omega) = -\frac{1}{\pi}\frac{Im[\Sigma]}{\left([\omega \mp M(\boldsymbol{k}) - Re[\Sigma]]^2 + [Im[\Sigma]]^2\right)} \tag{2.45}$$

The Trace become

$$\mathrm{Tr}\left[\hat{v}_x^> \hat{A}^> \hat{v}_x^> \hat{A}^{>\prime}\right] = \left(\frac{\partial M(\boldsymbol{k})}{\partial k_x}\right)^2 (A_+A'_+ + A_-A'_-) \tag{2.46}$$

and contains only the intraband transition terms.

Therefore, the DC conductivity is given by $\lim_{\Omega\to 0} Re\sigma(\Omega)$

$$Re\sigma_{xx} = \bar{\sigma} 2\pi \int_{-\infty}^{+\infty} d\omega \left(-\frac{df}{d\omega}\right) \int_{\boldsymbol{k}>\boldsymbol{k}_\Lambda} \frac{d^3k}{(2\pi)^3}\phi(\boldsymbol{k}) \left[A_+A_+ + A_-A_-\right] \tag{2.47}$$

where $\phi(\boldsymbol{k})$ is the vertex function and $\boldsymbol{k}_\Lambda = \Lambda/v_F$ as in the Section 2.1.2. Since we can define a vertex density as $\phi(\epsilon)D(\epsilon) = \sum_{\boldsymbol{k}} \phi(\boldsymbol{k})\delta(\epsilon - \epsilon_{\boldsymbol{k}})$, then $\int \frac{d^3k}{(2\pi)^3}\phi(\boldsymbol{k}) = \int d\epsilon \phi(\epsilon) D(\epsilon)$ and the integral in $\boldsymbol{k}$ is

$$\begin{aligned} Re\sigma_{xx} = \bar{\sigma} 2\pi \int_{-\infty}^{+\infty} d\omega \left(-\frac{df}{d\omega}\right) \times \\ \left[\int_{\Lambda}^{+D} \phi(\epsilon) D_>^+(\epsilon) A^{(+)} A^{(+)} + \int_{-D}^{-\Lambda} \phi(\epsilon) D_>^-(\epsilon) A^{(-)} A^{(-)}\right] \end{aligned} \tag{2.48}$$

where this time $A^{(\pm)} = A^{(\pm)}(\epsilon,\omega)$ are

$$A^{(\pm)}(\epsilon,\omega) = -\frac{1}{\pi}\frac{Im[\Sigma]}{\left([\omega \mp \epsilon - Re[\Sigma]]^2 + [Im[\Sigma]]^2\right)} \tag{2.49}$$

This formulation is valid whenever $M^2(\boldsymbol{k}) \gg (b_x^2 + b_y^2)$.

Now, we need to briefly discuss the evaluation of $\phi(\epsilon)$. Our objective is to match the high-energy vertex function, $\phi(\epsilon)$, with the constant vertex described in Ref. [64], which is $\phi_{LE} = v_F^2/3$. To simplify the analysis, we assume that the vertex function in

the high-energy case is constant with respect to energy and we force both to be the same constant $\phi(\epsilon) = \phi_{LE} = 1/3$.

As a result, by combining the low and high energy contributions one can obtain the final and complete formula for the d.c. conductivity for our 4 bands model of a nodal semimetal. Taking into account the parts in Ref. [64] with the appropriate considerations for the vertex function and Eq. 2.48 and following Eq. 2.41

$$Re\sigma_{xx} = \bar{\sigma} 2\pi \int_{-\infty}^{+\infty} d\omega \left(-\frac{df}{d\omega}\right) \times \\ \times \left(\int_{-D}^{D} d\epsilon \mathcal{N}(\epsilon) \left[A^{(+)}A^{(+)} + A^{(-)}A^{(-)}\right] + \int_{-\Lambda}^{\Lambda} d\epsilon \, 2c\epsilon^2 \left[A^{(+)}A^{(-)} + A^{(-)}A^{(+)}\right] \right) \tag{2.50}$$

Here, $\mathcal{N}(\epsilon)$ and c are the same as in Eq. (2.29).

The conductivity has in this way two contributions: the first term is an intraband contribution which is given by all the bands and the second term an interband contribution given by the linear bands.

2.3.2 Temperature crossover at nodal point

A study of the three transport quantities mentioned before (σ, χ, and $\mathcal{D}$) has been performed as a function of the temperature at half-filling where the Fermi energy is chosen to be exactly at the nodal point. Here, σ has been calculated in units of $\bar{\sigma}$.

It is worth remembering here some results valid in the single band Hubbard model at half-filling for the Bethe model. At weak coupling, in the Fermi Liquid state, the system behaves as a conventional metal therefore, in the Drude approach, the temperature dependence of the conductivity arises entirely from the scattering time 1.4.3. In the Nernst-Einstein approach indeed the compressibility is almost constant w.r.t. both temperature and chemical potential assuming that $T \ll D$ and $|\mu| \ll D$. The temperature dependence of the conductivity is therefore solely due to the temperature dependence of the diffusivity i.e. $\mathcal{D} \propto \tau \propto T^{-2}$ and in terms of temperature exponents $\alpha_\sigma = \alpha_\mathcal{D} = -2$.

In the opposite limit of incoherent scattering when $T \gg T^*$, the linear behaviour for the resistivity is solely due to the temperature dependence of the compressibility, while the diffusion constant is almost constant, i.e. $\alpha_\sigma = \alpha_\chi = -1$ [65].

The analysis of Ref. [25] for the case of pure quadratic DOS ($\Lambda/D = 1.0$) at half-filling can be then reinterpreted in terms of temperature exponents for σ,χ and $\mathcal{D}$. The vanishing of the spectral function at the nodal point induces qualitative deviations from the conventional Fermi liquid behaviour in the weak coupling regime. In this case both χ and $\mathcal{D}$ contribute to the temperature exponent of conductivity, namely $\alpha_\chi = 2$ while $\alpha_\mathcal{D} = -8$ that corresponds to $\alpha_\sigma = -6$ [25]. From the point of view of the Nernst relation, the large diffusivity of the states near the nodal point overcompensates the vanishing charge susceptibility i.e. the vanishing number of available carriers in Eq. (2.36) leading to a large temperature exponent for resistivity. Moving away from half-filling ($|\mu| < T$), the low-temperature behaviour becomes dominated by the presence of a finite spectral function at the chemical potential and Fermi-

liquid exponents are expected $\alpha_\sigma = \alpha_{\mathcal{D}} = -2$.

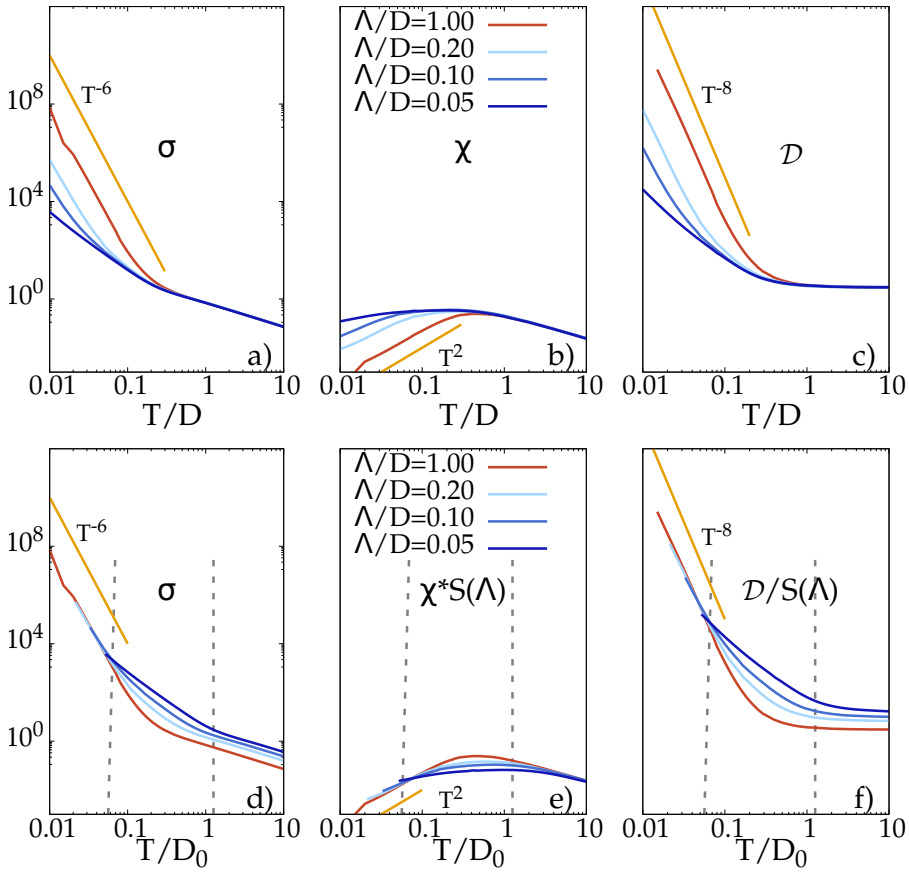


Figure 2.12: Conductivity (a), charge compressibility (b) and diffusivity (c) at $\mu = 0$ as a function of the temperature at weak coupling ($U/D = 0.5$). The same quantities (respectively d), e) and f)) at $\mu = 0$ as a function of the scaled temperature at weak coupling ($U/D = 0.5$). The dashed grey lines are useful to separate the crossover central region from the NSM one at lower temperatures and the bad metal one at higher temperatures.

These exponents are further modified by the presence of cut-off energy Λ leading to temperature and density crossover. Evidently, in Fig. 2.12 we show the conductivity (a), charge compressibility (b) and diffusivity (c) at the nodal point as a function of the temperature at weak coupling ($U/D = 0.5$). The low-energy behaviour can be studied by introducing a scaling method. This scaling method is designed to bring different models with different values of the cutoff Λ/D to the same Fermi velocity, thereby achieving the same curvature of the density of states around zero energy, as described in Appendix B. In Fig. 2.12 (d), e) and f)) we present the same coefficients as shown in Fig. 2.12 (a), b) and c)) but plotted as a function of scaled temperatures at weak coupling ($U/D = 0.5$). The scaling approach enables a collapse of the curves at low temperatures for various values of the cutoff Λ/D.

As explicitly shown in Appendix B, this scaling introduces a factor $S(\lambda) = \left(\lambda^3 + 3\lambda^2(1-\lambda)\right)^{\frac{1}{3}}$ where $\lambda = \Lambda/D$, and the temperature is calculated in units of a fixed half-bandwidth $D_0 = S(\lambda)D$. The scaled picture highlights that the limiting temperature behaviour found for $T/D_0 \ll 1$ shows the characteristic low-temperature exponents $\alpha_\sigma = -6$, $\alpha_\chi = 2$, $\alpha_{\mathcal{D}} = -8$. However, by increasing the temperature we enter the intermediate temperature *metallic* phase characterized by the same exponents found for a Fermi liquid i.e. $\alpha_\sigma - 2$, $\alpha_\chi = 0$ and $\alpha_{\mathcal{D}} = -2$.

By further increasing the temperature, when $T/D > 1$ the incoherent Λ-independent regime is reached. This regime is clearly seen in Fig. 2.12 where $\alpha_\sigma = -1$, $\alpha_\chi = -1$, $\alpha_\mathcal{D} = 0$, i.e. the same as for the incoherent bad metallic regime [65].

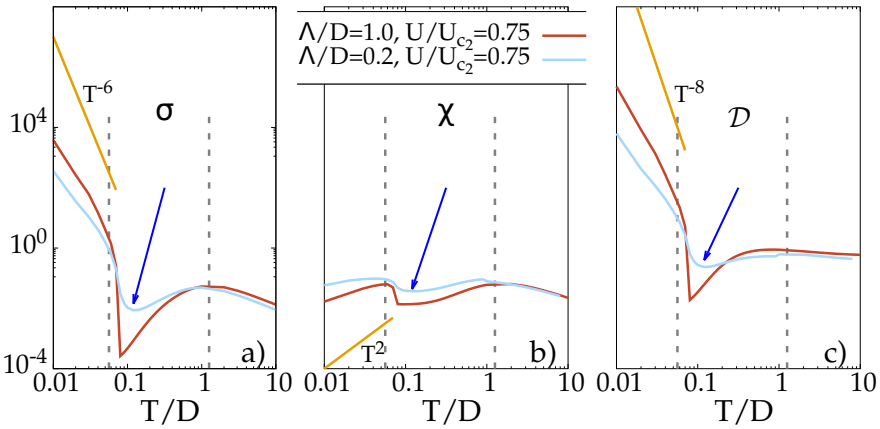


Figure 2.13: Conductivity (a), charge compressibility (b) and diffusivity (c) at $\mu = 0$ as a function of the temperature at strong coupling near the sMIT. Arrows indicate the temperature at which the quasiparticle U-shape disappears ($T^*/D = 0.1$). The dashed grey lines are useful to separate the transition central region from the NSM one at lower temperatures and the bad metal one at higher temperatures.

In Fig. 2.13 the quantities σ, χ and D are shown in the strongly correlated NSM phase ($U/U_{c_2} = 0.75$) at half-filling. At low temperatures ($T < T^*$) a semimetallic behaviour is observed but with apparent exponents which slightly deviate from that of the weak coupling at $\Lambda/D = 1$ as shown in the figure. Deviation from the exponents observed in the weak-coupling regime gets more marked for $\Lambda/D < 1$. By increasing the temperature we eventually meet the first-order finite temperature transition for $\Lambda/D = 1$ which appears to be smoothed out for smaller Λ. By further increasing the temperature a non-monotonic behaviour of σ and χ is observed after the disappearance of the coherent central U-shape at T^*/D (arrows in Fig. 2.13). A final bad metallic regime with the conductivity and compressibility decreasing linearly with T is reached on a temperature scale larger than the bare half-bandwidth. Interestingly the sharp variation of charge compressibility observed around $T = T^*$ in Fig. 2.13 b) is similar to that found in the strongly correlated metallic phase of the single-band Hubbard model [65]. There, the charge susceptibility increases upon decreasing the temperature and reaches a constant value at $T/D = 0$ due to the onset of Kondo screening of the local moments. In contrast, here, χ after a first increase finally decreases when lowering the temperature as expected from the vanishing of the spectral function. However, its initial growth which occurs as far as the central U-shape is restored for $T < T^*$ indirectly suggests that an interpretation of the results in terms of the screening of local moments is possible in the strongly correlated NSM at least on an intermediate temperature scale due to the finite, albeit small, spectral weight at the nodal point [18, 61].

2.3.3 Density crossover away from nodal point

A second part of the study has been done away from half-filling. While conductivity is obtained by the Kubo formula Eq. (2.39), the compressibility has been obtained by a numerical

derivative of the filling with respect to the chemical potential. In Fig. 2.14 a) and b) the dependence of the filling on the chemical potential is shown explicitly. The small density of carriers in the node region is at the origin of the drop in compressibility near the node.

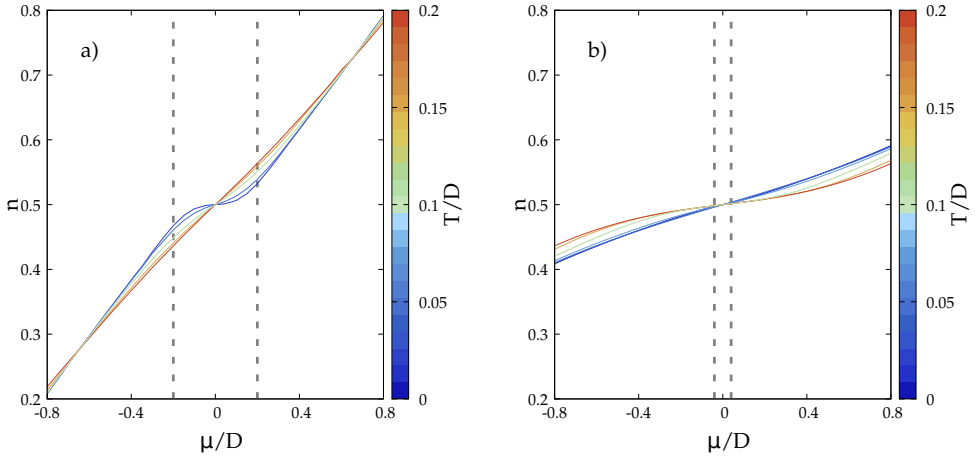


Figure 2.14: Filling as a function of the chemical potential for different temperatures at $\Lambda/D = 0.2$ and $U/D = 0.5$ (a) and $U/D = 3.0$ (b). Dashed grey lines indicate the width of the U-shaped structure in the spectral function.

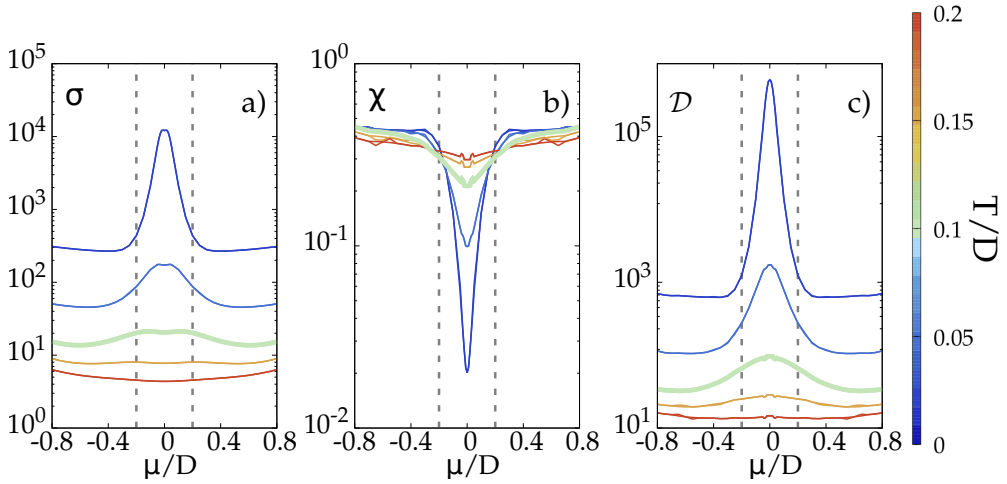


Figure 2.15: Conductivity (a), charge compressibility (b) and diffusivity (c) for $U/D = 0.5$ and $\Lambda/D = 0.2$ as a function of the chemical potential. Different curves refer to different temperatures. Dashed grey lines indicate the width of the U-shaped structure in the spectral function.

Figures 2.15 and 2.16 show the quantities involved in the Nernst relation as a function of the chemical potential for different temperatures. At weak coupling and low temperatures ($T < \Lambda$) (Fig. 2.15) we can identify tree regions:

i) When $|\mu| \ll T$, the system is really close to the nodal point and the temperature exponents are those found at the nodal point [25]. In this region, thermal fluctuations probe energy ranges in which the spectral density is very small and the behaviour of all quantities tends to be weakly dependent on μ.

ii) When $T < \mu < \Lambda$ the behaviour in μ is that of a NSM with linear bands: the diffusivity decreases and the compressibility increases with μ as expected from the increasing of the spectral density. The smaller the temperature the sharper the conductivity drop.

iii) When $\mu > \Lambda$ the transport properties have a Fermi liquid behaviour dominated by the non-linear part of the band structure.

A clear distinction between these zones disappears gradually as T approaches Λ when the semimetallic regime is gradually washed out.

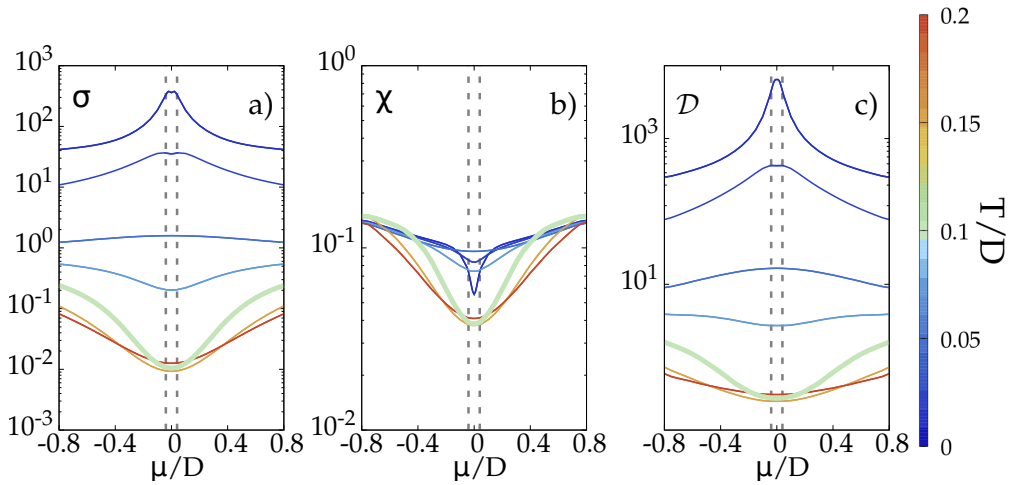


Figure 2.16: Conductivity (a), charge compressibility (b) and diffusivity (c) for $U/D = 3.0$ and $\Lambda/D = 0.2$ as a function of the chemical potential. Different curves refer to different temperatures. The green bold line ($T^*/D = 0.1$) marks the temperature at which, at half-filling, the quasiparticle U-shape vanishes. Dashed grey lines indicate the width of the U-shaped structure in the spectral function.

In the strongly correlated NSM phase, (Fig. 2.16) the very low-temperature μ-dependence of all quantities resembles qualitatively that of the weakly interacting case only at very low temperatures. One may note that with increasing U, the energy range where the quadratic pseudogap is present is narrower (Fig. 2.8) and therefore the crossover region ii) seen at weak coupling is here restricted to very low temperature (here $T/D < 0.05$). The strong reduction of the spectral weight at the minimum of the U-shape quasiparticle feature (see Fig. 2.8) occurring around $T \simeq T^*$ at $\mu = 0$ marks here a qualitative change of the behaviour in μ of all quantities: for $T > T^*$ σ increases with increasing chemical potential as a result of the concomitant enhancement of both χ and $\mathcal{D}$ which can here be ascribed to the partial restoring of the coherent U-shape with increasing μ (see Section 2.2.1).

2.3.4 Energy crossover at nodal point

The Λ-dependent crossover seen at the nodal point in the weak coupling regime (Fig. 2.12) has a counterpart in an energy crossover for the frequency-dependent scattering rate shown in Fig. 2.17 at constant temperature $T/D = 0.02$ and scaled with the scaling factor $S^9(\Lambda)$ to compare systems with the same Fermi velocity v_F. The scaling dimensions $S^9(\Lambda)$ can be recovered from the dependence on v_F of Γ, see Eq. (A.1). The predicted polynomial behaviour of the scattering rate at nodal point [25] spanning from a constant at low energy to ω^8 at higher energies is shown here for $\Lambda/D = 1$ (see also Appendix A). For $\Lambda/D < 1$ a crossover can be seen at $\omega \simeq \Lambda$, while above this energy scale, a Fermi liquid ω^2-behaviour is recovered.

In panel b) the scattering rate is shown in the strong coupling NSM phase. For $\Lambda/D = 1$ the energy exponent again spans from 0 to 8.

For $\Lambda/D < 1$ a crossover to smaller energy exponents is found at $\omega \simeq \Lambda$ though less evident than in the weak coupling case. When the energy scale Λ approaches the order of the temperature, the low-temperature scaling fails (see Appendix B).

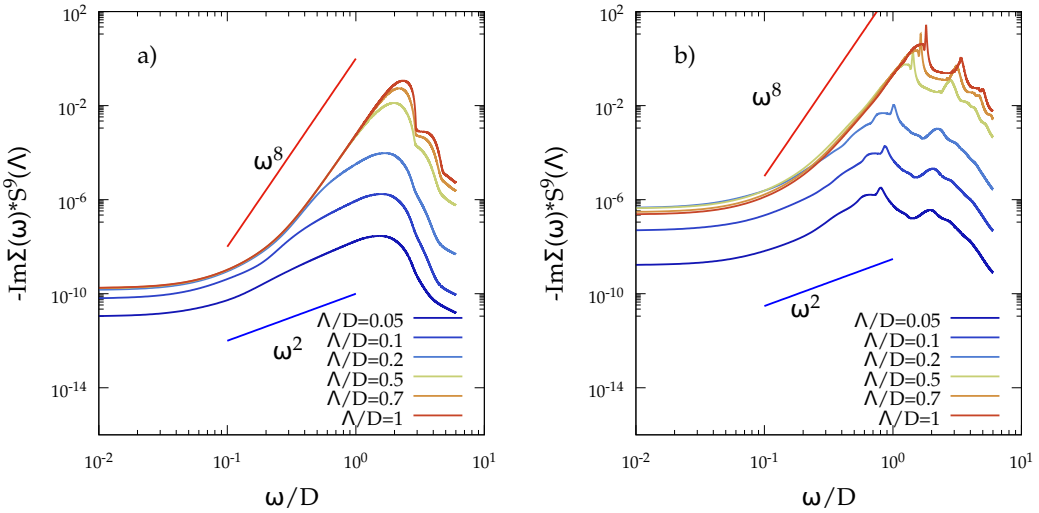


Figure 2.17: The imaginary part of the self-energy at half-filling for $U/D = 0.5$ and $T = 0.02$ scaled with $S^9(\Lambda)$ in order to obtain the same Fermi velocity of any Λ/D (a). The same quantity for $U/D = 3.0$ (b).

2.3.5 Optical Conductivity and optical damping

The energy crossover suggests that a corresponding crossover in the optical conductivity could also be observed. Using the Kubo formula 2.39 the optical conductivity is

$$Re\sigma_{xx} = \frac{\bar{\sigma} 2\pi}{\Omega} \int_{-\infty}^{+\infty} d\omega \left[f(\omega - \mu) - f(\omega - \mu + \Omega) \right] \times \\ \times \left(\int_{-D}^{D} d\epsilon \mathcal{N}(\epsilon) \left[A^{(+)} A'^{(+)} + A^{(-)} A'^{(-)} \right] + \int_{-\Lambda}^{\Lambda} d\epsilon \, 2c\epsilon^2 \left[A^{(+)} A'^{(-)} + A^{(-)} A'^{(+)} \right] \right) \tag{2.51}$$

where A' is the spectral function evaluated at $\omega + \Omega$ and A at ω. The results from the Kubo formula (Eq. 2.51) are shown in Fig. 2.18 in the weak (a) and strong coupling (b) NSM phases. Note that, the intraband contribution is obtained from Eq. 2.51 taking into account only the first term in the integral over ϵ.

Note that, our approximation for the optical conductivity 2.51 neglects the interband transitions at large energy Ω and therefore can describe accurately the optical spectra at low energy $\Omega < \Lambda$. A sharp zero frequency Lorentzian Drude peak is indeed found in Fig. 2.18, and its Ω^{-2} tail is shown. Only intraband transitions contribute to this peak. Both the amplitude and the width of this peak strongly depend on the energy scale Λ. At an energy $\omega > T$ as $T < \Lambda$ interband transitions start to contribute producing an increase in optical

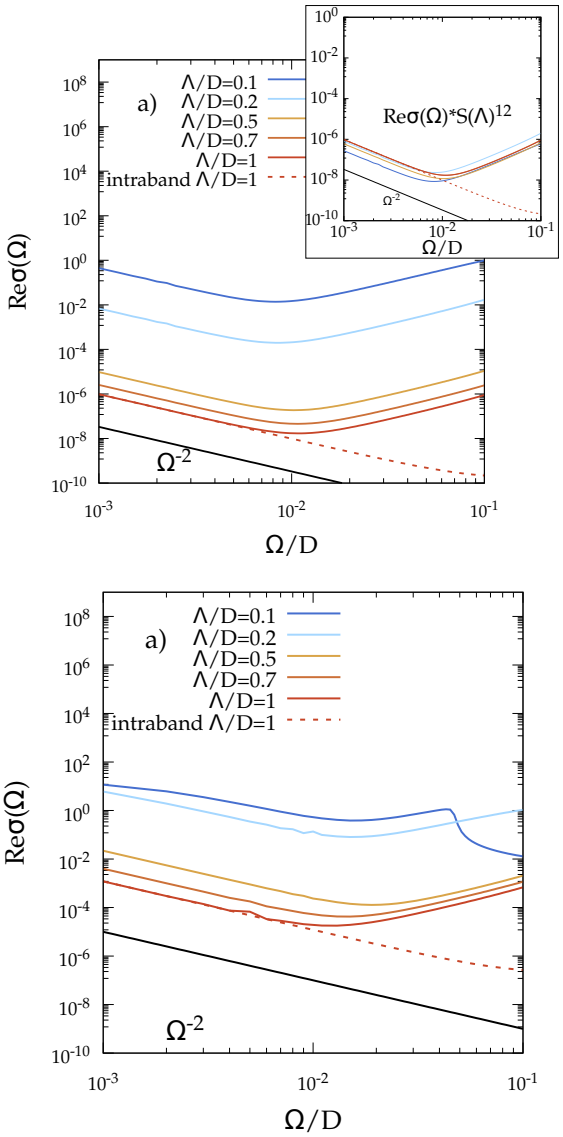


Figure 2.18: Optical conductivity at half-filling for $T/D = 0.02$ and $U/D = 0.5$ (a) and $U/D = 3.0$ (b) . The dashed red curve indicates the intraband contribution to the optical spectra at $\Lambda/D = 1$ in both panels. They are obtained by taking into account only the intraband contribution from the Kubo formula (Eq. 2.39).

absorption. Since at weak coupling the intraband absorption is of the Drude form

$$\sigma_{intra}(\Omega) = \frac{\sigma(0)\Gamma_{opt}^2}{\Omega^2 + \Gamma_{opt}^2} \tag{2.52}$$

the effect of $\Lambda/D < 1$ reduces at low temperature to simple scaling of low-frequency optical conductivity since for $\Omega > \Gamma_{opt}$ the scaling of the optical spectra reduces to the scaling of $\sigma(0)\Gamma_{opt}^2$. From the results shown in Fig. 2.12 (d) we know that $\sigma(0)$ scales with $S^6(\Lambda)$. On the other hand, as it is shown in Fig. 2.19 and derived below Γ_{opt} scales as the quasiparticle damping ($S^{-9}(\Lambda)$) and therefore at weak coupling and low temperature the scaling of low energy optical conductivity is that of $S^{-12}(\Lambda)$. The scaled optical conductivity is shown in the inset of Fig. 2.18 (a). In the strongly correlated NSM phase, the scaling does not hold but still, the low-frequency optical conductivity has a Lorentzian form with Γ_{opt} that deviates

from a simple proportionality with quasiparticle damping as shown in Fig. 2.19.

We now derive the relation between Γ_{opt} and Γ. By using the intraband part of the Kubo formula in Eq. 2.51, each term of the optical conductivity can be written as the integral over energies and frequencies of the product of two Lorentzians

$$Re\sigma_{i,j}(\Omega) = \frac{\bar{\sigma}2\pi}{\Omega}\int_{-\infty}^{+\infty} d\omega\,[f(\omega-\mu)-f(\omega-\mu+\Omega)]\times \\ \times\int d\epsilon\mathcal{N}(\epsilon)\frac{\Gamma(\omega)}{(\omega-Re\Sigma(\omega)-\epsilon)^2+\Gamma^2(\omega)}\frac{\Gamma(\omega+\Omega)}{(\omega+\Omega-Re\Sigma(\omega+\Omega)-\epsilon)^2+\Gamma^2(\omega+\Omega)} \tag{2.53}$$

$$= \frac{\bar{\sigma}2\pi}{\Omega}\int_{-\infty}^{+\infty} d\omega\,[f(\omega-\mu)-f(\omega-\mu+\Omega)]\times I(\omega,\Omega) \tag{2.54}$$

Let $\Gamma(\omega)=\Gamma_1$, $\Gamma(\omega+\Omega)=\Gamma_2$ and $\omega-Re\Sigma(\omega)=\epsilon_1$, $\omega+\Omega-Re\Sigma(\omega+\Omega)=\epsilon_2$, then the integral in energy ϵ can be made using the specific model with $\Lambda/D=1$ and the corresponding quadratic density of states $\mathcal{N}(\epsilon)=3\epsilon^2/2D^3$

$$I(\omega,\Omega)=\int d\epsilon\mathcal{N}(\epsilon)\frac{\Gamma_1}{(\epsilon_1-\epsilon)^2+\Gamma_1^2}\cdot\frac{\Gamma_2}{(\epsilon_2-\epsilon)^2+\Gamma_2^2}=\frac{3\pi}{2D^3}\frac{\Gamma_1\epsilon_2^2+\Gamma_2\epsilon_1^2+\Gamma_1^2\Gamma_2+\Gamma_2^2\Gamma_1}{(\epsilon_1-\epsilon_2)^2+(\Gamma_1+\Gamma_2)^2} \tag{2.55}$$

Hence, we perform some approximations: i) we neglect the real part of the self-energy ii) we take a constant imaginary part of the self-energy in the limit of $\omega \ll T$ and $\Omega \ll T$ ($\Gamma_1=\Gamma_2=\Gamma$).

The optical conductivity is thus

$$Re\sigma_{i,j}(\Omega)=\frac{3\pi^2}{2D^3}\int_{-\infty}^{+\infty} d\omega\left(-\frac{\partial f}{\partial\omega}\right)\frac{\Gamma(\omega^2+(\omega+\Omega)^2)+2\Gamma^3}{\omega^2+(2\Gamma)^2} \tag{2.56}$$

since the derivative of the Fermi function can be written as

$$-\frac{\partial f(\omega)}{\partial\omega}=\frac{1}{2}\frac{\beta}{1+cosh(\beta\omega)} \tag{2.57}$$

then the integral over the frequencies is

$$Re\sigma(\Omega)=\frac{3\pi}{2D^3}\frac{\Gamma}{\Omega^2+(2\Gamma)^2}\left(\frac{2\pi}{3\beta^2}+2\Gamma^2+\Omega^2\right) \tag{2.58}$$

In the range $\Gamma \ll \Omega, \omega \ll T$

$$Re\sigma(\Omega)=\frac{\pi^3}{D^3\beta^2}\frac{\Gamma}{\Omega^2+(2\Gamma)^2} \tag{2.59}$$

then the optical damping is twice as the quasiparticle damping ($\Gamma_{opt}=2\Gamma$).

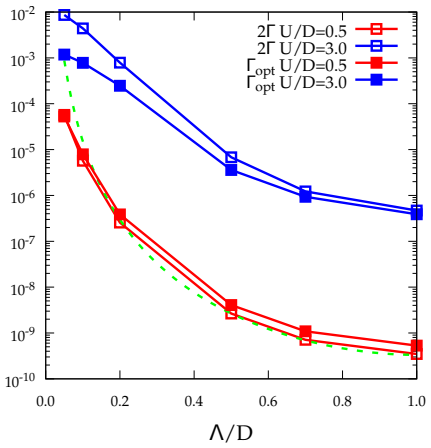


Figure 2.19: Γ_{opt} and Γ at half-filling for $T/D = 0.02$ and $U/D = 0.5$ and $U/D = 3.0$. The dashed green line represents the Λ/D dependence from the perturbation theory (Eq. A.1).

As it is shown in Fig. 2.19 the optical scattering rate at weak coupling does depend strongly on the amplitude of the energy scale Λ through the same scaling function introduced in Fig. 2.12 since $\Gamma_{opt} \simeq 2\Gamma$. Scaling does not hold in the NSM strongly correlated phase where Γ_{opt} is not simply proportional to the scattering rate as shown in Fig. 2.19. Although the qualitative dependence on Λ is similar in both cases, we notice a significative deviation of the optical scattering rate from its estimate based on the quasiparticle scattering rate when non-linear deviations become important.

CHAPTER 3

KONDO SCREENING IN INTERACTING NODAL SEMIMETALS

In the previous chapter, we uncovered evidence from many-body calculations suggesting the presence of Kondo effect signatures in nodal semimetals as the temperature decreases. Although earlier studies showed that the Anderson impurity model describing an impurity coupled to a pseudogapped conduction band does not exhibit the Kondo effect [24], our DMFT calculations reveal a key difference in the associated Anderson impurity model. In the case of nodal semimetals, despite the vanishing of the DOS at the impurity level, the impurity itself is infinitely coupled to the conduction bath. This distinction allowed us to explore this novel impurity model and verify its consistency with the Kondo effect.

In this chapter, I will present the signatures of the Kondo effect in both conventional metals and nodal semimetal materials. Furthermore, I will analyze the behavior of spin susceptibility of the Anderson model associated with the DMFT solution of nodal semimetals and emphasize the distinctive effects of the screening of the local moments in the impurity model.

This Chapter is part of the previously mentioned work *M. Fischer, A. Poli, L. Crippa, S. Ciuchi, M. Vojta, A. Toschi, and G. Sangiovanni, arXiv:2503.14326 (2025)* [27].

3.1 Kondo screening in the impurity model

A starting point for the study of strongly correlated electrons was the discovery of the mechanism behind the Kondo screening in magnetic alloys [66]. These materials are modelized as magnetic impurities embedded in a sea of conduction electrons. The susceptibility of these magnetic impurities in metals is described by Curie-Weiss law

$$\chi = \frac{C}{T + \Theta} \tag{3.1}$$

where the case of a single spin S in a conduction bath has $\Theta = 0$ and $C = \frac{4\mu_B^2 S(S+1)}{3K_B}$. Typically, the susceptibility of an impurity in a dilute metallic alloy has a $\Theta \neq 0$ which means it has Curie-Weiss behaviour down to a temperature where it saturates in a constant paramagnetic susceptibility [67]. This anomalous behaviour was initially explained with the $s - d$ model,

to capture how a magnetic local moment interacts with mobile electrons [68]. Jun Kondo in his work [22] solved this model in the framework of perturbation theory, expanding up to the third order in the coupling J, between the local moments and the bath, demonstrating that as the temperature decreases, the effective strength of the interaction increases logarithmically. From this solution, perturbation theory breaks below the Kondo temperature

$$T_K \propto \exp\left(-\frac{E_F}{J}\right) \tag{3.2}$$

where E_F is the Fermi energy of conduction electrons. Later, Anderson introduced a model of a non-magnetic impurity interacting with a conduction bath, incorporating local interactions at the impurity site (Eq. 1.32). This model could be linked to the Kondo model, with the interaction explaining the formation of the local magnetic moment. Extensions to this model were then introduced to study the divergence of the coupling at low temperatures, as perturbation theory was unable to fully capture the divergent behavior.

The following studies culminated in Wilson's introduction of a non-perturbative method, the "numerical renormalization group" [69]. This method, based on scaling theory developed in condensed matter physics and field theories from high-energy physics, predicted that at low temperatures, the ground state is a singlet formed between the impurity and conduction electrons, with infinite coupling between them. As a result the magnetic impurity forms a singlet with one conduction electron leaving a magnetic *screened* spinless impurity and therefore the conduction electrons would eventually scatters elastically with it. For the same reasons the spin susceptibility will converge at low temperature to a constant value.

3.2 Kondo screening in interacting materials

The most prominent effects of Kondo screening are observed in materials later termed "heavy fermions." These compounds typically feature a regular sublattice of 4f or 5f atoms, such as Ce, Yb, or U. Heavy fermion materials are often close to a magnetic instability that leads to long-range magnetic order, arising from interactions between the 4f or 5f magnetic moments mediated by conduction electrons. This makes these materials an ideal platform for studying the effects of strong magnetic interactions in solids. The large magnetic interactions in these systems result in an extraordinary many-body renormalization of the carriers' effective mass, with $m^*/m \sim 1000$, while Fermi liquid theory remains valid at sufficiently low temperatures [2–5].

Self-consistent band structure calculations fail to capture this significant mass enhancement. However, many-body techniques, such as those based on the Dynamical Mean-Field Theory (DMFT) framework, successfully explain this phenomenon. DMFT predicts the emergence of renormalized bands at the Fermi level due to the formation of coherent states. In strongly correlated systems, the temperature range over which Fermi liquid behavior is observed—the coherence temperature T_c—is often very narrow. The coherence temperature is typically inversely proportional to the effective mass enhancement, making it much smaller than the Fermi temperature. Above T_c, physical properties are dominated by strong incoherent electron-electron scattering. In this high-temperature regime, local magnetic moments

form as the local electron interaction U increases, laying the groundwork for Kondo screening as the temperature decreases.

In the DMFT solution of the Hubbard model (Fig. 1.3), the correlated density of states exhibits a three-peak structure, consisting of a coherent quasiparticle peak at the Fermi level and two Hubbard bands. This structure reflects the coexistence of itinerant and localized electrons. Localized electrons act as magnetic moments immersed in a conduction bath. Signatures of local moment formation are observable in transport quantities, such as the charge compressibility, which exhibits a sharp decrease near the coherence temperature T_c in the strongly correlated Fermi liquid phase [65]. This behavior contrasts sharply with the weakly correlated phase, where the charge compressibility decreases smoothly with temperature due to the broadening of the Fermi-Dirac distribution function.

The connection between the impurity problem and the lattice problem can be examined by analyzing the characteristic temperatures associated with screening phenomena in both models. In the single impurity Kondo model, the Kondo temperature T_K marks the crossover from the local moment regime to the screened local moment regime. In heavy fermion systems, which correspond to high-density magnetic impurity systems, the coherence temperature T_c is significantly lower than T_K [70]. Various methods have been developed to determine T_K, including approaches based on the eigenvalues of the two-particle generalized susceptibility computed in imaginary frequencies. In such methods, T_K is identified as the temperature at which the first and second eigenvalues intersect [61].

3.3 Signatures of Kondo screening in a nodal semimetal

Similar to conventional metals, the signatures of Kondo screening in nodal semimetal materials can be identified through their charge compressibility and spin susceptibility. Analyzing the compressibility in Fig. 2.13 b) the arising of a possible Kondo screening has been discussed (Par. 2.3.2).The compressibility exhibits a T^2 growth with increasing temperature, consistent with the behavior expected for a gas of electrons with a quadratically dispersed density of states. However, a step-like feature occurs with increasing temperature, which has been interpreted in Ref. [65] as a deviation from coherent Fermi liquid behavior. This deviation suggests the formation of local moments, where the environment fails to fully screen them.

This step was initially surprising, as the density of states vanishes at the Fermi level in nodal semimetals leaving no conduction electron to screen the impurity spin. Previous studies employing the renormalization group approach have demonstrated that Kondo screening does not occur in the Anderson impurity model with a quadratically vanishing hybridization function at the Fermi level [24]. This result is intuitive: if the number of metallic states near the impurity energy vanishes, the screening effect is suppressed.

Going back to the lattice model, in a Bethe lattice and for any metallic density of states the hybridization function (Eq. 1.34) is proportional to the density of states at the Fermi level and it remains finite, as does the density of states.

Instead, the semimetallic density of states does not directly represent the hybridization function for the impurity model associated with nodal semimetals (Eq. 1.34). When the local density of states vanishes and considering the system before the Mott transition where the

self-energy is finite when $\omega = 0$, the hybridization function diverges at the Fermi level and remains regular elsewhere. This behavior is evident from the local Green's function,

$$G_{loc}(\omega) = \frac{1}{G_0^{-1}(\omega) - \Sigma(\omega)} = \frac{1}{\omega - \Delta(\omega) - \Sigma(\omega)}. \tag{3.3}$$

At zero frequency (the Fermi level), the local Green's function vanishes, $G_{loc}(\omega = 0) = 0$. Since the self-energy, $\Sigma(\omega)$, is finite, the hybridization function, $\Delta(\omega)$, must diverge. The local Green's function and the calculated hybridization function are shown in Fig. 3.1 for two different values of the interaction strength U, both of which are below the first-order transition. In the Mott insulating phase, the vanishing density of states is compensated by a diverging self-energy. Here, the vanishing density of states is instead compensated by the hybridization function, as the self-energy remains finite.

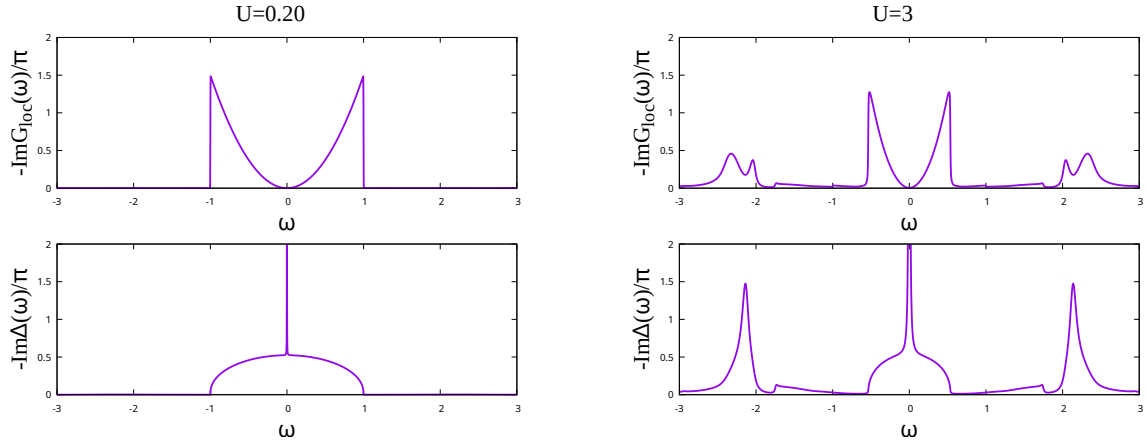


Figure 3.1: Imaginary part of the local Green's function and the hybridization function for two different interaction strengths $U = 0.2$ and $U = 3.0$. When the density of states vanishes the hybridization function diverges even at higher U, but $U < U_{c2}$.

3.4 Anderson Impurity model with singular hybridization function

Motivated by the DMFT study of the interacting semimetal, in the work [27], an Anderson model with singular hybridization function has been considered. It is characterized by an impurity coupled to a conduction electron bath via a hybridization function that diverges at the Fermi level. The Hamiltonian for this system corresponds to the standard Anderson impurity model

$$\begin{aligned}
\hat{H}_0 &= \sum_{\sigma} \epsilon_{\mathrm{d}}\, \hat{c}^{\dagger}_{\mathrm{d}\sigma}\, \hat{c}_{\mathrm{d}\sigma} \;+\; U\, \hat{n}_{\mathrm{d}\uparrow}\, \hat{n}_{\mathrm{d}\downarrow} \\
\hat{H}_{\mathrm{bath}} &= \sum_{l\sigma} \epsilon_{l\mathrm{F}}\, \hat{c}^{\dagger}_{1l\sigma}\, \hat{c}_{1l\sigma} \\
\hat{H}_{\mathrm{hyb}} &= \sum_{l\sigma} V_l \left(\hat{c}^{\dagger}_{1l\sigma}\, \hat{c}_{\mathrm{d}\sigma} \;+\; \hat{c}^{\dagger}_{\mathrm{d}\sigma}\, \hat{c}_{1l\sigma} \right) \\
\hat{H} &= \hat{H}_0 \;+\; \hat{H}_{\mathrm{bath}} \;+\; \hat{H}_{\mathrm{hyb}}\,.
\end{aligned} \tag{3.4}$$

$\hat{H}_0$ represents the Hamiltonian for the impurity site, $\hat{H}_{\text{bath}}$ describes the bath, and $\hat{H}_{\text{hyb}}$ accounts for the hybridization V_l between the impurity and the bath. The operators $\hat{c}^{(\dagger)}_{\text{d}\sigma}$ and $\hat{c}^{(\dagger)}_{1l\sigma}$ are the annihilation (creation) operators for electrons at the impurity site and in the bath, respectively. The energy level of the impurity site is given by ϵ_{d}, while $\epsilon_{l,\text{F}}$ refers to the energy levels in the bath. The term U denotes the on-site interaction on the impurity when it is doubly occupied, and the index l accounts for the orbital and site degrees of freedom in the bath.

As a model introducing singularity in the hybaridization function we consider the following model

$$-\frac{1}{\pi}\,\text{Im}\left[\Delta(\omega)\right] = V^2\left((1-\alpha)\ \text{Flat}\left[-\Lambda:\Lambda\right] + \alpha\,\delta(\omega)\right). \tag{3.5}$$

where "Flat" is a function representing the regular part modelized as a constant box between $-\Lambda$ and Λ and "$\delta(\omega)$" is the dirac function. α is a varying parameter in $[0,1]$. This function is reproduced in Fig. 3.2.

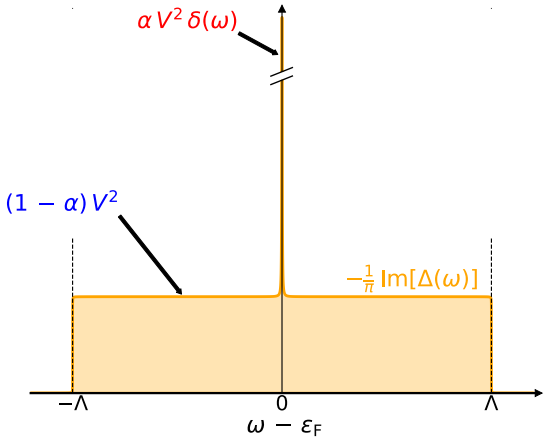


Figure 3.2: Hybridization function of the considered Anderson impurity model. The parameter $\alpha \in [0,1]$ and when $\alpha = 0$ the hybridization is flat and when $\alpha = 1$ the hybridization is a delta function [27].

For $\alpha = 0$ the Anderson impurity model has a constant hybridization function When $\alpha = 1$, the model features a delta-shaped hybridization function and is effectively equivalent to a Kondo dimer. The properties of this latter model can be calculated analytically and the model is analyzed in the next section to investigate whether it exhibits the Kondo effect.

3.5 Correlation function study of the Kondo dimer

The Kondo dimer consists of an impurity (d) coupled to only one state in the bath (1). Only the impurity contains a short-range Coulombian repulsion.

$$H = \epsilon_F \sum_\sigma c^\dagger_{1,\sigma} c_{1,\sigma} + \epsilon_F \sum_\sigma c^\dagger_{d,\sigma} c_{d,\sigma} + V \sum_\sigma \left(c^\dagger_{1,\sigma} c_{d,\sigma} + c^\dagger_{d,\sigma} c_{1,\sigma} \right) + U n_{d,\uparrow} n_{d,\downarrow} - h\sigma_z \tag{3.6}$$

Both the state in the bath and the impurity have energy ϵ_F, the coupling constant between the bath and the impurity is V and U is the repulsive on-site term in the impurity. In this

model we considered explicitly an external perturbation h which couples with the spin in the $z-$direction ($\sigma_z = c^\dagger_{d,\uparrow}c_{d,\uparrow} - c^\dagger_{d,\downarrow}c_{d,\downarrow}$). This choice has been done to better calculate the spin susceptibility with the thermodynamic relation that I will show in the next paragraph.

3.5.1 Local spin susceptibility of the Kondo Dimer

The local spin susceptibility is a valuable quantity for revealing the effects of Kondo screening in a system. As previously discussed, the susceptibility exhibits two distinct behaviors: a Curie-Weiss type associated with the presence of local moments and a constant value characteristic of Pauli paramagnetism.

In the case of the Kondo dimer, the local spin susceptibility has been calculated within both the canonical ensemble, considering particle numbers from 0 to 4, and the grand canonical ensemble. This calculation is performed within the framework of thermodynamics, where the susceptibility is defined as the derivative of the magnetization with respect to an applied local magnetic field acting on the impurity

$$\chi^s_{loc} = \frac{\partial m}{\partial h} \tag{3.7}$$

The full calculations are exposed in Appendix D.

In the canonical ensemble, the magnetization is

$$< \sigma_z >= m_N = \frac{Tre^{-\beta\hat{H}}\hat{\sigma}_z}{Tre^{-\beta\hat{H}}} = \frac{\sum_n e^{-\beta E_n}\langle v_n|\hat{\sigma}_z|v_n\rangle}{\sum_n e^{-\beta E_n}} \tag{3.8}$$

where σ_z is the Pauli matrix and E_n and $|v_n\rangle$ are eigenvalues and eigenvectors associated to the n-state. N is the number of particles.

The magnetization in the grand canonical ensemble is:

$$< \sigma_z >= \frac{Tre^{-\beta(\hat{H}-\mu\hat{N})}\hat{\sigma}_z}{Tre^{-\beta(\hat{H}-\mu\hat{N})}} = \frac{\sum_N e^{\beta\mu N}\sum_n e^{-\beta E_n} < v_n|\hat{\sigma}_z|v_n >}{\sum_N z^N \sum_n e^{-\beta E_n}} = \frac{\sum_N z^N < \sigma_z >_N Z_N}{\sum_N e^{\beta\mu N} Z_N} \tag{3.9}$$

where Z_N and $< \sigma_z >_N$ are the partition function and the magnetization with $N-$particles, and $z = e^{\beta\mu}$.

To determine whether the system is at half-filling, we calculated the average number of particles obtained from the grand canonical partition function $\mathcal{Z}_{gcan}$

$$< n >=< n_\uparrow + n_\downarrow >= \frac{1}{\beta}\frac{\partial}{\partial\mu} log(Z_{gcan}) \tag{3.10}$$

For different temperatures, it can be observed that the system reaches half-filling ($n = 2$) when $\mu = 0$ (Fig. 3.3).

At half-filling, the spin susceptibility is shown in Fig. 3.4 a) for ($U = 5.75$) and ($V = 2.0$). The susceptibility calculated in the grand canonical ensemble is compared with that obtained in the canonical ensemble for ($N = 2$) and for ($N = 1$) or ($N = 3$) (which exhibit the same

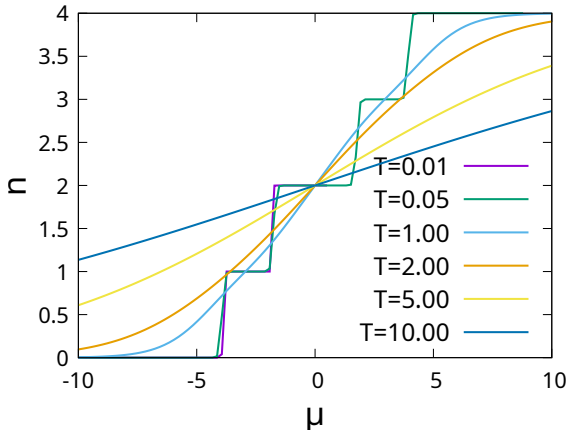


Figure 3.3: Total average number of particles measured in the Grand Canonical ensemble, at different Temperatures as a function of the chemical potential.

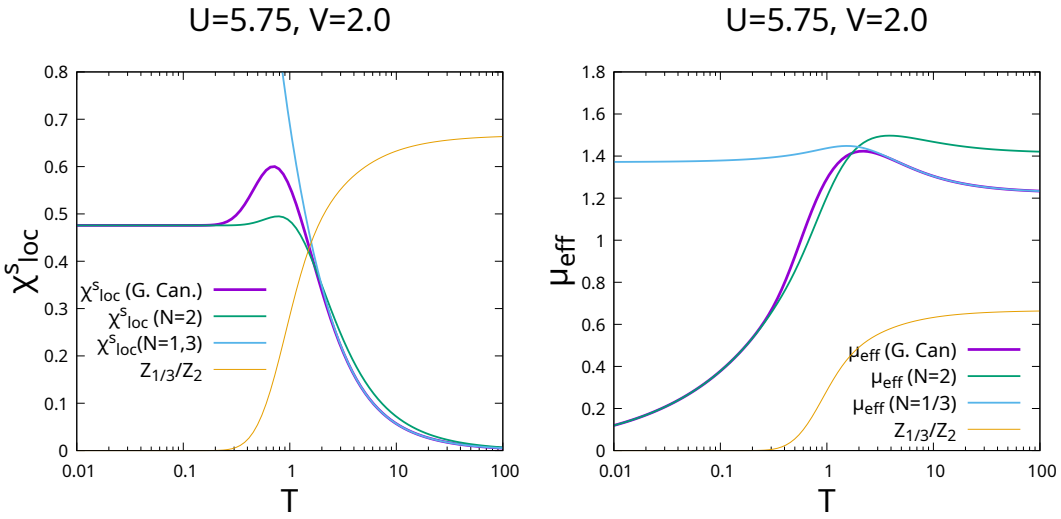


Figure 3.4: a) Spin susceptibility in the Grand Canonical ensemble with $U = 5.75$, $V = 2.0$ and $\mu = 0$ and spin susceptibility in the Canonical ensemble with $N = 2$ and $N = 1, 3$. Reciprocal weight of the states with 1,3 particles and 2 particles are shown. b) effective local moment defined as $\mu_{eff} = \sqrt{3T\chi^s_{loc}}$.

magnetization). It can be observed that the overall behavior of the spin susceptibility results from a combination of these contributions. At high temperatures, the susceptibility follows a Curie-law-like behavior, scaling as $(1/T)$, consistent with magnetic states corresponding to configurations with one or three particles. As the temperature approaches zero, the behavior is dominated by the two-particle sector, where the singlet state becomes the ground state, indicating that Kondo screening is active. The ratio of the weights of these states is also shown.

To gain further insight into the behavior of the local moments, we calculated the effective magnetic moment

$$\mu_{eff} = \sqrt{3T\chi^s_{loc}} \tag{3.11}$$

Fig. 3.4 b) shows that the effective magnetic moment of the 1- and 3-particle states (light blue line) is higher and remains constant at low temperatures. This behavior is Curie-like, corresponding to the magnetic states occupied at low temperatures. As the temperature

increases, the effective moment retains a Curie-like behavior but with a different slope due to the involvement of additional states. The effective moment of the 2-particle states (green line) is low at low temperatures, indicating the screening of the magnetic moments. At higher temperatures, the magnetic states of the triplet become occupied, leading to an increase in the effective moment for the 2-particle states. In the grand canonical ensemble (violet line), the system is dominated at low temperatures by the 2-particle states, while at high temperatures, the 1- and 3-particle states dominate. This behavior arises from the changing relative weights of these states (yellow line).

In this way, it is possible to explain how the screening in the Kondo dimer works. At low temperatures, it is not strictly a screening, but rather involves just 2 electrons forming a singlet state with total spin equal to zero. Additionally, the peak in the effective moment arises from the change in the states contributing to the susceptibility, from magnetic states at high temperatures to non-magnetic states at low temperatures.

3.5.2 Comparison with numerical calculation

The impurity model can be studied numerically at any value of the parameter α. To achieve this, a solution with the Dynamical Mean-Field Theory (DMFT) solver by continuously varying the parameter α of the hybridization function from $\alpha = 0$ to $\alpha = 1$ has been obtained [27]. The solution was computed using a Continuous-Time Quantum Monte Carlo (CT-QMC) impurity solver, which operates in imaginary frequency space and is numerically exact [60]. This method enables the calculation of response functions at the impurity site like the spin susceptibility (the reaction of the system to an applied field in $z-$direction) and charge compressibility for different values of α.

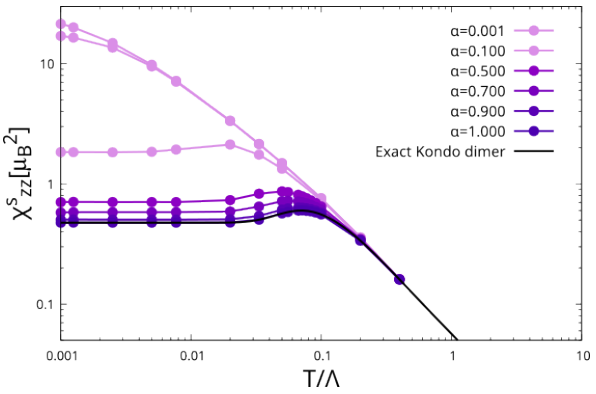


Figure 3.5: Numerical calculation of the spin susceptibility for different values of the parameter for the hybridization function α close to $\alpha = 1$. The calculations have been done at the interaction value of $U = 5.75$ and the coupling potential with the bath $V = 2.0$. The exact solution (black line) is the analytical spin susceptibility for a Kondo dimer. The data are part of the work in the paper [27].

The main results are presented in Fig. 3.5, where the analytical spin susceptibility calculated for the Kondo dimer is compared with numerical calculations. For $\alpha = 0$ or α close to zero, the system corresponds to the conventional Anderson model with a finite hybridization function. In this regime, the spin susceptibility exhibits a Curie-Weiss behavior at high temperatures but becomes constant as the temperature decreases to low values.

In contrast, the behavior for $\alpha = 1$ or α close to 1 differs significantly at intermediate

temperatures, where a pronounced peak emerges in the spin susceptibility. This peak is consistent with the predictions from the analytical calculations mentioned earlier and illustrated in Fig. 3.4.

Another quantity that we extrapolate from the numerical solution is the effective local moment with Eq. 3.11. In Fig. 3.6 it is shown for different values of α and U. The effective moments for $\alpha = 1$ are calculated analytically, those for $\alpha = 0$ are calculated numerically. The model shows at any value of the parameter α an increase of the effective moment by decreasing temperature and a subsequent decreasing when the temperature is smaller. This is a signature of the Kondo effect because at low temperatures the local moments are screened and the effective momentum vanishes.

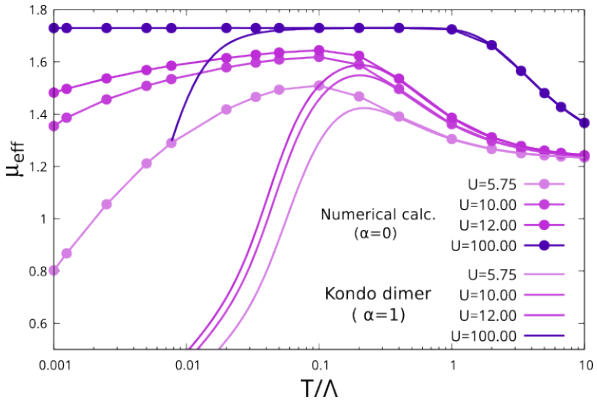


Figure 3.6: Effective moment calculated for models with different values of the parameter α. The calculation for $\alpha = 1$ are the same calculated analytically and shown in Fig. 3.4 right). The numerical data are taken from the work [27].

CHAPTER 4

INTERPLAY BETWEEN ELECTRONIC AND INTERACTIONS AND QUENCHED AND ANNEALED DISORDER

Extensive studies have examined the interplay between electronic correlations and disorder, revealing complex phases and unusual transport properties across various materials. For instance, κ-type organic conductors exhibit a remarkable sensitivity to hydrostatic pressure, which has enabled the discovery of multiple phases within a relatively accessible pressure range [71]. These phases have been investigated theoretically, often at temperatures above the coherence temperature [72, 73]. Under specific conditions, studies show that the addition of disorder can induce metallization in a Mott insulator – a phenomenon also observed experimentally in κ-organics [17, 74]. A "bad metallic" behaviour has been reported near the Mott transition at temperatures above the coherence temperature, where quasiparticles are no longer well defined [75].

At low temperatures, the Fermi liquid (FL) phase is also expected to be impacted by the disorder, with the scattering time and resistivity displaying two distinct trends with temperature: in addition to the T^2 component due to inelastic scattering from electron-electron interactions, a residual, T-independent scattering arises due to elastic collisions, which is responsible for the finite resistivity in the $T \to 0$ limit. Although Matthiessen's rule might be expected to apply for weak interactions, this assumption becomes questionable in the presence of strong interactions, where the interplay between disorder and correlations can significantly shift the Mott transition to larger interaction values [76].

Extensive studies carried on using DMFT and generalisations to take into account Anderson localization effects have pointed out that a form of screening of disorder should be present in interacting disordered systems which becomes complete at the Mott transition [77]. On the other hand Anderson transition itself is strongly affected by disorder [76]. While these theoretical approaches aimed at explaining the phase diagram in the vicinity of transitions both Mott or Anderson type we instead focus our attention to the Fermi liquid phase and emphasize the interplay between disorder and interactions that is still present there and leads to some unexpected results.

The bulk of this chapter is the object of a work which is currently in the arXiv [28]. In this work, we combine dynamical mean-field theory (DMFT) with the Coherent Poten-

tial Approximation (CPA), to study the interplay between electron-electron correlations and disorder in the Fermi liquid state. Previously applied in Ref. [78] to examine the interplay electron-phonon interactions with the disorder, this method allows us to demonstrate that residual resistivity – or equivalently, the residual scattering rate – is itself renormalized by electron-electron interactions. Specifically, we observe that as the interaction strength increases, the scattering rate intercept behaves as though the system were experiencing a lower disorder level, suggesting an effective "renormalization" of disorder by correlations. Interestingly, this renormalization is not symmetric: while disorder is significantly renormalized by electron-electron interactions even at low interaction, the reverse is true only when the system is in the range of intermediate to strong disorder. The properties of the Fermi liquid itself, embodied in the temperature dependence of the scattering rate arising from electron-electron interactions, are mostly unaffected by the presence of small disorder.

4.1 Quenched and annealed disorder

Electron correlations and randomness–such as impurity configurations or variations in chemical composition–are intrinsic features of real materials. To disentangle their individual effects on electron behavior, it is useful to analyze them separately. This section first presents the a simple model for local uncorrelated disorder in absence of interactions, followed by an introduction to two distinct types of disorder: quenched and annealed. Quenched disorder refers to a fixed probability distribution, typically associated with static defects or site-dependent variations in the atomic potential. In contrast, annealed disorder involves a temperature-dependent probability distribution that dynamically interacts with the electronic system. The latter being a model for interaction with classical phonons at temperatures larger than the typical phonon frequencies.

4.1.1 Coherent Potential Approximation for quenched disordered systems

The simplest model of disorder in metals – crystalline solids with conduction electrons – consists of a Fermi gas of electrons moving and scattering off immobile ions, whose atomic potentials fluctuate from site to site. The general Hamiltonian for such an electron is given by the Anderson Hamiltonian [79]

$$H = -t \sum_{\langle i,j \rangle \sigma} (\hat{c}^{\dagger}_{i\sigma} \hat{c}_{j\sigma} + \hat{c}^{\dagger}_{j\sigma} \hat{c}_{i\sigma}) + \sum_{i} \xi_i \hat{n}_i \tag{4.1}$$

with the usual $\hat{c}_i^{(\dagger)}$ annihilation (creation) operator for a fermion in the state i, and the number operator $\hat{n}_i = \hat{c}_i^{\dagger} \hat{c}_i$. ξ_i are independent randomly distributed variables with a distribution $P(\xi)$.

Systems where there is random disorder are not easy to solve exactly due to the lack of translational invariance. One exception is the one-dimensional system. In general, one has to use approximations. In the framework of Mean Field Theories, the Coherent Potential Approximation (CPA) was developed to address disordered systems and to calculate one-particle quantities. This method was originally introduced independently by P. Soven and D. W. Taylor [80, 81], with a comprehensive review provided in ref. [82]. CPA solution has

been observed to be identical to the self-consistent DMFT equations determining the Green's function in the limit of high dimensions i.e. the limit of high coordination number Z [83].

In order to solve the Hamiltonian Eq. 4.1 using DMFT one should find the local averaged Green's function that can be written as the average over the disorder configurations ($\langle \cdots \rangle_{\{\xi_i\}}$) of the single-site random Green's function

$$G_{loc}(\omega) = \left\langle \hat{G} \right\rangle_{\{\xi_i\}} = \left\langle \frac{1}{\omega - \hat{H}(\omega, \{\xi_i\})} \right\rangle_{\{\xi_i\}} \tag{4.2}$$

CPA approximation consists in finding a self-consistent not random mean-field G_0 that gives an approximated form for the single site Green's function

$$\hat{G}(\omega, \xi_i) = \frac{1}{G_0^{-1}(\omega) - \xi_i} \tag{4.3}$$

The G_0 can be found using an auxiliary Anderson impurity model (Eq. 1.32 without the U term and where $\epsilon_d = \xi$)

$$G_0^{-1}(\omega) = \omega - \Delta(\omega) \tag{4.4}$$

where $\Delta(\omega)$ is the hybridization function (Eq. 1.34).

In the limit of infinite dimensions or coordination number Z, the G_0 becomes self-averaging and independent on the site (Sec. 1.4.1). In this way, G_0 can equivalently be described as the effective medium for a system with a local non-random potential which is the self-energy

$$G_0^{-1}(\omega) = G^{-1}(\omega) + \Sigma(\omega) \tag{4.5}$$

and G_{loc} is the local averaged Green's function over the disorder configurations $G_{loc} = \langle \hat{G} \rangle_{\{\xi_i\}}$, which in infinite dimension correspond to the average over the sites

$$G_{loc}(\omega) = \int P(\xi) \frac{1}{G_0^{-1}(\omega) - \xi} d\xi \tag{4.6}$$

where $P(\xi)$ is the disorder probability distribution.

The quenched disorder model characterizes materials where disorder is extrinsic, such that introduced by doping or irradiation. In such cases, the disorder follows a fixed distribution. The considered probability distribution in this chapter is a zero-mean Gaussian with variance W^2

$$P(\xi) = \frac{e^{-\frac{\xi^2}{2W^2}}}{\sqrt{2\pi W^2}} \tag{4.7}$$

CPA calculations using gaussian distribution will turn out to be useful also in the case of annealed disorder as detailed in Sec. 4.1.3.

Despite its name, the Coherent Potential Approximation (CPA) does not capture coherent effects and cannot predict an Anderson transition. Indeed, Anderson demonstrated [79] that strong disorder can lead to destructive interference of scattered electron waves, resulting in their localization. In this localized state, the wavefunction's envelope decays exponentially from a point r_0 in space. Localization effects are especially pronounced in one-dimensional systems, where it can be rigorously shown that all electron eigenstates become localized with

any degree of disorder [84]. This phenomenon prevents charge transport in infinitely long one-dimensional wires, rendering quantum wires insulating.

An Anderson insulator is fundamentally different from a conventional insulator. Unlike band insulators, which have a band gap that blocks current, an Anderson insulator exhibits insulating behaviour because all quantum states near the Fermi level are localized, immobilizing charge carriers.

This limitation of CPA arises from its reliance on an incoherent averaging of states in the mean-field G_0, rather than accounting for the coherent overlap between states. The approximation predicts very well the spectral quantities in any dimension if sufficiently far from band tails where large deviations effects are relevant. The difficulty emerges with two-particle correlations, such as conductivity, because these states are localized.

To clarify, in absence of interactions, to compute conductivity, we must average the product of two Green's functions. In low-dimensional systems, however, there's a marked difference between averaging the product of these Green's functions and taking the product of their averages. In such systems, the Green's functions are strongly correlated, and averaging them tends to suppress these correlation effects. This limitation is particularly significant in one- and two-dimensional systems, where the constraints on electron paths enhance the impact of these correlations. In contrast, in three-dimensional systems with a high density of states at the Fermi level, numerous available electron paths reduce the likelihood of strong correlations, making this limitation less pronounced.

4.1.2 Annealed disordered systems (Classical phonons)

In contrast, another type of disorder is intrinsic to the system and varies self-consistently with temperature. This type of disorder is known as an annealed disorder, an example is given by electrons interacting with classical phonons. The simplest Hamiltonian describing hopping electrons interacting with local oscillators is the Holstein model [85, 86]

$$H = -t \sum_{\langle i,j \rangle \sigma} (\hat{c}^\dagger_{i\sigma} \hat{c}_{j\sigma} + \hat{c}^\dagger_{j\sigma} \hat{c}_{i\sigma}) + \sum_i \left(\frac{\hat{P}_i^2}{2M} + \frac{K \hat{X}_i^2}{2} \right) - g \sum_i \hat{X}_i \hat{n}_i \tag{4.8}$$

The first term corresponds to the hopping Hamiltonian for the electrons discussed in the Hubbard model. The second term represents the free Einstein's phonons, with the phonon coordinates $\hat{X}_i$ and the conjugate momenta $\hat{P}$. M are the oscillators' mass, $K = M\omega_0^2$ their elastic constant, ω_0 the characteristic frequency of the phonons. This last term represents a local potential on the $i-$site The third term represents the electron-phonon interaction, characterized by the coupling constant g between the total density of electrons in the $i-$site $\hat{n}_i = \hat{c}^\dagger_{i\uparrow} \hat{c}_{i\uparrow} + \hat{c}^\dagger_{i\downarrow} \hat{c}_{i\downarrow}$ and the oscillators' displacement.

At high temperatures, when $T \gg \omega_0$, oscillators can be treated as classical and X_i represent the lattice displacements of each i site and behave as classical variables. These displacements acquire a temperature-dependent distribution, reflecting the thermal fluctuations of the lattice. In the classical limit $\omega_0 \to 0$ and M diverges keeping K constant, the kinetic phonon term in Eq. 4.8 can be neglected.

A characteristic electron-phonon coupling energy can be obtained by minimizing the

phonon energy neglecting the elecron hopping, the associated lattice energy scale is found to be $\epsilon_P = -g^2/2K$, corresponding to the energy of a localized polaron i.e. an electron sitting on a given site associated with the displacement $X_0 = g/K$. The dimensionless ratio polaronic and electronic characteristic energy (D) gives the dimensionless electron phonon coupling

$$\lambda = \frac{g^2}{2KD}. \tag{4.9}$$

The adiabatic parameter

$$\gamma = \frac{2\omega_0}{D} \tag{4.10}$$

quantifies the relative inverse timescales of lattice vibrations (ω_0) and electronic motion (D). When $\gamma \ll 1$, the system is in the adiabatic regime, where phonons evolve much more slowly than the characteristic electronic dynamics. In this limit, for a fixed electron-phonon coupling λ, phonons can be approximated as a static classical field. The electronic problem is then solved for fixed phonon positions, similar to the Born-Oppenheimer approximation, and the results are averaged over phonon configurations.

The Holstein model has been solved using ED-DMFT at zero temperature showing a bipolaronic transition from Fermi liquid state in the spinful case which replaces a polaron crossover in the spinless [87] case. This transition is governed by the parameter λ in the adiabatic regime ($\gamma << 1$) and occurs as a crossover for non-zero temperature in the static phonon case [88].

In the classical limit, the phonon displacement is treated as a randomly distributed classical variable, and its probability distribution is given by the functional integral over the fermionic variables [89] as in [88]:

$$\begin{aligned} P(X) &= \frac{\int \mathbb{D}\hat{c}\mathbb{D}\hat{c}^\dagger e^{-S[X,c]}}{\mathcal{Z}} = \\ &= \frac{e^{-\frac{1}{2}\beta K X^2}\int \mathbb{D}\hat{c}\mathbb{D}\hat{c}^\dagger e^{-S_{el}[X,c]}}{\mathcal{Z}}. \end{aligned} \tag{4.11}$$

The functional integral is on the single site fermonic field $\hat{c}$ (the spin indexes here are omitted for simplicity). The first term $e^{-\frac{1}{2}\beta K X^2}$ is the the contribution of the local bosonic action in the static limi. $S_{el}[X, c]$ is the electronic part of the action

$$S_{el}[X, c] = \int_0^\beta d\tau \int_0^\beta d\tau' c^\dagger(\tau) \left[G_0^{-1}(\tau - \tau') - gX\delta(\tau - \tau')\right] c(\tau') \tag{4.12}$$

The partition function $\mathcal{Z}$ is obtained by integrating e^{-S} over all variables:

$$\mathcal{Z} = \int dX \int \mathbb{D}\hat{c}\mathbb{D}\hat{c}^\dagger e^{-S[X,c,c^\dagger]} \tag{4.13}$$

In this case, X is a classical variable fixed in the integral over the fermionic variables. Since the action is bilinear in the fermionic variables, the integral is a Gaussian integral over Grassmann variables, which can be solved formally. This results in a probability distribution

that is a Gaussian multiplied by a weight due to the electrons

$$P(X) = \frac{e^{-\frac{1}{2}\beta K X^2} W_{el}(X)}{\mathcal{Z}} \tag{4.14}$$

$W_{el}(X)$ is the solution of the Gaussian integral and a functional of G_0. This implies that the probability distribution of the displacements is determined self-consistently and depends on temperature. This is the origin of the annealed disorder. If only the Gaussian probability were considered, the variance of the local potential would be

$$\sigma^2 = g^2 \langle X^2 \rangle = \frac{g^2}{K} K_B T = 2\lambda K_B T \tag{4.15}$$

where λ is the coupling constant. However, the additional weight from $W_{el}(X)$ renormalizes this variance, resulting in a higher effective variance when approaching the polaron transition [88]

$$g^2 \langle X^2 \rangle = 2\lambda^* K_B T = \frac{2\lambda}{1 - c\lambda} K_B T \tag{4.16}$$

where λ^* is a renormalized coupling constant arising from the bubble resummation and $c = \frac{1}{\beta} \sum_n G^2(i\omega_n)$ is the zero frequency electronic bubble.

This is important in electron-phonon systems because the bare electron-phonon coupling constant is renormalized by the environment and the *apparent* divergence of λ^* when $c\lambda = 1$ signal the onset of a bimodal phononic distribution which occurs at the polaronic transition [88]. The constant c can be obtained analytically when $T = 0$ by computing the Matsubara sums as integrals.

Moreover, we know that the variance of the probability distribution for the annealed disorder depends on the temperature and it is intrinsically renormalized by the system itself. In Fig. 4.1, for different values of $\lambda = \frac{g^2}{2}$, the variance of the of the local potential $g^2 \langle X^2 \rangle$ is plotted as a function of $\lambda^* T$, showing a linear relationship between these two quantities with a proportionality constant of 2. This proportionality holds up to $\lambda^* T = 0.1$ where the variance the perturbation theory is not anymore valid.

4.1.3 Quenched and annealed disorder scattering rate within the CPA description

In this section I will show how the scattering rate of an electron in a disordered system can be calculated within the CPA approach. Calculations are performed by using Eq. 4.6 with a gaussian probability distribution with the form 4.7 for the disorder.

The variance W^2 is the fixed variance of the disorder in the case of the quenched disorder.

> The local Green function Eq. 4.6 averaged using gaussian distribution 4.7 can be ex-

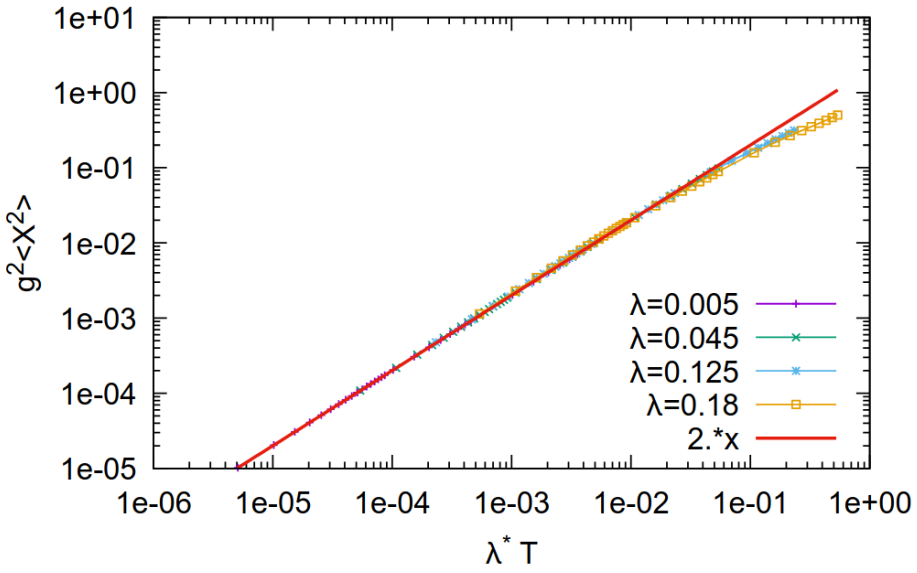


Figure 4.1: Variance of the local potential acting on electrons (gX) as a function of $\lambda^* T$ which is the renormalized electron-phonon constant (λ^*) multiplied by the temperature. The data are obtained with the numerical solution for the uncorrelated model in Eq. 4.8. It is shown for different values of the electron-phonon constant.

pressed as a continued fraction expansion [90, 91]

$$G(\omega) = \cfrac{1}{\omega - \Delta(\omega) - \cfrac{W^2}{\omega - \Delta(\omega) - \cfrac{2W^2}{\omega - \Delta(\omega) - \cfrac{3W^2}{\omega - \Delta(\omega) - \cdots}}}} \tag{4.17}$$

where $\Delta(\omega)$ is the Hybridization function (Eq. 1.34) and from Eq. 4.17 we identify the self-energy as $\Sigma = \omega - \Delta(\omega) - G^{-1}(\omega)$. We want to calculate the scattering rate $\Gamma = -Im\Sigma(0)$, as $\Delta(\omega = 0) = -i\gamma$ is purely imaginary we can express Γ as

$$\Gamma = WS(\gamma/W) \tag{4.18}$$

where $S(x)$ can be expressed as a continued fraction as

$$S(x) = \cfrac{1}{x - \cfrac{2}{x - \cfrac{3}{x - \cfrac{4}{x - \cdots}}}} \tag{4.19}$$

From Eqs. 4.18 and 4.19 we derive the weak disorder limit ($x \to \infty$)

$$\Gamma = W^2/\gamma = W^2(-ImG) \tag{4.20}$$

that is the result of the Born approximation. In the opposite strong disorder limit ($x \to 0$) a

resummation of continued fraction Eq. 4.19 is not straightforward but resorting to Eq. 4.6 it easy to prove that in the large disorder limit using gaussian distribution Eq. 4.7 we get

$$\Gamma = W\sqrt{2/\pi} \tag{4.21}$$

which is now linear in W. Interestingly, when one truncates the fraction 4.17 to any order, the high W linear limit is never recovered since the continued fraction truncation is always an even function of W. This is a signal that the change of dependence is due to a resummation of infinite order diagrams not included in the perturbation theory.

This argument can be extended to annealed disordered systems where, in order to have an extimation of the scattering rate behaviour, the variance W^2 of the probability distribution can be replaced by the variance of the local potential gX acting on electrons, $\lambda^* k_B T$ (Eq. 4.16), in the approximation that this is nearly Gaussian In this case, Eqs. 4.20 and 4.21 are respectively linear in temperature and proportional to the square root of the temperature. The same behaviour transposed to the resistivity is known as resistivity saturation [92]. The result is shown in Fig. 4.2 where the black line represents the analytical calculation for the scattering rate using Gaussian disorder and the points represent Γ obtained by DMFT at several values of electron-phonon interaction.

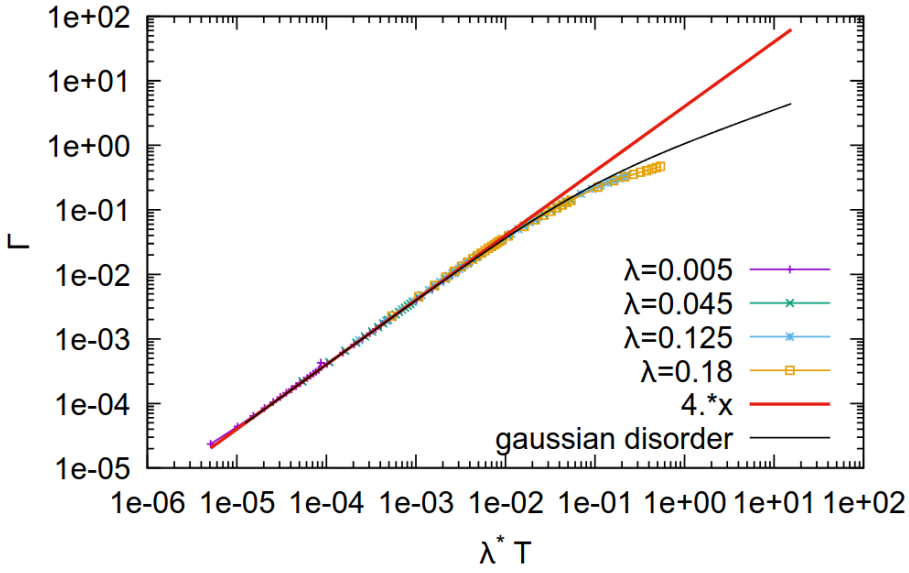


Figure 4.2: Scattering rate calculated for the classical Holstein model as a function of $\lambda^* T$. The black line is obtained using Eq. 4.18 and using the T dependence of local potential variance given in Eq. 4.16. The points represent Γ as from DMFT solution of the Holstein model Eq. 4.8.

4.2 Combining electrons correlation and disorder

Here we combine the electronic correlation with the quenched or annealed disorder. The model in these cases is a Hubbard model with an additional term of the disorder coupled with the density. In the case of quenched disorder, the coupled variable is the random variable ξ_i

$$\hat{H} - \mu\hat{N} = -t \sum_{\langle i,j\rangle\sigma} (\hat{c}^\dagger_{i\sigma}\hat{c}_{j\sigma} + \hat{c}^\dagger_{j\sigma}\hat{c}_{i\sigma}) + U\sum_i \hat{n}_{i\uparrow}\hat{n}_{i\downarrow} - \sum_i (\mu + \xi_i)\hat{n}_i \tag{4.22}$$

From a theoretical perspective, the Hamiltonian admits an exact self-consistent solution in the limit of high spatial dimensions, achieved through a mapping onto an impurity problem [93]. This infinite-dimensional framework has been extensively used to investigate the impact of disorder on strongly correlated systems. Within the Dynamical Mean-Field Theory (DMFT) formalism, the local Green's function can be expressed as a configurational average over disorder realizations, enabling the study of disorder effects. This methodology will be elaborated in subsequent sections. Here, I summarize key findings from prior research. Investigations into the influence of disorder on the Mott transition reveal that increasing disorder pushes the transition to higher interaction strengths and reduces the coexistence region in the temperature range [76]. Additionally, alternative approaches that explore the system above the coherence temperature have shown that stronger disorder induces metallization [72, 73].

In the case of annealed disorder, such as classical phonons, the Hubbard Hamiltonian includes an additional coupling term that accounts for the interaction with phonon displacements, along with the free Hamiltonian describing classical harmonic oscillators

$$\hat{H} - \mu\hat{N} = -t \sum_{\langle i,j\rangle\sigma} (\hat{c}^{\dagger}_{i\sigma}\hat{c}_{j\sigma} + \hat{c}^{\dagger}_{j\sigma}\hat{c}_{i\sigma}) + U \sum_{i} \hat{n}_{i\uparrow}\hat{n}_{i\downarrow} - \sum_{i} (\mu + g\hat{X}_i)\hat{n}_i + \sum_{i} \frac{K}{2}\hat{X}_i^2 \qquad (4.23)$$

This model has been studied, in absence of quenched disorder, within DMFT frameworks using different solvers e.g. ED [87, 94] or more recently by hybridisation expansion continuous time solver [95].

In this work both the quenched disorder case and the classical phonons (annealed disorder) case have been solved by taking the disorder and the correlation on the same foot by employing Dynamical Mean Field Theory (DMFT) to address correlations, utilizing the Iterated Perturbation Theory (IPT) as the impurity solver and combining this approach with the Coherent Potential Approximation (CPA) to investigate disorder. Our approach allows direct investigation of the quantities of interest e.g. Green function and conductivity along the real frequency axis. The algorithm is detailed in Appendix E, but a brief overview of the procedure is provided here. The single-site propagator G is expressed in terms of a local propagator, $G_0(\omega)$, that captures the averaged influence of the environment, along with a self-energy $\Sigma(\omega)$ as:

$$G(\omega) = \frac{1}{G_0^{-1}(\omega) - \Sigma(\omega)}. \qquad (4.24)$$

The site propagator G can be expressed as an average over the disorder variable

$$G(\omega) = \int P(\xi) G_{\xi}(\omega) d\xi = \qquad (4.25)$$

$$= \left\langle \frac{1}{G_0^{-1} + \xi - \Sigma_{\xi,U}(\omega)} \right\rangle_{\xi}, \qquad (4.26)$$

where ξ is the local disorder variable (in the case of annealed disorder it is replaced by $\xi = gX$ where X is the local displacement of the classical phonon) and $\Sigma_{\xi,U}(\omega)$ is the electron-electron self-energy depending on the local variables of the disorder.

To handle this problem practically, two main points are essential. First, for each specific disorder configuration, the impurity problem should be treated as if it were away from half-

filling since each realization of disorder at a single site effectively shifts the local chemical potential. Therefore, we use the n_0-IPT impurity solver rather than the simpler IPT to address this off-half-filling scenario. Second, for the annealed disorder, the treatment of the probability distribution requires particular attention. While quenched disorder has a fixed distribution (as in Eq. 4.7), annealed disorder's distribution is temperature-dependent and requires self-consistent determination (Eq. 4.14). In the next paragraph we will go into more detail about this treatment.

4.2.1 Probability distribution approximation for the Annealed disorder

Similar to the case for the pure Holstein model in the classical limit the path integral formalism in statistical mechanics is an analytical approach for calculating the probability distribution of phonons in the Holstein-Hubbard model. The probability has indeed the same form of Eq. 4.11 but $S_{el}[X, c, c^\dagger]$ also contains the Hubbard interacting part

$$S_{el}[X, c] = \int_0^\beta d\tau \int_0^\beta d\tau' c^\dagger(\tau) \left[G_0^{-1}(\tau - \tau') - gX\delta(\tau - \tau')\right] c(\tau') + S_{int}[c^\dagger, c] \tag{4.27}$$

where

$$S_{int}[c^\dagger, c] = U \int_0^\beta \hat{c}_\uparrow^\dagger(\tau)\hat{c}_\uparrow(\tau)\hat{c}_\downarrow^\dagger(\tau)\hat{c}_\downarrow(\tau) = U \int_0^\beta \hat{n}_\uparrow(\tau)\hat{n}_\downarrow(\tau) \tag{4.28}$$

The probability can thus be written as

$$P(X) = \frac{e^{-\frac{1}{2}\beta K X^2} e^{-\beta F(X)}}{\mathcal{Z}} \tag{4.29}$$

where $F(X)$ is the free energy of the system at a given value of the classical displacement X.

This time, the action is formally not bilinear in the fermionic operators and can't be solved analytically. Moreover, the Free energy can't be calculated within IPT because the free-energy is a functional of G but IPT gives it as a functional of G_0 [96]. Thus, there is no consistent way to derive IPT from a free energy functional.

An alternative approach is to calculate the electronic energy directly instead of the free energy, which can be readily obtained using the Green's function. This approximation involves neglecting the TS term in the expression $F = E_{el} - TS$. However, this method is clearly invalid in the high-temperature regime ($T \gg D$) and in the atomic limit, where $D = 0$ serves as a canonical example for achieving this regime analytically. Nevertheless, as demonstrated in Appendix F, even in the atomic limit, the system's qualitative behavior can still be predicted, albeit with the polaronic transition occurring at twice the temperature compared to the exact result that includes the entropic contribution.

Within this approximation the probability distribution can thus be written as:

$$P(X) \propto e^{-\frac{1}{2}\beta K X^2} e^{-\beta E_{el}(X)} \tag{4.30}$$

where the electronic energy can be evaluated with the expectation value of the electronic Hamiltonian (Eq. 4.23 without the last phononic term) for a fixed set of diplacements $\{X_i\}$

$$E_{el}(\{X_i\}) = \langle H \rangle_{\{X_i\}} \tag{4.31}$$

in the DMFT-CPA approximation it can be obtained with the sum of the energies at fixed X_i

$$E_{el}(\{X_i\}) = \sum_i E_{el}(X_i) \tag{4.32}$$

where the expression of the electronic energy can be derived from Eq. 47 of the review [18]

$$E_{el}(X_i) = T \sum_n \left(\Delta(\omega_n) - gX_i + \frac{1}{2}\Sigma_i(\omega_n, X_i) \right) G_{ii}(\omega_n, X_i) \tag{4.33}$$

and the sum is over Matsubara frequencies. The terms in the expression 4.33 are the impurity quantities calculated at fixed X_i. The first term is the hybridization function, the third term is the impurity self-energy. $G_{ii}(\omega_n, X_i)$ is the impurity Green's function.

This approximation has been shown to be qualitatively reliable away from the polaronic transition, as shown in Appendix F. Additionally, for temperatures much lower than the half-bandwidth ($T \ll D$), the role of entropic contribution is shown to be negligible in the calculation of $P(x)$ (Appendix F).

4.3 Results for the quenched disordered case

We aim to investigate the Fermi liquid regime of resistivity in the previously described disordered and correlated model (Eq. 4.22), which, unlike earlier models [72, 73], is capable of capturing the system's behaviour even in the low-temperature regime. At low temperatures and moderate disorder strengths, the resistivity is proportional to the scattering rate. Therefore, we focus our analysis on the scattering rate, with the understanding that our conclusions will directly extend to the resistivity. However I will introduce the properties of the resistivity and its characteristic behaviour that we want to explore and find a justification for the experimental observations. The numerical analysis will furnish a theoretical explanation of the behaviour involving a reciprocal renormalization of the disorder and the correlation.

4.3.1 Resistivity and scattering rate

The resistivity has been calculated by performing the inverse of the Kubo formula for conductivity 1.26 ($\rho = 1/\sigma$) and is represented in Fig. 4.3 in the strongly correlated metallic phase for the value of $U = 3.0$ near the Metal-Insulator transition (MIT) of the clean system ($U_{c2} = 3.2$ within the IPT) for different values of disorder strength. Three different regimes can be distinguished for the resistivity, corresponding to low, intermediate and large temperatures. The behaviour at intermediate temperatures has been explored in previous works [72, 73], showing a progressive metallization of the system upon increasing the amount of disorder. This originates from the fact that the metal-insulator transition is shifted to higher interaction values of U as W increases [76], i.e. randomness and local interactions compete. The large temperature regime is instead a bad metallic regime (where the resistivity exceeds the Mott-Ioffel-Regel limit) dominated by incoherent scattering and, being less sensitive to the locus of the phase transition, it is also less sensitive to disorder.

Our focus here is on the low-temperature regime, that becomes accessible taking advantage

of the fully quantum nature of the IPT, that correctly reproduces the $W = 0$ Fermi liquid regime. Contrary to the intermediate and high-temperature regimes, here a normal behaviour is recovered, where a finite residual resistivity develops at $T = 0$ and the resistivity is an increasing function of disorder strength, as expected for a disordered metal.

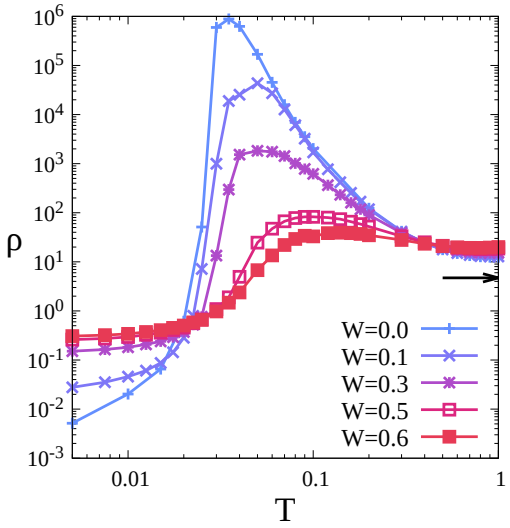


Figure 4.3: Resistivity varying W. $U = 3.0$ is close to the MIT at $W = 0$ ($U_c = 3.2$). The black arrow represents the Motte-Ioffe-Regel limit obtained with Eq. 4.36 when $\Gamma \simeq D$.

When the temperature is smaller than the effective low energy bandwidth scale set by the spectral function ($T << D^*$), in the Kubo equation 1.26 (with $\bar{\sigma} = 1$) the derivative of the Fermi function can be safely approximated by a delta function in $\omega = 0$ giving

$$\sigma \simeq 2\pi \int d\epsilon \mathcal{N}_\phi(\epsilon) A^2(\epsilon, \omega = 0) \tag{4.34}$$

$A(\epsilon, \omega)$ is the spectral function coming from the DMFT self-consistency and can be approximated as

$$A(\epsilon, \omega) = -\frac{1}{\pi} Im \frac{1}{\omega + i\delta - \Sigma - \epsilon} \tag{4.35}$$

where $\Sigma = \Sigma_1 + i\Sigma_2$, which at $\omega = 0$ has the zero real part and $\Sigma_2(\omega = 0) = -\Gamma$ where Γ is the scattering rate [32]. $A(\epsilon, \omega = 0)$ is then a Lorentzian function in ϵ. For small $\Gamma << D$ and using the current vertex density for the semicircular density of states [97] $\mathcal{N}_\phi(\epsilon) = z + \frac{2}{3}\left((z^2 - 1) \cdot \sqrt{z - 1} \cdot \sqrt{z + 1} - z^3\right)$ ($z = \epsilon + \mu - \Sigma(\epsilon) + \delta$), the integral gives

$$\sigma \simeq \frac{\mathcal{N}(\epsilon = 0)}{\Gamma} \tag{4.36}$$

At low temperatures and for weak to moderate disorder strengths [78] the resistivity is therefore proportional to the scattering rate at the Fermi energy and the scattering rate has the following temperature behaviour

$$\Gamma = \Gamma_0 + bT^2. \tag{4.37}$$

This can be checked by plotting Γ as a function of T^2 as shown in Fig. 4.4.

While the presence of Γ_0 is due to finite disorder and the bT^2 term in Eq. 4.37 is reminiscent of the Fermi liquid regime, the actual dependence of these parameters on disorder

and interactions is not at all trivial. At all values of U, the intercept (Γ_0) markedly increases with the disorder strength, while the slope (b) is much less affected by disorder at low temperatures. Meanwhile, the competition between randomness and interactions, that causes a disorder-induced metallization at large temperatures, manifests here by the decreasing of Γ_0 upon increasing U. In the following Section we quantitatively analyze and explain these observations.

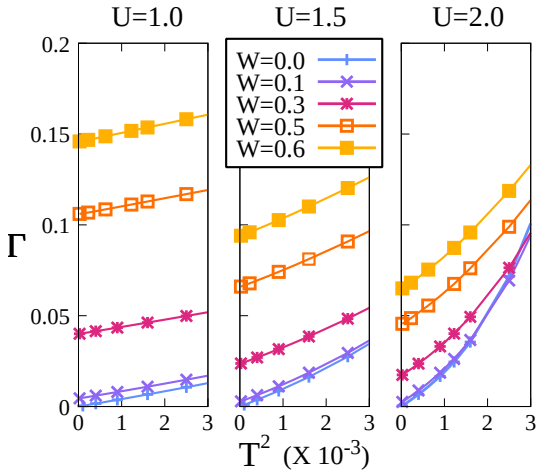


Figure 4.4: Scattering rate as a function of T^2. The intercept varies but the coefficient for T^2 remains constant over the different disorders. Like Fig. 3 in [17]

4.3.2 Renormalization of the disorder by the interaction and of the interaction by the disorder

The combined effect of disorder and interactions at low temperatures allows us to investigate whether Matthiessen's rule is satisfied. In its simplest form, this implies that the total scattering rate should be the sum of the pure interaction scattering rate $\Gamma(U, W = 0)$ (that can be obtained from DMFT calculations in clean systems) and the disorder scattering rate $\Gamma(U = 0, W)$ (that can be obtained by CPA calculations in the absence of interactions).

In Fig. 4.5 a tentative Matthiessen's rule interpretation of the low temperature scattering rate is shown in the case of strongly correlated metal $U = 2.0$. As the residual scattering rate Γ_0 of the disordered system in the absence of interaction (back arrow) largerly overestimate the actual value (orange curve, x) a straightforward application of Matthiessen's rule largerly overestimate the scattering rate up to large temperatures. At the same time, a fit of the DMFT data using Eq. 4.37 gives a very good agreement and indeed at low temperatures, Matthiessen's rule can be restored by addressing new significance to the two terms appearing in 4.37. This suggests that the residual scattering rate and the coeffcient b are renormalized but the descriptive function remains the same.

Specifically, the low temperature residual scattering can be interpreted as that of a non interacting disordered system with renormalized interaction-dependent disorder strength $\bar{W}(U)$

$$\Gamma_0 = \Gamma_0(\bar{W}(U)). \tag{4.38}$$

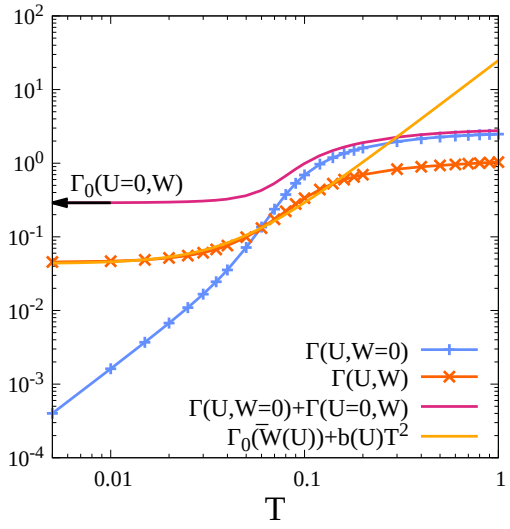


Figure 4.5: Scattering rate function for $U = 2.0$ and $W = 0.5$ calculated within the IPT+CPA method (red) compared to: the bare interaction scattering rate (dark green), the scattering rate calculated with the bare Matthiessen's rule (green) calculated with the sum between the scattering rates of the two bare interactions $\Gamma(U, W = 0) + \Gamma(U = 0, W)$, and the scattering rate calculated with the sum of the intercept with the renormalized disorder and the interaction part given by the nominal interaction (pink). The arrow indicates the value for the intercept of the scattering rate in the non-interacting disordered case.

The coefficient b in 4.37 can be interpreted as that of a weakly renormalized interacting sistem with $\bar{U}(W)$.

$$b = b(\bar{U}(W) \tag{4.39}$$

Let us consider the origin of the two terms appearing in Eq. 4.37.

The Γ_0 term in Eq. 4.38 is obtained as a residual scattering rate for a purely disordered system in which the interaction renormalizes the disorder strength $\Gamma_0(\bar{W}(U)) = \Gamma_0(U = 0, \bar{W})$. This can be observed in Fig. 4.6 a), where Γ_0 is expressed as a function of the disorder intensity. The behaviour is quadratic for small W, as one expects from perturbation theory. When increasing W one expects a linear behaviour, which is visible at $U = 0.0$ and $U = 0.5$. The same quantity normalized with W^2 as a function of U is shown in Fig. 4.6 b). Here, the discrepancy at low U shows that the behaviour is not quadratic in W in these cases. Overall, the Γ_0/W^2 decreases with U, i.e., the interaction renormalises the disorder effect.

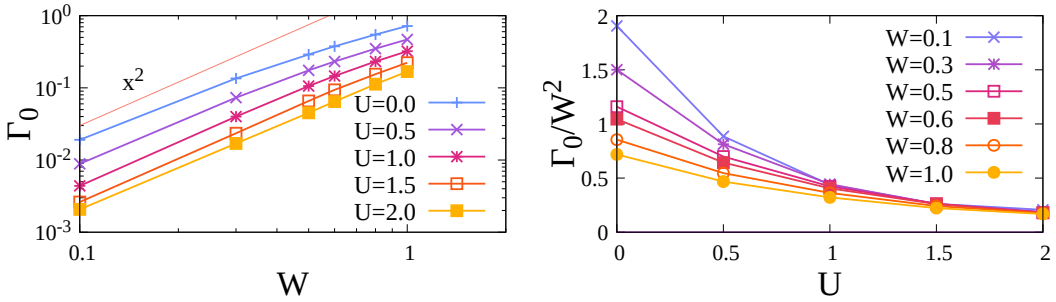


Figure 4.6: a) The intercept of the scattering rate as a function of the disorder intensity. It scales quadratically. b) Γ_0 as a function of the interaction strength U. The intercept is then renormalized by the interaction.

On the other side the coefficient of T^2 in Fig. 4.7 is normalized with U^2 which is the perturbative behaviour. In this view, when U is large enough the coefficient b is dependent only on U^2, and is not modified by the disorder.

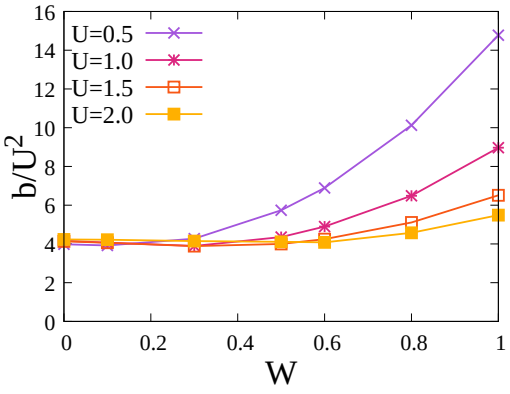


Figure 4.7: The T^2 coefficient of the scattering rate. It remains constant for large U with varying the disorder. This means that the disorder does not normalize too much the coefficient given by the Fermi liquid regime.

At this point is possible to define the renormalized $\bar{W}$ and $\bar{U}$.

The value of $\bar{W}$ can be obtained by considering that the interacting system behaves like a non-interacting system with a different disorder strength. The expression for the non-interacting $\Gamma_0(W)$ can be obtained analitically within CPA (Section 4.1.1) and inverted to get the effective $\bar{W}$ from the known Γ_0 in the presence of interaction.

The T^2 term in Eq. 4.39 embodies instead the effect of the disorder on the interaction. We assume, as before, that at a defined U and $W \neq 0$, $b(\bar{U}(W)) = b(\bar{U}, W = 0)$.

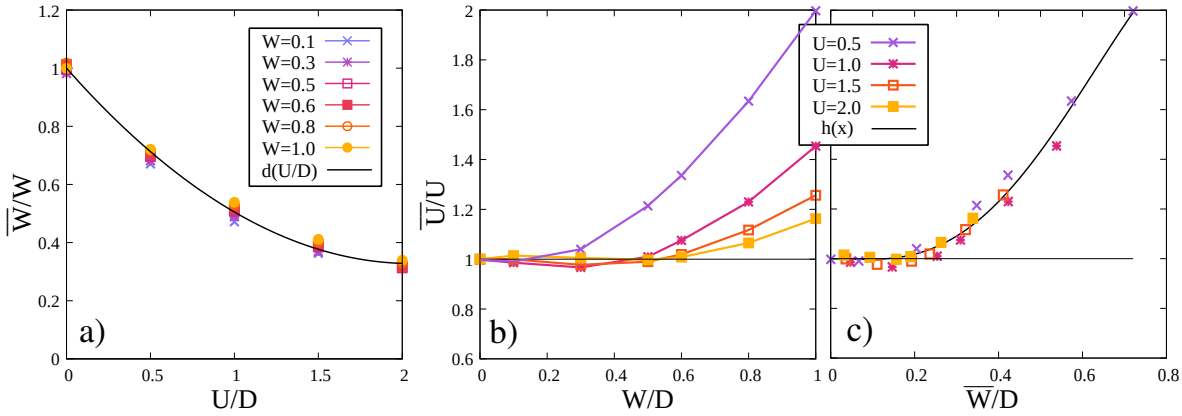


Figure 4.8: a) The renormalized disorder parameter $\bar{W}/W$ as a function of U for different values of disorder W, black line is a fitting curve $d(x) = 1 + d_1 x + d_2 x^2$. b) Effective interaction $\bar{U}/U$ as a function of the disorder. c) Effective interaction parameter $\bar{U}/U$ as a function of the renormalized disorder parameter $\bar{W}/D$, black line is a fitting curve $h(x) = 1 + h_2 x^2 + h_3 x^3 + h_4 x^4$.

Fig. 4.8 shows the main result of this work showing both the renormalized disorder strength $\bar{W}/W$ as a function of the interaction (a) and the renormalized interaction $\bar{U}/U$ as a function of the disorder strength (b). In this analysis, different disorder strengths approximately scale onto the same universal curve as a function of the interaction only. The

renormalized disorder is lower than the nominal one and decreases, increasing the interaction strength, leading the system to a more metallic one.

The effects are instead more complex regarding the quadratic temperature coefficient that embodies electron-electron collisions. On one hand, by screening the effective disorder potential, large values of U appear to stabilize Fermi liquid behavior, pinning the coefficient b to its disorder-free value. On the other hand, this protection against disorder breaks down when the latter becomes too strong: beyond a certain threshold, disorder starts to cooperate with interactions causing an increase of the inelastic scattering rate, which can be interpreted as an increase of the effective interaction strength.

Further analysis can be conducted by considering the mutually renormalized system, where the effective disorder environment renormalized also renormalizes the interaction. The result is shown in Fig. 4.8 c), where the renormalized interaction is a function of the strength of the renormalized disorder. The interaction remains effectively non-renormalized in the range of small disorder up to $\bar{W} \simeq 0.3W$. However, as the renormalized disorder increases, the effective interaction is enhanced.

A physical explanation for the renormalization of the disorder by the interaction can be attributed to the anti-correlation between disorder and interaction. The interacting electrons move in a random effective disorder η of variance $\langle \eta^2 \rangle < W^2$ due to the anticorrelation between the self-energy fluctuations and the disorder itself.

The anti-correlation between the disorder and the interaction can be the origin of the renormalization of the disorder by the interaction. Given the local Green's function

$$\langle \hat{G} \rangle_\xi = \left\langle \frac{1}{G_0^{-1} + \xi - \Sigma(\xi)} \right\rangle_\xi \tag{4.40}$$

the self-energy can be splitted as $\Sigma(\xi) = \Sigma_U(0) + \Delta\Sigma(\xi)$ where $\Sigma_U(0)$ is the $\xi = 0$ value of $\Sigma(\xi)$ due to the presence of interactions. The propagator can thus be rewritten as

$$\langle \hat{G} \rangle_\xi = \left\langle \frac{1}{G_U^{-1} + \xi - \Delta\Sigma(\xi)} \right\rangle_\xi \tag{4.41}$$

where $G_U = (G_0^{-1} - \Sigma_U(0))^{-1}$. A zero mean effective disorder can be defined as $\eta = \xi - Re\Delta\Sigma(\xi)$.

In the limit of weak disorder, one can use the linear approximation for the real part of Σ

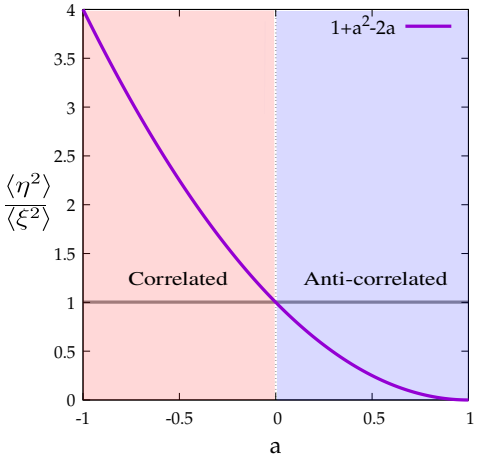
$$Re\Delta\Sigma(\xi) = \frac{\partial Re\Delta\Sigma(\xi)}{\partial \xi}|_{\xi=0}\xi = a\xi \tag{4.42}$$

then the variance of the effective disorder will be

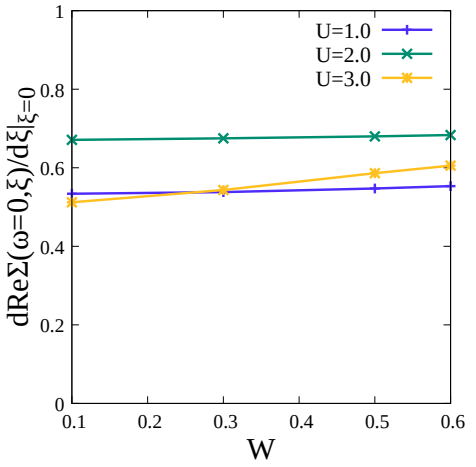
$$\langle \eta^2 \rangle = \langle \xi^2 \rangle \left[1 + a^2 - 2a\right] \tag{4.43}$$

the function $\langle \eta^2 \rangle / \langle \xi^2 \rangle$ is shown in Fig. 4.9a and when $a < 1$ it means that disorder and interaction are correlated, when $a > 1$ they are anticorrelated. In our data

(Fig. 4.9b), $a > 0$ which means anticorrelation, and being the disorder small ($a < 1$), this leads directly to the fact that the effective disorder strength in the presence of interactions is lower than the nominal one $\langle \eta^2 \rangle < \langle \xi^2 \rangle$.



(a) Effective correlation function over the nominal one as a function of $a = \frac{\partial \mathrm{Re}\Delta\Sigma(\xi)}{\partial \xi}|_{\xi=0}$



(b) $a = \frac{\partial \mathrm{Re}\Delta\Sigma(\xi)}{\partial \xi}|_{\xi=0}$ for different values of U and W at $T = 0.01$

Figure 4.9: Comparison of the two analyses: (a) Effective correlation function, and (b) Dependence of a on U and W.

Comparison with experiments

We compared our theoretical findings qualitatively with the experimental data in [17] to validate our results. Briefly, the experiment is performed in the material $\kappa-(ET)_2Cu[N(CN)_2]Cl$ which belongs to the family of layered organic conductors with half-filled bands. These materials experiment first-order transition from a Mott insulator to a Fermi liquid increasing the pressure and, in this phase, when decreasing the temperature, they are superconductive. Irradiation induces disorder in the chemical bonds in the anion layers of these materials and the irradiation time (t_{irr}) is proportional to the disorder. In Fig. 3 (a), (b), (c) and (d) of the paper [17], it is shown that the resistivity has the following general expression $R = R_0 + AT^2$.

Fig. 4.10 shows our theoretical results that can be compared to the Fig. 3 (e) of the experiment. The coefficient b for the quadratic behaviour (A in the experiment) is constant over the different disorder intensities (orange line). The intercept ρ_0 (R_0 in the experiment) strongly depends on the disorder (black line).

4.4 Results for the annealed disorder

The technique and results obtained for quenched disorder can be extended to annealed disorder (or classical phonons) through some theoretical considerations. We here present our preliminary results of a study of the temperature dependence of the scattering rate obtained by the Hamiltonian Eq. 4.23.

Analyzing the scattering rate reveals a contribution proportional to temperature, originating from the classical phonons. This contribution is renormalized by interactions, and the

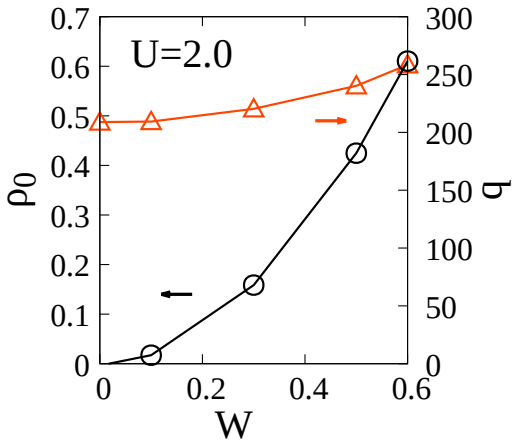


Figure 4.10: Intercept of the resistivity (ρ_0) and coefficient of T^2 (b) as a function of the disorder for $U = 2.0$.

nature of this renormalization can be studied within the same framework used for quenched disorder, after accounting for the variance of the disorder distribution.

This work is still in progress, but here the theoretical foundations and some preliminary results that support the theory are presented. The preliminary results analyze the quantities as a function of the coupling g between the electron density n_i and the displacement X_i in the i-site. However it is related to λ (Eq. 4.9).

4.4.1 Scattering rate

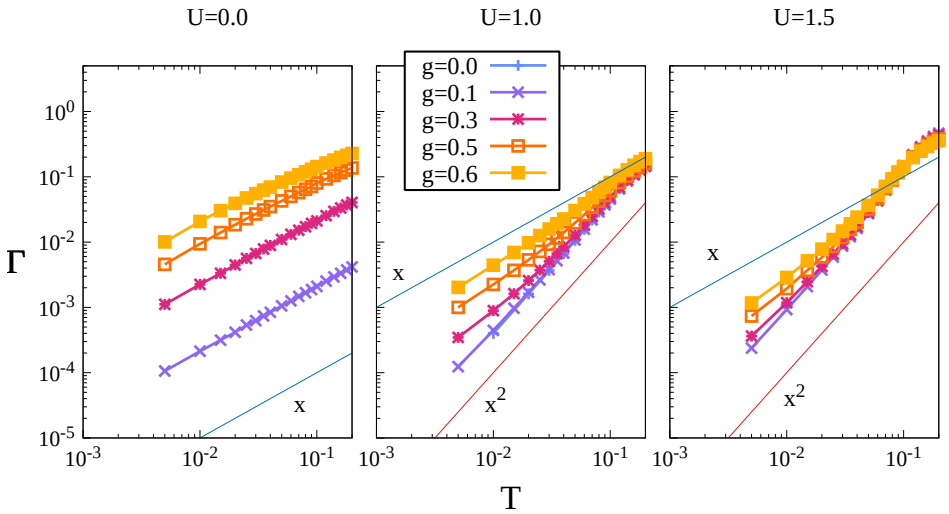


Figure 4.11: Scattering rate at low temperatures for a correlated Bethe lattice with electron–classical phonon coupling, shown as a function of temperature for different values of the interaction U and electron-phonon coupling $g = 2KD\sqrt{\lambda}$ and $K = D = 1$.

Figure 4.11 shows the low-temperature scattering rate as a function of T on a logarithmic scale. This representation highlights the temperature dependence of the scattering rate,

which—unlike the quenched disorder case (Eq. 4.37)—follows the form

$$\Gamma = cT + bT^2 \tag{4.44}$$

where the linear term (with coefficient c) represents the phononic contribution, while the quadratic term reflects the perturbative effect of electron correlations.

In the absence of correlations ($U = 0$), the scattering rate is linear in T, with the slope increasing as the electron-phonon coupling g increases (Eq. 4.16). At higher temperatures, outside the perturbative regime, a change in slope becomes evident due to vertex corrections, leading to a $\sqrt{T}$ dependence [88]. As the interaction strength increases ($U = 1.0$, $U = 1.5$), the quadratic temperature dependence at lower T becomes more pronounced, reflecting the influence of electron correlations.

4.4.2 Preliminary results with interaction

The analysis of the two coefficients in Eq. 4.44 was conducted similarly to the case of the quenched disorder by extrapolating data from a fit of the scattering rate at low temperatures. In Fig. 4.12, the coefficient of the linear term, c, is shown as a function of the electron-phonon coupling g (left panel) and the interaction strength U (right panel). c approximately scales quadratically with electron phonon coupling c. From Fig. 4.12 the linear in T coefficient of the scattering rate is strongly reduced by the interaction U.

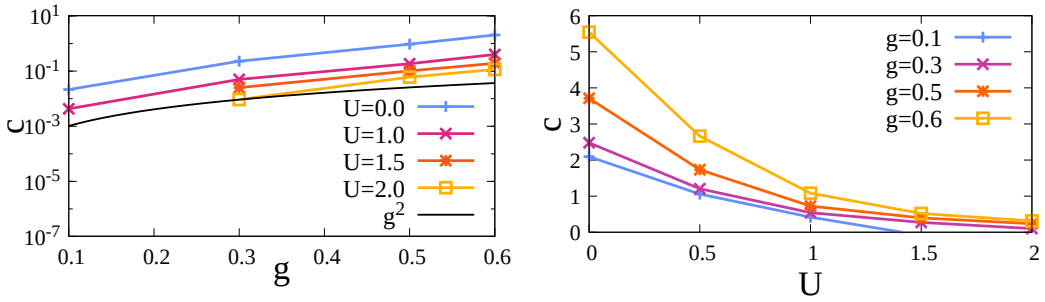


Figure 4.12: a) The coefficient of the linear in T term c as a function of $g = 2KD\sqrt{\lambda}$ and $K = D = 1$. b) c as a function of the interaction strength U.

On the other hand, we analyzed the coefficient of the quadratic term, normalized by U^2, which corresponds to the perturbative behavior, as a function of the coupling g (Fig. 4.13). The result is consistent with the case of quenched disorder, as the coefficient is not much affected by the strength of the electron-phonon coupling, when U is large, $b/U^2 \approx 4$ which is the value obtained from the perturbation theory (See Appendix C and value of a_0 in Eq. C.12).

The main purpose for the future development of this work is to calculate the mutually renormalized quantities. In this case one can define the two parts in Eq. 4.44 with renormalized quantities $cT(\bar{g})$ and $b(\bar{U})$. However, the analysis is more complex than in the case of quenched disorder, because the crossover temperature between the linear and quadratic terms is given by $T^* = c/b$ (see Fig. 4.14). In scenarios with small g and large U, the crossover temperature T^* becomes very small, making the linear behavior difficult to detect.

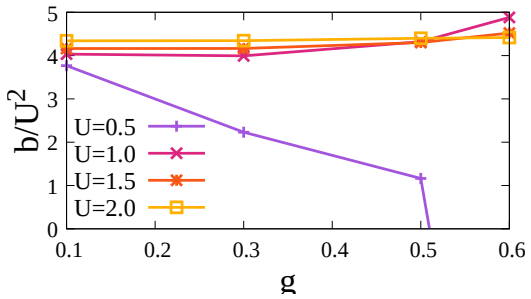


Figure 4.13: The T^2 coefficient of the scattering rate as a function of $g = 2KD\sqrt{\lambda}$ and $K = D = 1$. It remains constant for large U with varying the coupling. This means that the phonons don't normalize too much the coefficient given by the Fermi liquid regime. When $U = 0.5$ the linear phase is predominant and the fit of the quadratic term becomes difficult.

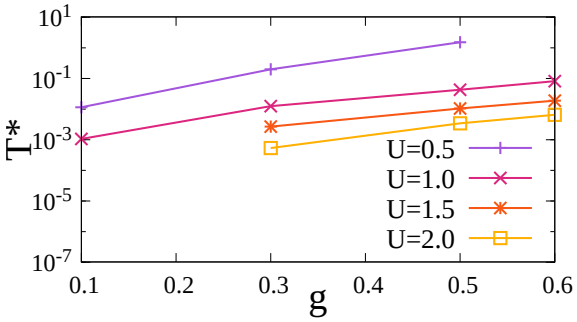


Figure 4.14: Crossover temperature as a function of g for different values of the interaction U. It increases of orders of magnitude when increasing g and/or decreasing U.

CONCLUSIONS

The focus of this thesis was to provide a theoretical description of specific strongly correlated systems in the presence of other types of interactions. In particular, the study aimed to understand how electron correlation competes with various interactions or intrinsic properties of the system. The theoretical framework employed was Dynamical Mean Field Theory (DMFT), which averages properties over space and is exact in infinite dimensions. However, DMFT provides a reliable approximation for three-dimensional systems, which form the core focus of this thesis. The specific DMFT flavor used in this thesis was IPT a real-frequencies impurity solver which allows to obtain directly the spectral functions and transport properties.

The first class of systems analyzed was nodal semimetals. In these systems, an intriguing competition emerges between electronic correlation and band dispersion. The band dispersion of nodal semimetals is characterized by linear behavior around specific band crossings, a property dictated by the symmetry of the system. This inherent symmetry competes with electronic correlations, effectively pushing the onset of the Mott transition to higher interaction strengths. This observation supports the idea that symmetry protects the system against local perturbations.

In the semimetallic phase, before reaching the Mott transition, several notable properties can be described. One key feature is the high conductivity observed in these materials. The linear dispersion around the nodes at the Fermi level results in a vanishing density of states at the Fermi level, with a quadratic behavior around it. This unique density of states is responsible for the unusually high exponents in the temperature dependence of resistivity. While the DMFT prediction becomes inaccurate precisely at the nodal point due to the local approximation [56], the theory accurately describes the behavior of exponents away from the node. Specifically, crossovers from higher to lower exponents were observed when deviations from linearity in the bands were included. This crossover could explain the experimental behavior of resistivity in certain directions.

Further investigation into nodal semimetals revealed that they exhibit Kondo screening at sufficiently low temperatures. Using the Anderson impurity model to solve the self-consistent lattice model for nodal semimetals demonstrated the emergence of the Kondo effect. This model represents a specific case where the impurity couples to a bath through a hybridization function that is infinite at the Fermi level and finite elsewhere within the bandwidth of the bath.

The second class of systems studied involved strongly correlated systems where disorder plays a significant role. Two types of disorder were considered: quenched and annealed disorder. Quenched disorder has a fixed probability distribution unaffected by interacting electrons and is representative of systems with lattice impurities as occurs in correlated materials subjected to irradiation. Our approach revealed that interaction renormalizes the disorder distribution, corroborating experimental observations in irradiated correlated κ-organics. Specifically, electronic correlations reduce the effective disorder in the system. Conversely, disorder has minimal impact on correlated properties unless its strength fraction of system's half-bandwidth.

Similar results were observed, in a preliminar study presented here, for systems coupled to phonons in the classical phonon approximation. In this case, the renormalized quantity is the variance local potential induced by electron phonon interaction. Although this work is ongoing, it has broader applicability to systems where electron-phonon interaction is comparable in strength to electronic correlations, such as vanadates where recent measurements seem to suggest that electron-phonon interaction play important role in transport properties [98].

The study of mutual renormalization between disorder interaction and correlations can be performed in the Mott insulator and away from half-filling to explore a mechanism that can be relevant in the cuprates [99–101]. The method can also be extended to more complex, multi-orbital [102] and Hund materials [103]. Also, a more detailed analysis of the experiments performed in moderately correlated perovskite metal such as $SrVO_3$ [104] is needed even if the qualitative behaviour of the incercept ρ_0 can be explained by the mechanism put forward in the present work.

BIBLIOGRAPHY

[1] M. Imada, A. Fujimori, and Y. Tokura, Rev. Mod. Phys. **70**, 1039 (1998).

[2] L. Degiorgi, Rev. Mod. Phys. **71**, 687 (1999).

[3] G. R. Stewart, Rev. Mod. Phys. **73**, 797 (2001).

[4] H. v. Löhneysen, A. Rosch, M. Vojta, and P. Wölfle, Rev. Mod. Phys. **79**, 1015 (2007).

[5] P. Gegenwart, Q. Si, and F. Steglich, Nature Physics **4** (2008), 10.1038/nphys892.

[6] N. P. Armitage, P. Fournier, and R. L. Greene, Rev. Mod. Phys. **82**, 2421 (2010).

[7] N. Kumar, Y. Sun, N. Xu, K. Manna, M. Yao, V. Süss, I. Leermakers, O. Young, T. Förster, M. Schmidt, H. Borrmann, B. Yan, U. M. Zeitler, Shi, C. Felser, and C. Shekar, Nature Communications **8**, 1642 (2017).

[8] N. Kumar, Y. Sun, M. Nicklas, S. J. Watzman, O. Toung, I. Leermakers, J. Hornung, J. Klotz, J. Gooth, K. Manna, V. Süb, S. N. Giun, T. Förster, M. Schmidt, L. Muechler, B. Yan, P. Werner, W. Schnelle, U. Zeitler, J. Wosnitza, S. S. P. Parkin, C. Felser, and C. Shekar, Nature Communications **10**, 2475 (2019).

[9] T. Liang, Q. Gibson, M. N. Ali, M. Liu, R. J. Cava, and N. P. Ong, Nature Materials **14**, 280 (2015).

[10] O. Vafek and A. Vishwanath, Annual Review of Condensed Matter Physics **5**, 83 (2014), https://doi.org/10.1146/annurev-conmatphys-031113-133841 .

[11] R. A. Nistor, M. A. Kuroda, A. A. Maarouf, and G. J. Martyna, Phys. Rev. B **86**, 041409 (2012).

[12] B. A. Bernevig, Z.-D. Song, N. Regnault, and B. Lian, Phys. Rev. B **103**, 205411 (2021).

[13] G. Rai, L. Crippa, D. Călugăru, H. Hu, F. Paoletti, L. de' Medici, A. Georges, B. A. Bernevig, R. Valentí, G. Sangiovanni, and T. Wehling, Phys. Rev. X **14**, 031045 (2024).

[14] A. S. Shankar, D. O. Oriekhov, A. K. Mitchell, and L. Fritz, Phys. Rev. B **107**, 245102 (2023).

[15] Y. Chang, J. Yi, A.-K. Wu, F. B. Kugler, E. Y. Andrei, D. Vanderbilt, G. Kotliar, and J. H. Pixley, Phys. Rev. Lett. **133**, 126503 (2024).

[16] P. A. Lee, N. Nagaosa, and X.-G. Wen, Rev. Mod. Phys. **78**, 17 (2006).

[17] M. Urai, T. Furukawa, Y. Seki, K. Miyagawa, T. Sasaki, H. Taniguchi, and K. Kanoda, Phys. Rev. B **99**, 245139 (2019).

[18] A. Georges, G. Kotliar, W. Krauth, and M. J. Rozenberg, Reviews of Modern Physics **68**, 13 (1996).

[19] A. Burkov, Annual Review of Condensed Matter Physics **9**, 359 (2018), https://doi.org/10.1146/annurev-conmatphys-033117-054129 .

[20] P. Hosur, S. A. Parameswaran, and A. Vishwanath, Physical Review Letters **108**, 046602 (2012).

[21] P. Hosur and X. Qi, Comptes Rendus Physique **14**, 857 (2013), topological insulators / Isolants topologiques.

[22] J. Kondo, Progress of Theoretical Physics **32**, 37 (1964).

[23] P. Coleman, *Introduction to Many-Body Physics* (Cambridge University Press, 2015).

[24] L. Fritz and M. Vojta, Phys. Rev. B **70**, 214427 (2004).

[25] N. Wagner, S. Ciuchi, A. Toschi, B. Trauzettel, and G. Sangiovanni, Phys. Rev. Lett. **126**, 206601 (2021).

[26] A. Poli, N. Wagner, M. Fischer, A. Toschi, G. Sangiovanni, and S. Ciuchi, Phys. Rev. B **109**, 045118 (2024).

[27] M. Fischer, A. Poli, L. Crippa, S. Ciuchi, M. Vojta, A. Toschi, and G. Sangiovanni, "Fragility of local moments against hybridization with singular baths," (2025), arXiv:2503.14326 [cond-mat.str-el] .

[28] A. Poli, S. Fratini, J. Coulter, A. J. Millis, and S. Ciuchi, "Stabilization of fermi-liquid behavior by interactions in disordered metals," (2025), arXiv:2502.17250 [cond-mat.str-el] .

[29] N. W. Ashcroft and N. D. Mermin, *Solid State Physics* (Holt-Saunders, 1976).

[30] W. G. Baber and N. F. Mott, Proceedings of the Royal Society of London **158**, 383 (1937).

[31] "Landau fermi-liquid theory and low temperature properties of normal liquid 3he," in *Landau Fermi-Liquid Theory* (John Wiley and Sons, Ltd, 1991) Chap. 1, pp. 1–121, https://onlinelibrary.wiley.com/doi/pdf/10.1002/9783527617159.ch1 .

[32] G. D. Mahan, *Many-Particle Physics*, Physics of Solids and Liquids (Springer New York, NY, 2000).

[33] A. Khurana, Phys. Rev. Lett. **64**, 1990 (1990).

[34] M. C. Gutzwiller, Phys. Rev. Lett. **10**, 159 (1963).

[35] J. Hubbard, Proc. R. Soc. Lond. **A 276**, 238–257 (1963).

[36] J. Kanamori, Progress of Theoretical Physics **30**, 275 (1963), https://academic.oup.com/ptp/article-pdf/30/3/275/5278869/30-3-275.pdf .

[37] G. H. Wannier, Phys. Rev. **52**, 191 (1937).

[38] F. H. L. Essler, H. Frahm, F. Göhmann, A. Klümper, and V. E. Korepin, *The One-Dimensional Hubbard Model* (Cambridge University Press, 2005).

[39] A. Georges and G. Kotliar, Phys. Rev. B **45**, 6479 (1992).

[40] W. Metzner and D. Vollhardt, Phys. Rev. Lett. **62**, 324 (1989).

[41] K. Yamada, Progress of Theoretical Physics **53**, 970 (1975), https://academic.oup.com/ptp/article-pdf/53/4/970/5428364/53-4-970.pdf .

[42] K. Yosida and K. Yamada, Progress of Theoretical Physics Supplement **46**, 244 (1970), https://academic.oup.com/ptps/article-pdf/doi/10.1143/PTPS.46.244/5302531/46-244.pdf .

[43] X. Y. Zhang, M. J. Rozenberg, and G. Kotliar, Phys. Rev. Lett. **70**, 1666 (1993).

[44] H. Kajueter and G. Kotliar, Physical Review Letters **77**, 131 (1996).

[45] H. Kajueter, G. Kotliar, and G. Moeller, Physical Review B **53**, 16214 (1996).

[46] M. Potthoff, T. Wegner, and W. Nolting, Phys. Rev. B **55**, 16132 (1997).

[47] T. Wegner, M. Potthoff, and W. Nolting, Phys. Rev. B **57**, 6211 (1998).

[48] E. Muller-Hartmann, Z. Phys. B - Condensed Matter **74**, 507 (1989).

[49] A. Martin-Rodero, F. Flores, M. Baldo, and R. Pucci, Solid State Communications **44**, 911 (1982).

[50] L.-F. m. c. Arsenault, P. Sémon, and A.-M. S. Tremblay, Phys. Rev. B **86**, 085133 (2012).

[51] H. Terletska, J. Vučičević, D. Tanasković, and V. Dobrosavljević, Phys. Rev. Lett **46**, 26401 (2011).

[52] A. A. Burkov, M. D. Hook, and L. Balents, Physical Review B **84**, 235126 (2011).

[53] P. Nozieres and D. Pines, *Theory Of Quantum Liquids*, Advanced Books Classics (Avalon Publishing, 1999).

[54] B. Q. Lv, N. Xu, H. M. Weng, J. Z. Ma, P. Richard, X. C. Huang, L. X. Zhao, G. F. Chen, C. E. Matt, F. Bisti, and et al., Nature Physics **11**, 724–727 (2015).

[55] A. Georges and G. Kotliar, Physical Review B **45**, 6479 (1992).

[56] A. Mu, Z. Sun, and A. J. Millis, Phys. Rev. B **106**, 085142 (2022).

[57] P. Hansmann, A. Toschi, G. Sangiovanni, T. Saha-Dasgupta, S. Lupi, M. Marsi, and K. Held, physica status solidi (b) **250**, 1251 (2013), https://onlinelibrary.wiley.com/doi/pdf/10.1002/pssb.201248476 .

[58] M. Kargarian, M. Randeria, and Y.-M. Lu, Proceedings of the National Academy of Sciences **113**, 8648 (2016), https://www.pnas.org/doi/pdf/10.1073/pnas.1524787113 .

[59] B. Irsigler, T. Grass, J. H. Zheng, M. Barbier, and W. Hofstetter, Phys. Rev. B **103**, 125132 (2021).

[60] M. Wallerberger, A. Hausoel, P. Gunacker, A. Kowalski, N. Parragh, F. Goth, K. Held, and G. Sangiovanni, Computer Physics Communications **235**, 388 (2019).

[61] P. Chalupa, T. Schäfer, M. Reitner, D. Springer, S. Andergassen, and A. Toschi, Phys. Rev. Lett. **126**, 056403 (2021).

[62] T. B. Mazitov and A. A. Katanin, Phys. Rev. B **105**, L081111 (2022).

[63] J. Vučičević, S. Predin, and M. Ferrero, Phys. Rev. B **107**, 155140 (2023).

[64] P. E. C. Ashby and J. P. Carbotte, Phys. Rev. B **89**, 245121 (2014).

[65] N. Pakhira and R. H. McKenzie, Physical Review B **91**, 075124 (2015).

[66] K. Andres, J. E. Graebner, and H. R. Ott, Phys. Rev. Lett. **35**, 1779 (1975).

[67] P. Coleman, "Heavy fermions: Electrons at the edge of magnetism," in *Handbook of Magnetism and Advanced Magnetic Materials* (John Wiley Sons, Ltd, 2007) https://onlinelibrary.wiley.com/doi/pdf/10.1002/9780470022184.hmm105 .

[68] A. C. Hewson, *The Kondo Problem to Heavy Fermions*, Cambridge Studies in Magnetism (Cambridge University Press, 1993).

[69] K. G. Wilson, Rev. Mod. Phys. **47**, 773 (1975).

[70] P. Nozières, The European Physical Journal B - Condensed Matter and Complex Systems **6**, 447 (1998).

[71] T. Sasaki, H. Oizumi, N. Yoneyama, N. Kobayashi, and N. Toyota, Journal of the Physical Society of Japan **76**, 123701 (2007), https://doi.org/10.1143/JPSJ.76.123701 .

[72] M. c. v. M. Radonjić, D. Tanasković, V. Dobrosavljević, and K. Haule, Phys. Rev. B **81**, 075118 (2010).

[73] S. Ciuchi and S. Fratini, Phys. Rev. B **108**, 235173 (2023).

[74] J. G. Analytis, A. Ardavan, S. J. Blundell, R. L. Owen, E. F. Garman, C. Jeynes, and B. J. Powell, Phys. Rev. Lett. **96**, 177002 (2006).

[75] P. Limelette, P. Wzietek, S. Florens, A. Georges, T. A. Costi, C. Pasquier, D. Jérome, C. Mézière, and P. Batail, Phys. Rev. Lett. **91**, 016401 (2003).

[76] M. C. O. Aguiar, V. Dobrosavljević, E. Abrahams, and G. Kotliar, Phys. Rev. B **71**, 205115 (2005).

[77] D. Tanasković, V. Dobrosavljević, E. Abrahams, and G. Kotliar, Phys. Rev. Lett. **91**, 066603 (2003).

[78] S. Ciuchi, D. Di Sante, V. Dobrosavljević, and S. Fratini, npj Quantum Materials **3**, 44 (2018).

[79] P. W. Anderson, Phys. Rev. **109**, 1492 (1958).

[80] P. Soven, Phys. Rev. **156**, 809 (1967).

[81] D. W. Taylor, Phys. Rev. **156**, 1017 (1967).

[82] R. J. Elliott, J. A. Krumhansl, and P. L. Leath, Rev. Mod. Phys. **46**, 465 (1974).

[83] R. Vlaming and D. Vollhardt, Phys. Rev. B **45**, 4637 (1992).

[84] P. Erdös and R. C. Herndon, Adv. Phys. **31**, 65 (1982).

[85] T. Holstein, Annals of Physics **8**, 325 (1959).

[86] T. Holstein, Annals of Physics **8**, 343 (1959).

[87] M. Capone and S. Ciuchi, Phys. Rev. Lett. **91**, 186405 (2003).

[88] A. J. Millis, R. Mueller, and B. I. Shraiman, Phys. Rev. B **54**, 5389 (1996).

[89] A. Altland and B. D. Simons, *Condensed Matter Field Theory*, 2nd ed. (Cambridge University Press, 2010).

[90] M. Abramowitz and I. A. Stegun, *Handbook of Mathematical Functions with Formulas, Graphs, and Mathematical Tables.* (Dover Publications, 1983).

[91] A. Cuyt, V. B. Petersen, B. Verdonk, H. Waadeland, and W. B. Jones, *Handbook of Continued Fractions for Special Functions* (Springer Dordrecht, 2008).

[92] A. J. Millis, J. Hu, and S. D. Sarma, Phys. Rev. Lett. **82**, 2354 (1999).

[93] V. Dobrosavljević and G. Kotliar, Phys. Rev. Lett. **71**, 3218 (1993).

[94] G. Sangiovanni, M. Capone, C. Castellani, and M. Grilli, Phys. Rev. Lett. **94**, 026401 (2005).

[95] P. Werner and A. J. Millis, Phys. Rev. Lett. **99**, 146404 (2007).

[96] E. G. C. P. van Loon, Phys. Rev. B **105**, 245104 (2022).

[97] A. Chattopadhyay, A. J. Millis, and S. Das Sarma, Phys. Rev. B **61**, 10738 (2000).

[98] M. Mirjolet, F. Rivadulla, P. Marsik, V. Borisov, R. Valentí, and J. Fontcuberta, Advanced Science **8**, 2004207 (2021), https://advanced.onlinelibrary.wiley.com/doi/pdf/10.1002/advs.202004207 .

[99] F. Rullier-Albenque, H. Alloul, and R. Tourbot, Phys. Rev. Lett. **87**, 157001 (2001).

[100] F. Rullier-Albenque, H. Alloul, and R. Tourbot, Phys. Rev. Lett. **91**, 047001 (2003).

[101] F. Rullier-Albenque, R. Tourbot, H. Alloul, P. Lejay, D. Colson, and A. Forget, Phys. Rev. Lett. **96**, 067002 (2006).

[102] A. Wang, L. Wu, Q. Du, M. Naamneh, W. H. Brito, A. M. Abeykoon, W. R. Pudelko, J. Jandke, Y. Liu, N. C. Plumb, G. Kotliar, V. Dobrosavljevic, M. Radovic, Y. Zhu, and C. Petrovic, Nano Letters **22**, 6900 (2022), pMID: 35976289, https://doi.org/10.1021/acs.nanolett.2c01282 .

[103] D. J. Abramovitch, J. Mravlje, J.-J. Zhou, A. Georges, and M. Bernardi, Phys. Rev. Lett. **133**, 186501 (2024).

[104] M. Mirjolet, F. Rivadulla, P. Marsik, V. Borisov, R. Valentí, and J. Fontcuberta, Advanced Science **8**, 2004207 (2021), https://advanced.onlinelibrary.wiley.com/doi/pdf/10.1002/advs.202004207 .

[105] D. Di Sante and S. Ciuchi, Phys. Rev. B **90**, 075111 (2014).

[106] E. Gull, A. J. Millis, A. I. Lichtenstein, A. N. Rubtsov, M. Troyer, and P. Werner, Rev. Mod. Phys. **83**, 349 (2011).

[107] X. Wang, H. T. Dang, and A. J. Millis, Phys. Rev. B **84**, 073104 (2011).

APPENDIX A

QUASIPARTICLE DAMPING AT WEAK COUPLING

From perturbation theory calculations [25] the small energy and temperature behaviour of the imaginary part of the self-energy has a polynomial dependence

$$Im\left[\Sigma(\omega)\right] = -8\pi^9 T^8 U^2 \left(\frac{1}{2\pi^2 v_F^3}\right)^3 P_8(\omega/T) \tag{A.1}$$

with

$$P_8(x) = a_0 + a_2 x^2 + a_4 x^4 + a_8 x^8 \tag{A.2}$$

$$a_0 = \frac{3\pi^8}{128} \tag{A.3}$$

$$a_2 = \frac{31\pi^6}{504 \cdot 2!} \tag{A.4}$$

$$a_4 = \frac{7\pi^4}{40 \cdot 4!} \tag{A.5}$$

$$a_8 = \frac{1}{8!} \tag{A.6}$$

and according to our definition of the density of states in Eqs. 2.29, 2.31, $v_F^3 = 1/(2\pi^2 c) = \frac{1}{2\pi^2}(2\Lambda^2(D-\Lambda) + \frac{2}{3}\Lambda^3)$.

In Fig. A.1 is shown the temperature evolution of the quasi-particle damping $\Gamma = -\mathrm{Im}[\Sigma(\omega = 0)]$ normalized with U^2, for different values of the interaction strength ($U = U/D$) and for different values of the cutoff (Λ/D). Temperature exponent ranges from a pure T^8 characteristic of nodal semimetal to T^2 being the characteristic exponent of the Fermi liquid phase. As far as $\Lambda/D < 1$, non-linear band effects extend to low energy and the exponent decreases from 8 to 2. Increasing U/D, for $\Lambda/D < 1$, leads to a more evident decrease of the exponent from the second-order perturbation theory result. A clear deviation from perturbation theory is shown for the smallest value of Λ/D and the largest value of U.

Employing a suitable scaling of the Γ and T in order to compare systems with the same zero energy Fermi velocity (see Appendix B) we get the rescaled curves shown in Fig. A.2. We identify a clear crossover from the semimetal liquid to the Fermi liquid behaviour of the quasi-particle damping which occurs when the $T \sim 0.1 v_F$. For the smallest $\Lambda/D = 0.05$ the

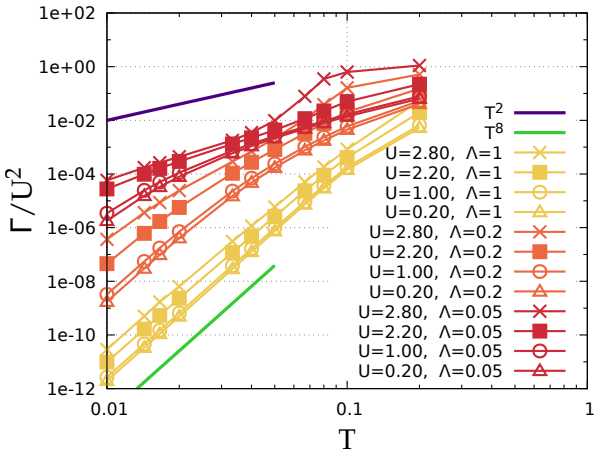


Figure A.1: The quasi-particle damping at half-filling normalized with U^2 as a function of the temperature ($T = T/D$) for $\Lambda = \Lambda/D = 1.0,\ 0.2,\ 0.05$ and several values of $U = U/D$ from the metallic side approaching the MIT.

range of T is too narrow to observe the semimetal liquid perturbative behaviour which we expect at very low temperatures.

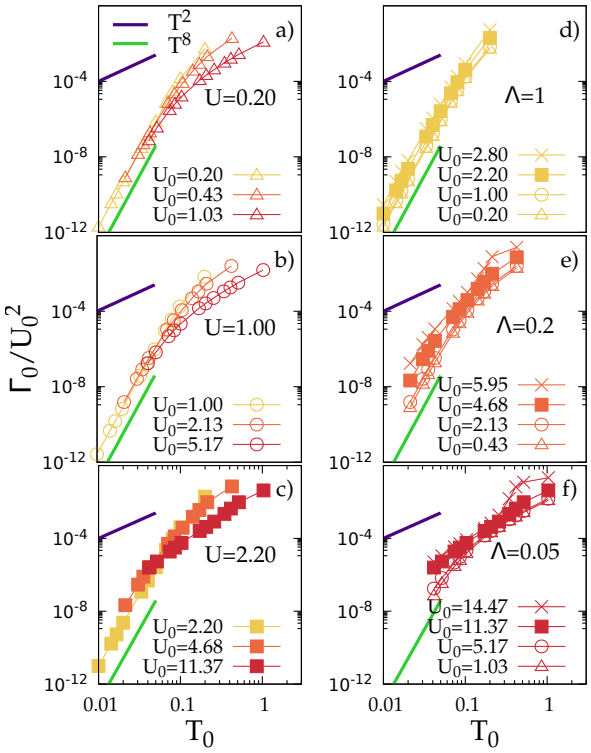


Figure A.2: The quasi-particle damping at half-filling normalized with U_0^2 at fixed $U = U/D$ and $\Lambda = \Lambda/D$ as a function of the temperature (T/D_0) and scaled to obtain a comparison between quantities with the same bare Fermi velocity. The subscript 0 indicates that the quantity in units D_0 [see Appendix B]. The colour code is the same as in Fig. A.1

APPENDIX B

SCALING AT WEAK COUPLING

In Fig. B.1 we show the total non-interacting DOS for $\Lambda/D = 1$ and for $\Lambda/D < 1$. In order to compare systems with the same *bare* Fermi velocity (curvature of the DOS around zero energy) a rescaling of the DOS (inset of Fig. B.1) is required. The rescaling affects both temperatures and the interaction strengths for $\Lambda/D < 1$.

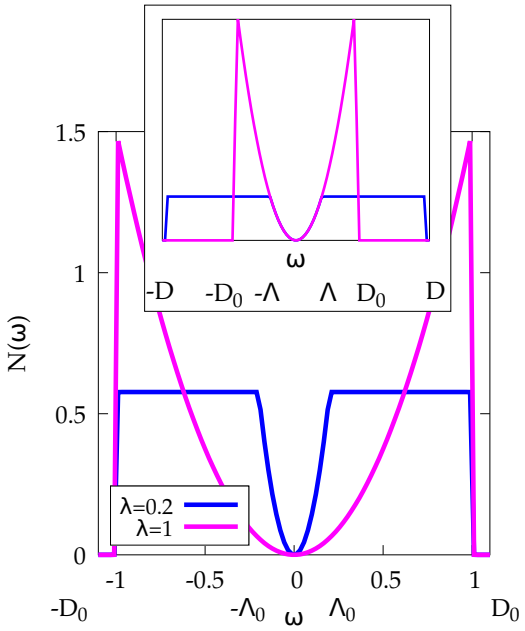


Figure B.1: Free particle DOS used in the IPT codes. Notice different curvature around $\omega = 0$ which imply different bare Fermi velocity. In the inset: Scaled free particle DOS which shows the same bare Fermi velocity.

Firstly, we fix the half-bandwidth of the model with $\Lambda/D = 1$ to a value D_0. The normalisation constant entering the DOS in Eq. 2.29 as $\Lambda = D_0$ can be expressed as

$$c = \frac{3}{2D_0^3} \tag{B.1}$$

Then, we can define a scaling factor such that

$$c_0 S^3(\lambda) = \frac{3}{2D_0^3} \tag{B.2}$$

where the subscript 0 stands for the constants describing the DOS model with half-bandwidth D_0. The constant $\lambda = \Lambda/D = \Lambda_0/D_0$ is independent from the rescaling. Recalling the formula for the normalization constant in 2.31, $c_0 = 1/\left[(\frac{2}{3}\lambda^3 + 2\lambda^2(1-\lambda))D_0^3\right]$ and therefore

$$S(\lambda) = (\lambda^3 + 3\lambda^2(1-\lambda))^{1/3}. \tag{B.3}$$

In order to keep D_0 constant we should rescale the half-bandwidth as

$$D = \frac{D_0}{S(\lambda)} \tag{B.4}$$

but also the temperature and the interaction consistently

$$\frac{T}{D_0} = \frac{T}{D}\frac{D}{D_0} = \frac{T}{S(\lambda)} > \frac{T}{D} \tag{B.5}$$

$$\frac{U}{D_0} = \frac{U}{D}\frac{D}{D_0} = \frac{U}{S(\lambda)} > \frac{U}{D}. \tag{B.6}$$

APPENDIX C

SECOND-ORDER PERTURBATION THEORY CALCULATIONS FOR A FLAT DOS

The imaginary part of the self-energy for a generic DOS, calculated with the second-order perturbation theory, is

$$\begin{aligned} Im\left[\Sigma(\omega)\right] = -\pi U^2 \int d\epsilon_k d\epsilon_{k'} d\epsilon_{k''} \mathcal{N}(\epsilon_{\vec{k}}) \mathcal{N}(\epsilon_{\vec{k'}}) \mathcal{N}(\epsilon_{\vec{k''}}) \cdot \\ \cdot \left[f(\epsilon_{\vec{k'}})(1 - f(\epsilon_{\vec{k''}}))(1 - f(\epsilon_{\vec{k}})) + \right. \\ \left. + (1 - f(\epsilon_{\vec{k'}})) f(\epsilon_{\vec{k''}}) f(\epsilon_{\vec{k}}) \right] \cdot \\ \cdot \delta(\omega + \epsilon_{\vec{k}} - \epsilon_{\vec{k'}} + \epsilon_{\vec{k''}}) \end{aligned} \tag{C.1}$$

as calculated in [25].

In [25] was calculated the specific imaginary part of the self-energy for a quadratic dispersed DOS. Here, the calculation for the flat dispersed DOS is shown as it is relevant for our $\Lambda/D = 0$ case.

We consider a flat band with large bandwidth D which gives

$$Im\left[\Sigma(\omega)\right] = -\frac{\pi U^2}{(2D)^3} \left(\xi(\omega) + \xi(-\omega)\right) \tag{C.2}$$

with

$$\begin{aligned} \xi(\omega) &= \int d\epsilon_k d\epsilon_{k'} d\epsilon_{k''} \delta(\omega - (\epsilon_k + \epsilon_{k'} + \epsilon_{k''})) f(\epsilon_{\vec{k}}) f(\epsilon_{\vec{k'}}) f(\epsilon_{\vec{k''}}) \\ &= \int \frac{d\alpha}{2\pi} e^{i\alpha\omega} A^3(\alpha) \end{aligned} \tag{C.3}$$

$A(\alpha)$ is given by

$$A(\alpha) = \int d\epsilon \; e^{-i\tilde{\alpha}\epsilon} f(\epsilon) \tag{C.4}$$

where $\tilde{\alpha} = \alpha + i\delta$. A complex integration is then performed.

When $\alpha \geq 0$ we close the integration path in the lower complex half-plane

$$\begin{aligned} A(\alpha) &= i2\pi T \sum_{m=0}^{\infty} e^{i\tilde{\alpha}(-i\pi T(2m+1))} \\ &= i\pi T \frac{1}{sinh(\tilde{\alpha}\pi T)} \end{aligned} \tag{C.5}$$

if $\alpha < 0$ we obtain the same result closing the path in the upper half plane

$$A^3(\alpha) = -i(\pi T)^3 \frac{1}{sinh^3(\tilde{\alpha}\pi T)}. \tag{C.6}$$

We expand around the poles $\tilde{\alpha} = \frac{in}{T}$ with $n \in \mathbb{N}$

$$\begin{aligned} A_n^3(\alpha) &= -i(\pi T)^3 \left[\frac{1}{(\pi T)^3(\tilde{\alpha} - \frac{in}{T})^3} - \frac{1}{2(\pi T)(\tilde{\alpha} - \frac{in}{T})} \right] \\ &= -i(-1)^n \left[\frac{1}{(\tilde{\alpha} - \frac{in}{T})^3} - \frac{(\pi T)^2}{2(\tilde{\alpha} - \frac{in}{T})} \right] \end{aligned} \tag{C.7}$$

which gives

$$\xi(\omega) = \int \frac{d\alpha}{2\pi} e^{i\alpha\omega} A^3(\alpha) = \oint \frac{dz}{2\pi} e^{iz\omega} A^3(z) =$$

$$= i(-i) \sum_{n=1}^{\infty} (-1)^n e^{-\frac{n\omega}{T}} \left[-\frac{\omega^2}{2!} - \frac{(\pi T)^2}{2} \right] =$$

$$= \frac{1}{1 + e^{\frac{\omega}{T}}} \left[\frac{\omega^2}{2} + \frac{(\pi T)^2}{2} \right] \tag{C.8}$$

We get for the imaginary part of the self-energy

$$\begin{aligned} Im\left[\Sigma(\omega)\right] &= -\frac{\pi U^2}{(2D)^3} \left(\xi(\omega) + \xi(-\omega)\right) = \\ &= -\frac{\pi U^2}{(2D)^3} \frac{1}{2} \left[\omega^2 + (\pi T)^2\right] \end{aligned} \tag{C.9}$$

The real part of the self-energy is obtained using the Kramers-Kroening relations using a large frequency cutoff L as

$$Re\left[\Sigma(\omega)\right] = -\frac{1}{\pi} P \int_{-L}^{L} d\epsilon \frac{Im\left[\Sigma(\epsilon)\right]}{\omega - \epsilon}. \tag{C.10}$$

We use the Eq. C.9

$$-Im\left[\Sigma(\omega)\right] = \left[a_2\omega^2 + a_0 T^2\right] \tag{C.11}$$

where

$$a_0 = \frac{U^2\pi^3}{2(2D)^3}$$
$$a_2 = \frac{U^2\pi}{2(2D)^3} \tag{C.12}$$

For $\omega << L$ we get

$$\frac{Re\left[\Sigma(\omega)\right]}{D} \simeq -\frac{U^2}{D^2}\left[\frac{\pi^2 L}{8D^2} - \frac{T^2}{8D^2 L}\right]\omega \tag{C.13}$$

which shows a linear dependence in ω.

APPENDIX D

KONDO DIMER CALCULATIONS

D.1 Eigenvalues and eigenvectors of the Kondo dimer

D.1.1 0-particles and 4-particles

The eigenvalues of the states $|0_1, 0_d>$ and $|2_1, 2_d>$ are 0. The contribution to the partition function is $\mathcal{Z}_1 = \mathcal{Z}_4 = 1$

D.1.2 1-particle and 3-particles

The basis on which we calculate quantities are $\{|1_\uparrow, 0>, |0, d_\uparrow>, |1_\downarrow, 0>, |0, d_\downarrow>\}$ for 1-particle and $\{|1_\uparrow, 2>, |2, d_\uparrow>, |1_\downarrow, 2>, |2, d_\downarrow>\}$ for 3-particles.

The Hamiltonian for 1(3)-particles is

$$H = \begin{pmatrix} \epsilon_F & (-)V & 0 & 0 \\ (-)V & \epsilon_d - h & 0 & 0 \\ 0 & 0 & \epsilon_F - h & (-)V \\ 0 & 0 & (-)V & \epsilon_d + h \end{pmatrix} = \tag{D.1}$$

$$= \begin{pmatrix} \frac{\epsilon_F + \epsilon_d - h}{2}\mathbb{1} \pm V\sigma_x + \frac{\epsilon_F - \epsilon_d + h}{2}\sigma_z & 0 \\ 0 & \frac{\epsilon_F + \epsilon_d + h}{2}\mathbb{1} \pm V\sigma_x + \frac{\epsilon_F - \epsilon_d - h}{2}\sigma_z \end{pmatrix} \tag{D.2}$$

The eigenvalues are the same for the two systems and are:

$$E_{1,2} = \frac{\epsilon_F + \epsilon_d - h}{2} \pm \sqrt{\left[\frac{\epsilon_F - \epsilon_d + h}{2}\right]^2 + V^2} = n_0 \pm \sqrt{n_3^2 + n_1^2} = n_0 \pm |\vec{n}| \tag{D.3}$$

$$E_{3,4} = \frac{\epsilon_F + \epsilon_d + h}{2} \pm \sqrt{\left[\frac{\epsilon_F - \epsilon_d - h}{2}\right]^2 + V^2} = n_0' \pm \sqrt{n_3'^2 + n_1'^2} = n_0' \pm |\vec{n'}| \tag{D.4}$$

D.1.3 2-particles

The basis in which we can consider the Hamiltonian is the same exposed by Max, $\{|T_2>, |T_3>, |T_1>, |S>, |D>\}, |D_d>\}$.

$$|T_2>=|1_\uparrow, d_\uparrow> \tag{D.5}$$
$$|T_3>=|1_\downarrow, d_\downarrow> \tag{D.6}$$
$$|T_1>=\frac{1}{\sqrt{2}}\left(|1_\uparrow, d_\downarrow>+|1_\downarrow, d_\uparrow>\right) \tag{D.7}$$
$$|S>=\frac{1}{\sqrt{2}}\left(|1_\uparrow, d_\downarrow>-|1_\downarrow, d_\uparrow>\right) \tag{D.8}$$
$$|D>\}=|2_1, 0_d> \tag{D.9}$$
$$|D_d>=|0_1, 2_d> \tag{D.10}$$

$|T_2>$ and $|T_3>$ are the magnetic states of the triplet, $|T_1>$ is the symmetric state of the triplet, $|S>$ is the singlet, and $|D>$ is the double occupied state in the bath. In this basis, with the addition of the magnetic field, the Hamiltonian is

$$H=\begin{pmatrix} \epsilon_F+\epsilon_d-h & 0 & 0 & 0 & 0 & 0 \\ 0 & \epsilon_F+\epsilon_d+h & 0 & 0 & 0 & 0 \\ 0 & 0 & \epsilon_F+\epsilon_d & h & 0 & 0 \\ 0 & 0 & h & \epsilon_F+\epsilon_d & \sqrt{2}V & \sqrt{2}V \\ 0 & 0 & 0 & \sqrt{2}V & 2\epsilon_F & 0 \\ 0 & 0 & 0 & \sqrt{2}V & 0 & U+2\epsilon_F \end{pmatrix} \tag{D.11}$$

The eigenvalues of the triplet submatrix correspondent to the eigenvectors $|T_2>$ and $|T_3>$ are $E_{t2,t3}=\epsilon_F+\epsilon_d\mp h$. The other 4×4 matrix can be studied with the perturbation theory. Let's consider first the unperturbed Hamiltonian when $h=0$. In this case, the energy of the state $|T_1>$ is $E_{t1}=\epsilon_F+\epsilon_d$.

Another simplification can be done considering that at half-filling $\epsilon_d=-\frac{U}{2}$ and $\epsilon_F=0$. The 3×3 Hamiltonian is then

$$H=\begin{pmatrix} -\frac{U}{2} & \sqrt{2}V & \sqrt{2}V \\ \sqrt{2}V & 0 & 0 \\ \sqrt{2}V & 0 & 0 \end{pmatrix} \tag{D.12}$$

it can be written in a better way with a change of basis $\{|S>, \frac{1}{\sqrt{2}}(|D_d>+|D_1>), \frac{1}{\sqrt{2}}(|D_d>-|D_1>)\}=\{|S>, |D_+>, |D_->\}$ and the Hamiltonian simplifies in this way

$$H=\begin{pmatrix} -\frac{U}{2} & 2V & 0 \\ 2V & 0 & 0 \\ 0 & 0 & 0 \end{pmatrix} \tag{D.13}$$

First of all, the eigenvalue correspondent to the $|D_->$ state is $E_{D_-}=0$. The other 2×2

block can be written with the Pauli matrices

$$\vec{b}\cdot\vec{\sigma} = -\frac{U}{4}\mathbb{1} + 2V\sigma_x - \frac{U}{4}\sigma_z$$

. The eigenvalues are then $E_\pm = -\frac{U}{4} \pm \sqrt{4V^2 + \frac{U^2}{16}}$. With correspondent eigenvectors

$$|v_+ >= \frac{1}{N_b}\begin{pmatrix} b_3 + |\vec{b}| \\ b_1 \end{pmatrix} = v_+^{(S)}|S> + v_+^{(D)}|D_+> \tag{D.14}$$

$$|v_- >= \frac{1}{N_b}\begin{pmatrix} -b_1 \\ b_3 + |\vec{b}| \end{pmatrix} = v_-^{(S)}|S> + v_-^{(D)}|D_+> \tag{D.15}$$

where $N_b = \sqrt{2|\vec{b}|(b_3 + |\vec{b}|)}$

Within perturbation theory, the $E_{2,3}$ eigenvalues are linear in h. The other ones are quadratic in h but the eigenvectors are linear. To calculate the eigenvectors we use the perturbation theory with the perturbative potential

$$hV = h\begin{pmatrix} 0 & 1 & 0 & 0 \\ 1 & 0 & 0 & 0 \\ 0 & 0 & 0 & 0 \\ 0 & 0 & 0 & 0 \end{pmatrix} \tag{D.16}$$

in the eigenstates $\{|T_1>, |v_+>, |v_->, |D_->\}$. The perturbed states are defined

$$|n>^{(1)} = |n>^{(0)} + h\sum_{k\neq n}\frac{^{(0)}<k|V|n>^{(0)}}{E_n - E_k}|k>^{(0)} \tag{D.17}$$

so the perturbed states here are

$$|T_1>^{(1)} = \frac{1}{N_1}\left(|T_1>^{(0)} + h\frac{v_+^{(S)}}{E_{t1} - E_+}|v_+>^{(0)} + h\frac{v_-^{(S)}}{E_{t1} - E_-}|v_->^{(0)}\right) = \tag{D.18}$$

$$= \frac{1}{N_1}\left(|T_1>^{(0)} + ht_+|v_+>^{(0)} + ht_-|v_->^{(0)}\right) \tag{D.19}$$

$$|v_->^{(1)} = \frac{1}{N_-}\left(|v_->^{(0)} + h\frac{v_-^{(S)}}{E_- - E_{t1}}|T_1>^{(0)}\right) = \tag{D.20}$$

$$= \frac{1}{N_-}\left(|v_->^{(0)} + hv_{-t}|T_1>^{(0)}\right) \tag{D.21}$$

$$|v_+>^{(1)} = \frac{1}{N_+}\left(|v_+>^{(0)} + h\frac{v_+^{(S)}}{E_+ - E_{t1}}|T_1>^{(0)}\right) = \tag{D.22}$$

$$= \frac{1}{N_+}\left(|v_+>^{(0)} + hv_{+t}|T_1>^{(0)}\right) \tag{D.23}$$

$$|D_->^{(1)} = |D_->^{(0)} \tag{D.24}$$

where N_1, N_- and N_+ are the normalization factors.

$$N_1 = \sqrt{1 + (ht_+)^2 + (ht_-)^2} \tag{D.25}$$
$$N_- = \sqrt{1 + (hv_{-t})^2} \tag{D.26}$$
$$N_+ = \sqrt{1 + (hv_{+t})^2} \tag{D.27}$$

D.2 Magnetization and susceptibility in the canonical ensemble

The magnetization in the canonical ensemble is defined as

$$< \sigma_z >= \frac{Tre^{-\beta\hat{H}}\hat{\sigma}_z}{Tre^{-\beta\hat{H}}} = m_N \tag{D.28}$$

and the spin susceptibility by its derivative

$$\chi^s_{loc} = \frac{\partial m_N}{\partial h} \tag{D.29}$$

D.2.1 0-particles and 4-particles

These states are non-magnetic. Then, the magnetization is 0.

D.2.2 1-particle and 3-particles

To calculate the magnetization we can use the properties of Pauli matrices. Indeed, the Hamiltonian D.2 is made by two blocks of 2×2 matrices. The first block is written

$$\begin{aligned} e^{-\beta\hat{H}} &= e^{-\beta n_0 \mathbb{1}} e^{-\beta\hat{n}\cdot\vec{\sigma}} = \\ &= \mathbb{1} e^{-\beta n_0}(cosh(\beta|\vec{n}|)\mathbb{1} - sinh(\beta|\vec{n}|)\hat{n}\cdot\vec{\sigma}) \end{aligned}$$

In the same basis,

$$\sigma_z = \begin{pmatrix} 0 & 0 & 0 & 0 \\ 0 & 1 & 0 & 0 \\ 0 & 0 & 0 & 0 \\ 0 & 0 & 0 & -1 \end{pmatrix} = \begin{pmatrix} \frac{1}{2}\mathbb{1} - \frac{1}{2}\sigma_z & 0 \\ 0 & -\frac{1}{2}\mathbb{1} + \frac{1}{2}\sigma_z \end{pmatrix} \tag{D.30}$$

For the first block the magnetization is thus

$$< \sigma_z > = \frac{Tre^{-\beta n_0}(cosh(\beta|\vec{n}|)\mathbb{1} - sinh(\beta|\vec{n}|)\hat{n}\cdot\vec{\sigma})(\frac{1}{2}\mathbb{1} - \frac{1}{2}\sigma_z)}{\mathcal{Z}_{1,(3)}} = \tag{D.31}$$
$$= e^{-\beta n_0}\frac{cosh(\beta|\vec{n}|) + sinh(\beta|\vec{n}|)\cdot\hat{n}_3}{\mathcal{Z}_{1,(3)}} \tag{D.32}$$

where

$$\hat{n} = \frac{1}{|\vec{n}|}(\pm V, 0, \frac{\epsilon_F - \epsilon_d + h}{2}) \tag{D.33}$$

and

$$\mathcal{Z}_{1,(3)} = e^{-\beta E_1} + e^{-\beta E_2} \tag{D.34}$$

The second block of D.2 is similar to the first but with the opposite sign of h. I will identify it with a $'$ and

$$\mathcal{Z}'_{1,(3)} = e^{-\beta E_3} + e^{-\beta E_4} \tag{D.35}$$

The total magnetization for $1,(3)$-particles is

$$m_{1,(3)} = \frac{1}{\mathcal{Z}_{1,(3)} + \mathcal{Z}'_{1,(3)}} \left[e^{-\beta n_0}(cosh(\beta|\vec{n}|) + sinh(\beta|\vec{n}|) \cdot \hat{n}_3) - e^{-\beta n'_0}(cosh(\beta|\vec{n'}|) + sinh(\beta|\vec{n'}|) \cdot \hat{n}'_3) \right] \tag{D.36}$$

D.2.3 2-particles

To calculate the magnetization here one should have the average of σ_z over the Hamiltonian perturbed states.

$$< T_2|\sigma_z|T_2 >= 1 \tag{D.37}$$

$$< T_3|\sigma_z|T_3 >= -1 \tag{D.38}$$

$$^{(1)} < T_1|\sigma_z|T_1 >^{(1)} = -\frac{2h}{N_1^2}\left[t_- v_-^{(S)} + t_+ v_+^{(S)}\right] \tag{D.39}$$

$$^{(1)} < v_-|\sigma_z|v_- >^{(1)} = -\frac{2h}{N_-^2}\left[v_{-t} v_-^{(S)}\right] \tag{D.40}$$

$$^{(1)} < v_+|\sigma_z|v_+ >^{(1)} = -\frac{2h}{N_+^2}\left[v_{+t} v_+^{(S)}\right] \tag{D.41}$$

$$^{(1)} < D_-|\sigma_z|D_- >^{(1)} = 0 \tag{D.42}$$

The magnetization is

$$m_2 = \frac{1}{\mathcal{Z}_2}\left[e^{-\beta E_{t2}} - e^{-\beta E_{t3}} - e^{-\beta E_{t1}} \frac{2h}{N_1^2}(t_- v_-^{(S)} + t_+ v_+^{(S)}) - e^{-\beta E_-} \frac{2h}{N_-^2}(v_{-t} v_-^{(S)}) - e^{-\beta E_+} \frac{2h}{N_+^2}(v_{+t} v_+^{(S)}) \right] \tag{D.43}$$

with

$$\mathcal{Z}_2 = 1 + e^{-\beta E_{t2}} + e^{-\beta E_{t3}} + e^{-\beta E_{t1}} + e^{-\beta E_-} + e^{-\beta E_+}. \tag{D.44}$$

In the limit of $h \to 0$ the ground state is $|v_- >$ which is a combination of $|S >$, $|D_d >$ and $|D_1 >$, respectively the singlet, the doubled occupied impurity and the doubled occupied state in the bath.

D.3 Limits of susceptibility in the grand canonical ensemble

D.3.1 $T \to 0$

When $T \to 0$ the relevant state participating to the susceptibility is the state with the lowest energy when $N = 2$. the magnetization to consider is thus

$$m_2 \sim \frac{-e^{-\beta E_-}\frac{2h}{N_-^2}(v_{-t}v_-^{(s)})}{Z_{2p}} \tag{D.45}$$

deriving to find the susceptibility

$$\frac{\partial m_2}{\partial h} = -\frac{e^{-\beta E_-}\frac{2}{N_-^2}(v_{-t}v_-^{(s)})}{Z_{2p}} + \frac{e^{-\beta E_-}\frac{6h}{N_-^3}\frac{\partial N_-}{\partial h}(v_{-t}v_-^{(s)})}{Z_{2p}} - \frac{e^{-\beta E_-}\frac{2h}{N_-^2}(v_{-t}v_-^{(s)})}{Z_{2p}^2}\frac{\partial Z_{2p}}{\partial h} \tag{D.46}$$

When the temperature goes to 0

$$Z_{2p} \sim e^{-\beta E_-}\left(e^{-\beta(E_+ - E_-)} + e^{-\beta(E_{t2} - E_-)} + e^{-\beta(E_{t3} - E_-)} + e^{\beta E_-} + 1\right) \tag{D.47}$$

thus, Z_{2p} has a term going to ∞ which simplifies with the one in the numerator of Eq. D.46, and a sum of finite terms. The second and third terms of Eq. D.46 go to 0 when $h \to 0$. The susceptibility at low temperatures is then

$$\frac{\partial m_2}{\partial h}|_{h=0,\beta\to\infty} = -2(v_{-t}v_-^{(s)}) = \tag{D.48}$$

$$= \frac{4V^2}{\sqrt{\frac{U^2}{16} + 4V^2}\left(\sqrt{\frac{U^2}{16} + 4V^2} - \frac{U}{4}\right)^2} = \tag{D.49}$$

$$= \frac{1}{2V\sqrt{u^2+1}\left(\sqrt{u^2+1} - u\right)^2} \tag{D.50}$$

where the variable u is defined $u = \frac{U}{8V}$.

D.3.2 $T \to \infty$

In this limit, we have to take the derivative of the Eq. D.36, because at high temperatures the temperature dependence of the susceptibility coincides with the one for 1/3-particles in the canonical ensemble. First of all, we take the limit for $T \to \infty$ of the magnetization, so we expand around $\beta = 0$ up to the second order, given that $\hat{n}_3^{(\prime)} = \frac{n_3^{(\prime)}}{|\vec{n}^{(\prime)}|}$

$$m_{13} \sim \frac{1}{4}\left[\beta(n_3 - n_0 - n_3' + n_0') + \beta^2\left(\frac{|\vec{n}|^2}{2} - \frac{|\vec{n'}|^2}{2} - n_0 n_3 + n_0' n_3'\right) - \frac{\beta^2}{2}(n_3 - n_0 - n_3' + n_0')(n_0 + n_0')\right] \tag{D.51}$$

by deriving respect to h and posing $h = 0$ and $\epsilon_d = -\frac{U}{2}$ and $\epsilon_F = 0$

$$\frac{\partial m_{13}}{\partial h}|_{h=0} = \frac{\beta}{2} + \frac{\beta^2 U}{8} \tag{D.52}$$

D.3.3 Crossing temperature

To find the temperature T_x where these two cross one has to equal the two behaviours at $T \to \infty$ and $T = 0$

$$\frac{1}{2T_x} = \frac{4V^2}{\sqrt{\frac{U^2}{16} + 4V^2}\left(\sqrt{\frac{U^2}{16} + 4V^2} - \frac{U}{4}\right)^2} \tag{D.53}$$

$$T_x = \frac{\sqrt{\frac{U^2}{16} + 4V^2}\left(\sqrt{\frac{U^2}{16} + 4V^2} - \frac{U}{4}\right)^2}{8V^2} = V\sqrt{1+u}(\sqrt{1+u} - u)^2 \tag{D.54}$$

where $u = \frac{U}{8V}$.

T_x give an estimation of where the high and low temperatures limit cross although this is not a criterion to determine the peak's position because it is more determined by the change of the relative weight between the states and this calculation is more complex.

APPENDIX E

IPT+CPA ALGORITHM

The algorithm used in this work is similar to the one described in [76]. The main idea is to average the impurity green's functions over the disorder configurations. The average green's function is then the local Green's function used in the DMFT loop. The same idea but with the electron-phonon self-consistency has been used in [105].

First, we calculated the green's function for N-impurity problems. For each disorder configuration, the impurity model is away from half-filling and we have to follow the scheme proposed in [**?**]. We first need an auxiliary field $G_{0,\xi}$ which is useful to calculate the second-order pert. theory self-energy ($\Sigma^{(2)}_{\xi}(\omega)$). It has a replacement of the chemical potential with a guess for $\tilde{\mu}_{\xi}$ which is determined self-consistently in a lower impurity loop.

$$G_{0,\xi}(\omega) = \frac{1}{\omega + \tilde{\mu}_{\xi} - \Delta(\omega)} \tag{E.1}$$

from this, we calculate the density

$$n_{0,\xi} = -\frac{1}{\pi} Im \int G_{0,\xi}(\omega) f(\omega) d\omega \tag{E.2}$$

The second-order perturbation theory self-energy for the impurity problem is calculated with the convolution of the three auxiliary fields $G_{0,\xi}$

$$Im\Sigma^{(2)}_{\xi}(\omega) = -U^2 \pi G_{0,\xi} * G_{0,\xi} * G_{0,\xi} \tag{E.3}$$

The real part of the self-energy is the Kramers-Kronig of the imaginary one.

The interpolating self-energy $\Sigma_{\xi}(\omega)$ representing the impurity self-energy for the single configuration

$$\Sigma_{\xi,U}(\omega) = U n_{\xi} + \frac{A_{\xi}\Sigma^{(2)}_{\xi}(\omega)}{1 - B_{\xi}\Sigma^{(2)}_{\xi}(\omega)} \tag{E.4}$$

and

$$A_\xi = \frac{n_\xi(1-n_\xi)}{n_{0,\xi}(1-n_{0,\xi})}$$
$$B_\xi = \frac{(1-n_\xi)U - \xi - \mu + \tilde{\mu}_\xi}{n_{0,\xi}(1-n_{0,\xi})U^2}$$

The updated impurity Green function ($G_\xi(\omega)$) is calculated with the new self-energy ($\Sigma_\xi(\omega)$)

$$G_\xi(\omega) = \frac{1}{G^{-1}_{0,\xi}(\omega) - \Sigma_{\xi,U}(\omega) - \tilde{\mu}_\xi + \mu + \xi} = \tag{E.5}$$
$$= \frac{1}{\omega + \mu - \Delta(\omega) + \xi - \Sigma_{\xi,U}(\omega)} \tag{E.6}$$

and the density n_ξ

$$n_\xi = -\frac{1}{\pi} Im \int G_\xi(\omega) f(\omega) d\omega \tag{E.7}$$

At this point, we impose the condition for finding $\tilde{\mu}_\xi$ which is $n_\xi = n_{0,\xi}$ (Eq.E.7=Eq.E.2) [46].

Outside the lower impurity loop, we perform the average of the impurity green's functions over the disorder configurations with a Gaussian distribution ($P(\xi)$) for the disorder

$$\langle G \rangle_\xi(\omega) = \int P(\xi) G_\xi(\omega) d\xi \tag{E.8}$$

and the local quantities $G_0(\omega)$, $\Sigma(\omega)$ and $G_{loc}(\omega)$ are calculated.

$$G_0^{-1}(\omega) = \omega - \Delta(\omega) + \mu \tag{E.9}$$
$$\Sigma(\omega) = G_0^{-1}(\omega) - \langle G \rangle_\xi^{-1}(\omega) \tag{E.10}$$
$$G_{loc}(\omega) = \int \frac{\mathcal{N}(\epsilon)}{\omega + \mu - \epsilon - \Sigma(\omega)} d\epsilon \tag{E.11}$$
$$\Delta(\omega) = \frac{D^2}{4} \langle G \rangle_\xi(\omega) \tag{E.12}$$

APPENDIX F

COMPARISON OF SAMPLING THE PROBABILITY DISTRIBUTION USING INTERNAL AND FREE ENERGIES

In this appendix is shown a comparison between results obtained with two different methods of calculation of the probability distribution: an exact calculation based on the free energy (Eq. 4.29), and an approximate approach employed in this work for the IPT solver, which relies on the internal energy (Eq. 4.30). These calculations are presented for two limiting cases where the free energy can be determined analytically: the non-correlated regime (Holstein model) and the atomic limit.

Non-correlated limit

The exact solution of the Holstein model can be obtained numerically. A comparison between the exact solution with the probability distribution calculated with the free-energy 4.29 and the approximated one with the internal energy 4.30 is shown in Fig. F.1. In particular, the compared quantity is the resistivity for two different values of the electron-phonon coupling λ varying T. For small couplings the discrepacy is lower than for higher couplings, but in our range the maximum λ is 0.18.

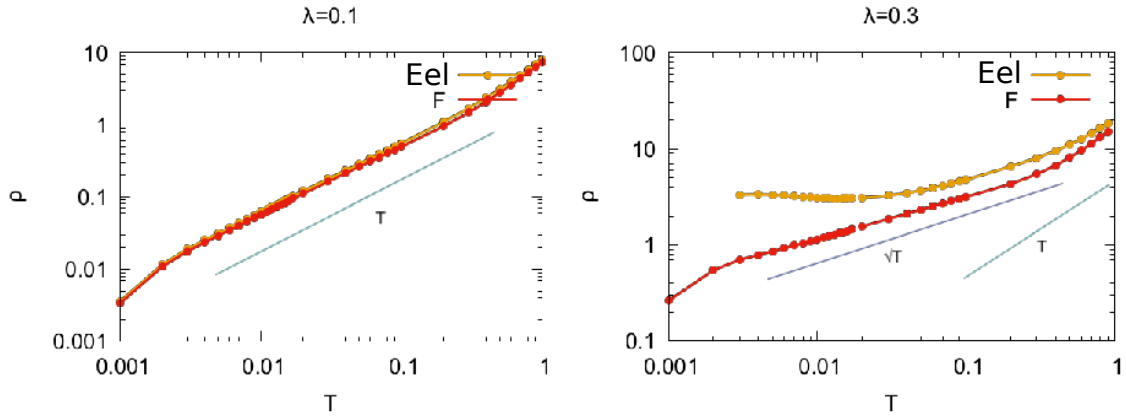


Figure F.1: Resistivity of the Holstein model calculated with the exact probability distribution and with the approximated one with the internal electronic energy. It is shown for two different values of the electron-phonon coupling λ.

Atomic limit

To show which is the difference in using the two different approaches using the free energy and the electronic energy one can study the atomic limit of the Hubbard-Holstein model where the probability can be calculated analitically in both cases. The model is

$$\hat{H} - \mu\hat{N} = \frac{1}{2}kX^2 + (gX - \mu)(n_\uparrow + n_\downarrow) + Un_\uparrow n_\downarrow \tag{F.1}$$

In order to analyze whether the approximation is reliable we have to find the crossover line for the polaronic transition in both cases. In the atomic limit, the available states are the non-occupied, the single and the double occupied ones ($\{|0>, |\uparrow>, |\downarrow>, |\uparrow\downarrow>\}$).

The probability for the phonons (in Eq. 4.29) is:

$$P(X) = \frac{e^{-\beta E_0(X)} + 2e^{-\beta E_1(X)} + e^{-\beta E_2(X)}}{\mathcal{Z}} \tag{F.2}$$

The associated energies for each state are:

$$\begin{aligned} E_0(x) &= \frac{1}{2}kx^2 \\ E_1(x) &= \frac{1}{2}kx^2 + gX - \mu \\ E_2(x) &= \frac{1}{2}kx^2 + 2gX - 2\mu + U \end{aligned} \tag{F.3}$$

and the probability distribution in Eq. F.2 becomes like three Gaussians centered in (0, $-g/k$, and $-2g/k$), with variance $\sigma^2 = 1/(\beta k)$. In order to center the three Gaussians in 0, we apply a shift

$$X = x + \frac{g}{k}$$

and

$$\begin{aligned} E_0(x) &= \frac{1}{2}kX^2 - gX \\ E_1(x) &= \frac{1}{2}kX^2 - \frac{g^2}{k} - \mu = \frac{1}{2}kX^2 - \mu' \\ E_2(x) &= \frac{1}{2}kX^2 + gX - 2\frac{g^2}{k} - 2\mu + U = \frac{1}{2}kX^2 + gX - 2\mu' + U \end{aligned} \tag{F.4}$$

by defining at half-filling $\mu' = \frac{U}{2}$, the energies are

$$\begin{aligned} E_0(X) &= \frac{1}{2}kX^2 - gX \\ E_1(X) &= \frac{1}{2}kX^2 - \frac{U}{2} \\ E_2(X) &= \frac{1}{2}kX^2 + gX \end{aligned} \tag{F.5}$$

By substituting the energies, the probability becomes

$$P(X) = \frac{e^{-\beta\frac{k}{2}X^2}(e^{\beta gX} + 2e^{\beta\frac{U}{2}} + e^{-\beta gX})}{\mathcal{Z}} \tag{F.6}$$

and

$$\mathcal{Z} = \int dX e^{-\beta\frac{k}{2}X^2}\mathcal{Z}_{el} = \int dX e^{-\beta\frac{k}{2}X^2}(e^{\beta gX} + 2e^{\beta\frac{U}{2}} + e^{-\beta gX}) = W_0 + W_1 + W_2 \tag{F.7}$$

$$W_0 = W_2 = \sqrt{\frac{2\pi}{\beta k}}e^{\frac{\beta g^2}{2k}}$$
$$W_1 = 2\sqrt{\frac{2\pi}{\beta k}}e^{\frac{\beta U}{2}}$$

The central peak corresponds to the probability of singly occupied states, while the two side peaks represent the probabilities of empty and doubly occupied states, respectively. The transition between a single-peak structure and a two-peak structure is known as the *Polaron crossover*. This crossover results from variations in the relative weights of the three peaks, which are governed by the balance between the interaction strength, U, and the electron-phonon coupling, characterized by $\lambda = \frac{g^2}{2k}$. The interplay between these factors determines the crossover: the interaction U favors electron localization, while the electron-phonon coupling λ promotes double occupancy of lattice sites.

To identify the crossover from a single-peak or three-peak state to the polaronic two-peak state, the second derivative of the probability at $X = 0$ can be evaluated:

$$\frac{d^2P(X)}{dX^2}|_{X=0} > 0 \tag{F.8}$$

When this condition is satisfied, the characteristic polaronic two-peak structure emerges.

A derivation is presented here for both the free-energy and internal energy cases. Considering that the probability can be written as $P(X) = \exp(-\beta V(X))$, the relation can equivalently be determined by calculating the second derivative of the exponent:

$$\left.\frac{d^2V(X)}{dX^2}\right|_{X=0} < 0. \tag{F.9}$$

When the probability follows the specific form associated with the free energy:

$$P(X) \propto e^{-\beta\left(\frac{1}{2}kX^2 + F(X)\right)}, \tag{F.10}$$

the free energy is given by:

$$F(X) = -\frac{1}{\beta}\ln\left(2e^{\beta\frac{U}{2}} + 2\cosh(\beta gX)\right). \tag{F.11}$$

Performing the calculation for the second derivative yields:

$$\left.\frac{d^2V(X)}{dX^2}\right|_{X=0} = k - \frac{g^2\beta}{1+e^{\beta\frac{U}{2}}}. \tag{F.12}$$

The polaronic crossover line can be determined as:

$$\frac{U}{4\epsilon_p} - \frac{\beta\frac{U}{2}}{1+e^{\beta\frac{U}{2}}} = 0, \tag{F.13}$$

where $\epsilon_p = \frac{g^2}{2k}$ is the polaronic energy.

For the case involving internal energy instead of free energy, the probability distribution is (Eq. 4.30):

$$P(X) \propto e^{-\beta\left(\frac{k}{2}X^2+U(X)\right)}, \tag{F.14}$$

where the electronic energy $E_{el}(x)$ is:

$$E_{el}(X) = -\frac{\partial}{\partial\beta}\ln\mathcal{Z}_{el}(X) = -\frac{Ue^{\beta\frac{U}{2}} + 2gX\sinh(\beta gX)}{\mathcal{Z}_{el}(X)}. \tag{F.15}$$

Using the same procedure as in the free-energy case, the zero line of the second derivative for the crossover region is given by:

$$\frac{U}{8\epsilon_p} - \frac{1+\left(1-\beta\frac{U}{2}\right)e^{\beta\frac{U}{2}}}{\left(1+e^{\beta\frac{U}{2}}\right)^2} = 0. \tag{F.16}$$

When the second derivative of the probability is greater than 0, the probability distribution for phonon displacements exhibits two peaks. Conversely, when the second derivative is lower than 0, the distribution may display one or three peaks, with their relative weights determined by the factors in Eq. F.7.

In Fig. F.2, the transition lines calculated using the free energy (green lines) and the electronic energy (yellow lines) are presented. While the overall qualitative behaviour remains consistent, the crossover determined from the internal energy shows a discrepancy by a factor of 2.

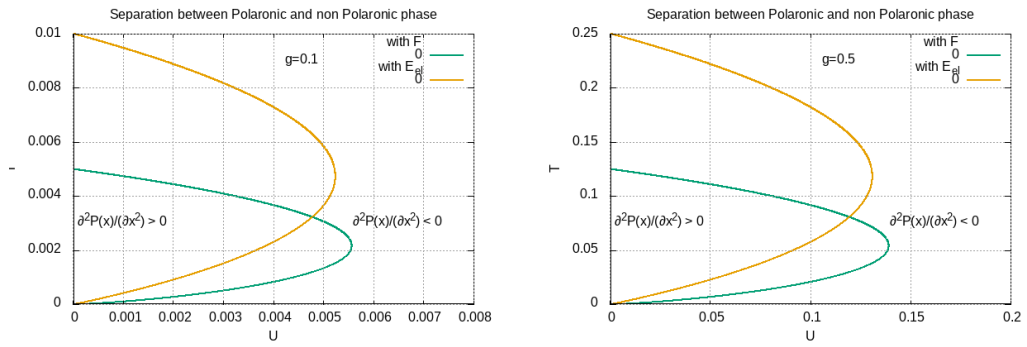


Figure F.2: Phase diagrams (T, U) of the polaronic/non-polaronic phase at two different values of the g constant (0.1, 0.5)

This analysis confirms that our approximation is valid for examining the qualitative behaviour of a correlated system coupled with classical phonons.

APPENDIX G

SELF-ENERGY SUM-RULES WITHIN IPT

To validate the results obtained with IPT, we verified that the self-energy satisfies the corresponding sum rules. Specifically, at half-filling, the self-energy must adhere to the sum rule given by:

$$-\frac{1}{\pi}\int_{-\infty}^{\infty} Im\Sigma(\omega)d\omega = \frac{U^2}{4} \tag{G.1}$$

To verify this sumrule, the imaginary frequency self-energy can be derived and compared to the literature:

$$\Sigma(i\omega_n) = \frac{1}{\pi}\int_{-\infty}^{\infty} \frac{Im\Sigma(\omega)}{i\omega_n - \omega}d\omega \tag{G.2}$$

which in the limit of high frequencies $i\omega_n \to \infty$

$$\Sigma(i\omega_n \to \infty) = \frac{1}{i\omega_n\pi}\int_{-\infty}^{\infty} Im\Sigma(\omega)d\omega = -\frac{U^2}{4i\omega_n} \tag{G.3}$$

The large frequency expansion of the self-energy in imaginary frequencies has been compared to the one obtained with an expansion for small times of the local Green's function and the bare one, and through the Dyson equation and the equation of motion [106, 107].

To verify that our IPT code follows the sum-rule in Eq. G.1 the $i\omega_n Im\Sigma(i\omega_n)$ is analyzed in Fig. G.1 and the high frequency limit corresponds precisely to the integral of the imaginary part of the self-energy, $-U^2/4$, at the corresponding U.

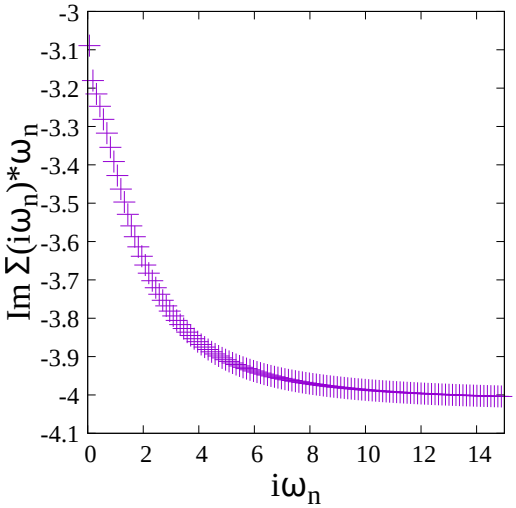


Figure G.1: Imaginary part of the self-energy in imaginary frequencies multiplied by the Matsubara frequency for $U = 4.0$. In Imaginary frequencies, when the frequency goes to infinite the function tends to the limit $-U^2/4$.